

# On Intrinsic Uncertainties in Earth System Modelling

D I S S E R T A T I O N

zur Erlangung des akademischen Grades  
Doktor der Naturwissenschaften (Dr. rer. nat.)  
in der Wissenschaftsdisziplin Theoretische Physik

eingereicht an der  
Mathematisch-Naturwissenschaftlichen Fakultät  
der Universität Potsdam

von  
**Brigitte Knopf**  
geboren am 28.08.1973 in Bonn

Potsdam, im Juni 2006



Ignorance is a situation in which man may be enclosed  
as narrowly as in a prison

*Simone de Beauvoir (1908-86)*  
*“Pour une morale de l’ambiguïté”, 1947*

Ignorance gives one a large range of probabilities

*George Eliot (1819 - 1880)*



## Abstract

Uncertainties are pervasive in the Earth System modelling. This is not just due to a lack of knowledge about physical processes but has its seeds in intrinsic, i.e. inevitable and irreducible, uncertainties concerning the process of modelling as well. Therefore, it is indispensable to quantify uncertainty in order to determine, which are robust results under this inherent uncertainty. The central goal of this thesis is to explore how uncertainties map on the properties of interest such as phase space topology and qualitative dynamics of the system. We will address several types of uncertainty and apply methods of dynamical systems theory on a trendsetting field of climate research, i.e. the Indian monsoon.

For the systematic analysis concerning the different facets of uncertainty, a box model of the Indian monsoon is investigated, which shows a saddle node bifurcation against those parameters that influence the heat budget of the system and that goes along with a regime shift from a wet to a dry summer monsoon. As some of these parameters are crucially influenced by anthropogenic perturbations, the question is whether the occurrence of this bifurcation is robust against uncertainties in parameters and in the number of considered processes and secondly, whether the bifurcation can be reached under climate change. Results indicate, for example, the robustness of the bifurcation point against all considered parameter uncertainties. The possibility of reaching the critical point under climate change seems rather improbable.

A novel method is applied for the analysis of the occurrence and the position of the bifurcation point in the monsoon model against parameter uncertainties. This method combines two standard approaches: a bifurcation analysis with multi-parameter ensemble simulations. As a model-independent and therefore universal procedure, this method allows investigating the uncertainty referring to a bifurcation in a high dimensional parameter space in many other models.

With the monsoon model the uncertainty about the external influence of El Niño / Southern Oscillation (ENSO) is determined. There is evidence that ENSO influences the variability of the Indian monsoon, but the underlying physical mechanism is discussed controversially. As a contribution to the debate three different hypotheses are tested of how ENSO and the Indian summer monsoon are linked. In this thesis the coupling through the trade winds is identified as key in linking these two key climate constituents. On the basis of this physical mechanism the observed monsoon rainfall data can be reproduced to a great extent. Moreover, this mechanism can be identified in two general circulation models (GCMs) for the present day situation and for future projections under climate change.

Furthermore, uncertainties in the process of coupling models are investigated, where the focus is on a comparison of forced dynamics as opposed to fully coupled dynamics. The former describes a particular type of coupling, where the dynamics from one sub-module is substituted by data. Intrinsic uncertainties and constraints are identified that prevent the consistency of a forced model with its fully coupled counterpart. Qualitative discrepancies between the two modelling approaches are highlighted, which lead to an overestimation of predictability and produce artificial predictability in the forced system. The results suggest that bistability and intermittent predictability, when found in a forced model set-up, should always be cross-validated with alternative coupling designs before being taken for granted.

All in this, this thesis contributes to the fundamental issue of dealing with uncertainties the climate modelling community is confronted with. Although some uncertainties allow for including them in the interpretation of the model results, intrinsic uncertainties could be identified, which are inevitable within a certain modelling paradigm and are provoked by the specific modelling approach.



## Zusammenfassung

Die vorliegende Arbeit untersucht, auf welche Weise Unsicherheiten, wie sie in der integrierten Klima-(folgen)forschung allgegenwärtig sind, die Stabilität und die Struktur dynamischer Systeme beeinflussen. Im Rahmen der Erdsystemmodellierung wird der Unsicherheitsanalyse zunehmend eine zentrale Bedeutung beigemessen. Einerseits können mit ihrer Hilfe disziplinäre Qualitätsstandards verbessert werden, andererseits ergibt sich die Chance, im Zuge von “Integrated Assessment” robuste entscheidungsrelevante Aussagen abzuleiten.

Zur systematischen Untersuchung verschiedener Arten von Unsicherheit wird ein konzeptionelles Modell des Indischen Monsuns eingesetzt, das einen Übergang von einem feuchten in ein trockenes Regime aufgrund einer Sattel-Knoten-Bifurkation in Abhängigkeit derjenigen Parameter zeigt, die die Wärmebilanz des Systems beeinflussen. Da einige dieser Parameter anthropogenen Einflüssen und Veränderungen unterworfen sind, werden zwei zentrale Punkte untersucht: zum einen, ob der Bifurkationspunkt robust gegenüber Unsicherheiten in Parametern und in Bezug auf die Anzahl und die Art der im Modell implementierten Prozesse ist und zum anderen, ob durch anthropogenen Einfluss der Bifurkationspunkt erreicht werden kann. Es zeigt sich unter anderem, dass das Auftreten der Bifurkation überaus robust, die Lage des Bifurkationspunktes im Phasenraum ist hingegen sehr sensitiv gegenüber Parameterunsicherheiten ist.

Für diese Untersuchung wird eine neuartige Methode zur Untersuchung des Auftretens und der Lage einer Bifurkation gegenüber Unsicherheiten im hochdimensionalen Parameterraum entwickelt, die auf der Kombination einer Bifurkationsanalyse mit einer multi parametrischen Ensemble Simulation basiert.

Mit dem Monsunmodell wird des weiteren die Unsicherheit bezüglich des externen Einflusses von El Niño / Southern Oscillation (ENSO) untersucht. Es ist bekannt, dass durch ENSO die Variabilität des Indischen Monsun beeinflusst wird, wohingegen der zu Grunde liegende Mechanismus kontrovers diskutiert wird. In dieser Arbeit werden drei verschiedene Hypothesen zur Kopplung zwischen diesen beiden Phänomenen untersucht. Es kann gezeigt werden, dass die Passat Winde einen Schlüsselmechanismus für den Einfluß von ENSO auf den Indischen Monsun darstellen. Mit Hilfe dieses Mechanismus können die beobachteten Niederschlagsdaten des Monsuns zu einem großen Anteil reproduziert werden. Zudem kann dieser Mechanismus auch in zwei globalen Zirkulationsmodellen (GCMs) für den heutigen Zustand und für ein Emissionsszenario unter Klimawandel identifiziert werden.

Im weiteren Teil der Arbeit werden intrinsische Unsicherheiten identifiziert, die den Unterschied zwischen der Kopplung von Teilmodulen und dem Vorschreiben von einzelnen dieser Module durch Daten betreffen. Untersucht werden dazu ein getriebenes GCM-Ensemble und ein konzeptionelles Ozean-Atmosphären-Modell, das eine strukturierte Analyse anhand von Methoden der Theorie dynamischer Systeme ermöglicht. In den meisten Fällen kann die getriebene Version, in der ein Teil der Dynamik als externer Antrieb vorschrieben wird, das voll gekoppelte Pendant nachbilden. Es wird gezeigt, dass es jedoch auch Regionen im Phasen- und Parameterraum gibt, in dem sich die zwei Modellierungsansätze signifikant unterscheiden und unter anderem zu einer Überschätzung der Vorhersagbarkeit und zu künstlichen Zuständen im getriebenen System führen. Die Ergebnisse legen den Schluss nahe, dass immer auch alternative Kopplungsmechanismen getestet werden müssen bevor das getriebene System als adäquate Beschreibung des gekoppelten Gesamtsystems betrachtet werden kann.

Anhand der verschiedenen Anwendungen der Unsicherheitsanalyse macht die Arbeit deutlich, dass zum einen Unsicherheiten intrinsisch durch bestimmte Arten der Modellierung entstehen und somit unvermeidbar innerhalb eines Modellierungsansatzes sind, dass es zum anderen aber auch geeignete Methoden gibt, Unsicherheiten in die Modellierung und in die Bewertung von Modellergebnissen einzubeziehen.





# Contents

<b>1</b>	<b>Introduction</b>	<b>1</b>
1.1	Classification of uncertainty . . . . .	2
1.1.1	Uncertainty in parameters . . . . .	3
1.1.2	Structural uncertainty in parameterisations . . . . .	3
1.1.3	Structural uncertainty of external forcings . . . . .	4
1.1.4	Structural uncertainty of coupling models . . . . .	4
1.2	Motivation and outline of the thesis . . . . .	5
<b>2</b>	<b>Uncertainty analysis of a model of the Indian Monsoon</b>	<b>9</b>
2.1	Motivation and Introduction . . . . .	9
2.2	Model description and equations . . . . .	12
2.3	Stability of the Indian summer monsoon . . . . .	17
2.3.1	Bifurcation analysis of the model M1 . . . . .	17
2.3.2	Normal form of the bifurcation . . . . .	20
2.3.3	Relevance of the bifurcation for paleo times . . . . .	22
2.4	Uncertainty analysis of the model hierarchy . . . . .	26
2.4.1	Model M2: Calculation of clouds and planetary albedo . . . . .	27
2.4.2	Model M3: Consideration of Hadley and trade wind circulation . . . . .	28
2.4.3	Model M4: Modelling the vegetation and the Tibetan Plateau . . . . .	29
2.5	Multi-run parameter uncertainty analysis . . . . .	32
2.5.1	Method . . . . .	33
2.5.2	Model and parameters . . . . .	33
2.5.3	Monte-Carlo analysis . . . . .	34
2.5.4	Global sensitivity analysis . . . . .	35
2.5.5	Deterministic parameter screening . . . . .	39
2.5.6	Deterministic parameter screening of anthropogenically influenced parameters . . . . .	42
2.6	Conclusions . . . . .	44
<b>3</b>	<b>On the physical link between the Indian monsoon and ENSO: past and future</b>	<b>49</b>
3.1	Introduction . . . . .	49
3.2	The physical link between the Indian monsoon and ENSO . . . . .	52
3.2.1	Coupling through the SSTs in the Indian Ocean . . . . .	53

3.2.2	Coupling through the snow depth over Tibet . . . . .	55
3.2.3	Coupling through the zonal trade winds . . . . .	56
3.2.4	The influence of ENSO on the ISMR under climate change . . . . .	58
3.3	Conclusions . . . . .	61
<b>4</b>	<b>Coupled versus forced Models in view of predictability</b>	<b>63</b>
4.1	Motivation and Introduction . . . . .	63
4.2	Predictability in forced versus coupled GCMs . . . . .	66
4.2.1	Analysis of variance (ANOVA) . . . . .	66
4.2.2	Potential predictability and definition of locking . . . . .	68
4.2.3	GCM experiments: model setup . . . . .	69
4.2.4	GCM results: mean locking time . . . . .	69
4.2.5	GCM results: analysis of variance . . . . .	73
4.3	Predictability in a conceptual model . . . . .	78
4.3.1	Model setup . . . . .	78
4.3.2	Mathematical framework . . . . .	80
4.4	Analysis of forced versus coupled setup . . . . .	82
4.4.1	System without seasonal cycle . . . . .	82
4.4.2	The role of (un)stable periodic orbits . . . . .	86
4.4.3	System with seasonal cycle . . . . .	88
4.4.4	Influence of the type of coupling . . . . .	89
4.4.5	Influence of noise and model uncertainties . . . . .	90
4.5	On-off synchronization . . . . .	92
4.6	Conclusions . . . . .	93
4.7	Synergy . . . . .	95
<b>5</b>	<b>Summary and Conclusions</b>	<b>97</b>
5.1	Uncertainty in parameters and parameterisations . . . . .	98
5.2	Uncertainty of external forcing . . . . .	98
5.3	Multi-parameter uncertainty analysis of a bifurcation point . . . . .	99
5.4	Intrinsic uncertainty of model coupling . . . . .	99
5.5	Outlook and final remarks . . . . .	100
<b>A</b>	<b>Variables and parameters of the monsoon model</b>	<b>103</b>
A.1	Variables . . . . .	103
A.2	Parameters . . . . .	104
<b>B</b>	<b>Constants for the normal form</b>	<b>106</b>
<b>C</b>	<b>Analysis of variance (ANOVA)</b>	<b>107</b>
C.1	Notation . . . . .	107
C.2	Statistical tests . . . . .	107
	<b>Bibliography</b>	<b>109</b>

# Chapter 1

## Introduction

The multiplicity of models is imposed by the contradictory demands of a complex, heterogeneous nature and a mind that can only cope with few variables at a time; by the contradictory desiderata of generality, realism, and precision; by the need to understand and also to control; even by the opposing esthetics standards which emphasize the stark simplicity and power of a general theorem as against the richness and the diversity of living nature. These conflicts are irreconcilable.

*Richard Levins, 1966*

Various types of uncertainty plague climate change simulation, which is, in turn, a crucial element of Earth System modelling. This fact was recognized for example in the Third Assessment Report (TAR) of the Intergovernmental Panel on Climate Change (IPCC, Houghton et al. (2001)), where the authors indicate that for the period between 1990 and 2100 an increase of the global mean temperature around 1.4–5.8°C is to be expected (Houghton et al. 2001). The width of this span as well as the fact that the authors did not give a number concerning the most probable value or a probability distribution shows clearly the large uncertainty. This uncertainty does not only arise due to the different scenarios of future development concerning greenhouse gas emissions for example, but follows to large degree from the wide range of results from different models as well.

The chain of these uncertainties of imponderables in the analysis of the *Earth System* (Schellnhuber and Wenzel 1998), which includes the climate system as well as the anthroposphere, reaches from uncertainties about the existence of critical thresholds, to ignorance of the exact state of today's climate, and ultimately to a lack of knowledge concerning climate-relevant processes, some of which are visible as uncertainties in climate models. Many attempts have been made to reduce these uncertainties by gaining a conceptual understanding of processes, e.g. of El Niño / Southern Oscillation (ENSO)

(Jin 1997, e.g.) or of the Atlantic overturning (Stommel 1961; Rahmstorf 1996, e.g.), by developing methods to identify critical thresholds in the climate system (Alley et al. 2003; Rial et al. 2004, e.g.), or by implementing an increasing number of processes in a model, resulting in high resolution general circulation models (GCMs), e.g. ECHAM5/MPI-OM (Jungclaus et al. 2006) or HadCM3 (Gordon et al. 2000) and many more. Nevertheless, the much larger part of uncertainties is inevitable in the process of modelling as well as in our understanding of the Earth System.

In this thesis we will structure this conglomeration of uncertainties climate research is confronted with. We will address several types of uncertainty and apply methods of dynamical systems theory on a trendsetting field of climate research, i.e. the Indian monsoon.

We will refer to *intrinsic* uncertainty, as the type of uncertainty that is in principle irreducible and unavoidable within a modelling paradigm and that cannot be reduced by expanding our knowledge. Acknowledging the point that some uncertainty is intrinsic, it becomes clear that we have to find suitable ways of *dealing* with these uncertainties (Morgan and Henrion 1990, e.g.). This refers to the fact that as it is impossible to gain a perfect understanding of the climate system and its interrelations it is rather important to develop robust strategies to cope with our ignorance, in particular in connection with the *integrated assessment of climate change* (Rotmans and Dowlatabadi 1998; Schellnhuber and Yohe 1997, e.g.) to support decision making processes.

## 1.1 Classification of uncertainty

Numerous attempts have been made to classify the uncertainties of the coupled human-climate system, which refer partially to more general theories and concepts. In the context of control theory for instance Paté-Cornell (1996) distinguishes between *aleatory* and *epistemic* uncertainties. Aleatory uncertainty describes the random uncertainty that cannot be decreased as it is inherent and cannot be known for principal considerations. Examples are the randomness of the outcome of a dice or the internal climate variability that is irreducible as it includes stochastic elements. Epistemic uncertainties, however, represent the state of the art of our knowledge and can in principle be reduced when more information is available about the causal relationships. This distinction is made in the context of the integrated assessment of climate change, that includes the decision making process, for instance in the work of Rotmans and van Asselt (2001), which account, on the one hand for the internal variability of the system, and on the other hand for a substantial lack of knowledge. With respect to another typology, Tóth et al. (2003) distinguish between scientific uncertainties related to ignorance about processes in the climate system, uncertainties concerning the predictability of future developments and thirdly the changing perceptions of societal values and their implications for political decisions.

In this thesis the uncertainties will be categorised along their variations in the mathematical structure of a model with increasing complexity: starting from the interior view concerning the actual model under consideration, the uncertainty reaches from (internal) variations in model parameters over functional relationships and finally to (external) influ-

ences due to other factors or sub-models. All types of uncertainty classified in the following sections 1.1.1–1.1.4 will be illustrated with applications on the basis of a model of the Indian monsoon in the subsequent chapters. The ignorance about future developments (e.g. about future projections of anthropogenic greenhouse gas emissions) will be classified as a control problem and not as a problem of uncertainty and will therefore not be an integral part of this thesis.

### 1.1.1 Uncertainty in parameters

We will refer to parameter uncertainties as uncertainties that appear internally within the numerical model and are related to pure numbers. As a mnemonic we can write the model dynamics as

$$\dot{x} = F(x, p), \quad (1.1)$$

where  $x$  symbolises the state,  $F$  the model and  $p$  the parameters that are subject to uncertainty. So far, in the integrated climate research uncertainty is usually accounted for by model parameter uncertainties. Tol (1999), e.g., examined probability distributions of uncertain parameters by means of a Monte Carlo analysis in a policy optimisation model, similar to Nordhaus (1994) and Plambeck et al. (1997). In the model uncertainty analysis of GCMs, the investigation of these parameter uncertainties plays a major role as well. As this is a very time consuming and computationally expensive procedure for large models, usually only a few parameters are varied. A detailed parameter study with 11 parameters has been performed by Schneider von Deimling et al. (2006) with the CLIMBER-2 model of intermediate complexity (Petoukhov et al. 2000) to reduce the range for *climate sensitivity*<sup>1</sup> by combining ensemble simulations with observational data. Similar studies were presented by Knutti et al. (2002) and Forest et al. (2002) and in an inter-model comparison study by Petoukhov et al. (2005). A fairly new approach in terms of GCM simulations is the idea of *climateprediction.net* (CPDN 2006), where several ten thousands of private PC users run versions of the Hadley Centre models HadCM3 (Gordon et al. 2000) and HadSM3 (Williams et al. 2001) with various parameter settings. Stainforth et al. (2005) investigated the results from such GCM runs with six simultaneously varied parameters.

### 1.1.2 Structural uncertainty in parameterisations

A generalisation of the above formulation can be pictured by the following formulation, where additionally to the parametric uncertainty the uncertainty of functional relationships  $f$  is investigated:

$$\dot{x} = F_f(x, p_f). \quad (1.2)$$

Here  $f$  describes different kinds of parameterisations, which represent the involved processes within the model  $F$ . As a parameterisation we will understand a parameterised family of functional relationships with parameters  $p_f$  for characterising one particular

---

<sup>1</sup>Climate sensitivity is defined as the change in equilibrium global mean temperature following a doubling of atmospheric CO<sub>2</sub> content from 280 to 560 ppm.

process.

Uncertainties in the functional relationships  $f$  are, in contrast to parameter uncertainties, only rarely addressed in a systematic way. In most studies, only “new” parameterisations are compared with the replaced “older” ones. Examples of a systematic investigation, however, are the studies by Visser et al. (2000) where different gas cycle modules and radiative forcing schemes are successively combined with each other resulting in a large number of models within the same framework but with varying sub-modules or by Knutti et al. (2002) where a number of different ocean modules are considered. When the uncertainty in  $f$  is too large this results in uncertainty about the model  $F$  itself, an approach that has e.g. been the focus of a stability analysis of the thermohaline circulation by Dijkstra and Weijer (2003).

### 1.1.3 Structural uncertainty of external forcings

A model can also be subject to uncertainties in external (time dependent) forcings  $g(t)$  that affect the boundary of the model. This uncertainty is related to the interface between the actual model and the part of the Earth System that is not included in the model  $F$  but externally prescribed. Examples of such forcings are the anthropogenic and the orbital forcing or, when the model  $F$  just represents the atmospheric component, the sea surface temperatures that influence the atmospheric dynamics. Here the uncertainty is related to the lack of knowledge about the forcing itself and additionally to the structural uncertainty by which functional relationship  $h$  this forcing is linked to the model<sup>2</sup>:

$$\dot{x} = F_h(x, g_h(t)). \quad (1.3)$$

One prominent example of this uncertainty is the question, whether the observed trend in global mean temperature rise can be attributed to anthropogenic climate change or whether it is purely related to “natural” forcings, such as solar or volcanic forcing. In this case it could impressively be shown that only with the inclusion of the anthropogenic forcing the increase of the global mean temperature over the last 150 years could be reproduced (Stott et al. 2000, e.g.).

The interplay between ENSO and the thermohaline circulation (THC) refers e.g. to uncertainty in  $h$ , as the direction of the mutual influence of both phenomena is uncertain: Latif et al. (2000) show that a permanent El Niño situation could prevent the THC from weakening in response to greenhouse warming, whereas Timmermann et al. (2005) present results in which a breakdown of the THC could modify ENSO variability.

### 1.1.4 Structural uncertainty of coupling models

The climate system consists of many subsystems, e.g. ocean, atmosphere, vegetation and sea-ice, that interact with each other. Therefore the linkage between different disciplines is necessary for an integrated view on the climate system. Moreover, as many processes

---

<sup>2</sup>Here and in the following part of the classification we will only highlight the very detail of the model equation that is focused on. The general form would read:  $\dot{x} = F_{f,h}(x, p_f, g_h(t))$ .

occur solely through the interplay between different components of the climate system (Houghton et al. 2001). In the context of modelling this is accounted for by coupling of different models, which are afflicted with uncertainty in each case. Moreover, there are several different ways to couple the same system, but some approaches might be more suitable or, on the other hand, increase the errors more than the others. For this reason special attention is drawn on the particular uncertainties and their consequences in terms of predictability, which result from the coupling itself. This is an extension of the formulation in Eq. 1.3 where the function  $g$  is replaced by an entire model<sup>3</sup>  $G$ :

$$\begin{aligned}\dot{x} &= F(x, y) \\ \dot{y} &= G(x, y).\end{aligned}\tag{1.4}$$

For a long time, the investigation of coupled systems has aroused interest in science. Haken (1981) developed a theory of self organization (*synergetics*), which describes the cooperation of individual subsystems. The theory, which was developed particularly for physical, biological and chemical systems, was transferred gradually to economic and sociological phenomena as well. *Complexity theory* (Bak 1999, e.g.) is another approach that studies the coupling of dynamical systems. A central idea of complexity theory is that behaviour emerges from the interaction of many components (Waldrop 1992). To bridge the gap from simple to more sophisticated systems, *identical* coupled systems (Fujisaka and Yamada 1983, e.g.), coupled chaotic systems (Pecora and Carroll 1990; Pikovsky and Grassberger 1991; Pecora et al. 1997, e.g.) or coupled maps (Pikovsky and Shekhov 1991; Kaneko 1992, e.g.) are examined. In these systems *synchronization* (Pikovsky et al. 2001) – characterising the coordination of occurrences in respect of time –, which is also found in chaotic systems, and the possibility of controlling chaotic systems (Kurths et al. 2003) play a major role. It was shown that the degree of the synchronization crucially depends on the coupling strength between the systems (Zheng et al. 1998; Blakely et al. 2000). Phenomena such as synchronization are found not only in low dimensional systems, but also in spatially resolved systems. An example from the climate system is a coupled large-scale atmospheric circulation pattern where synchronization both in the model and in the data can be observed (Duane 1997).

All of these analyses suggest that the effect of coupling in climate models is crucial to the system. Above all, in many studies the coupling of two sub-modules is replaced by forcing one of them with data from the other sub-module as described in Eq. 1.3, implicitly stating that a forced and a coupled set-up are identical in terms of the analysed features although the differences between the two approaches of coupling and forcing are often not even investigated.

## 1.2 Motivation and outline of the thesis

This thesis is motivated by the need for a systematic approach to address the different kinds of uncertainty and for evaluating and integrating these uncertainties in the modelling

---

<sup>3</sup>Here the general form is  $\dot{x} = F_{f,h}(x, p_f, g_h(t), y)$  and analogously for  $y$ .

process.

Central questions pursued in this thesis are:

- What are intrinsic (i.e. inevitable and irreducible) uncertainties in Earth System modelling?
- How do uncertainties map on properties of interest (such as phase space topology and qualitative dynamics of the system)?
- What are suitable (technical) methods of dealing with uncertainties?

To investigate the influence of uncertainties on phase space topology and therefore on the equilibria of systems, the method of path-following a stable state (“bifurcation analysis”) and the detection of bifurcation points along this path is applied as the central technique. The bifurcation analysis provides the possibility to explore the stability of a system in dependence on its parameters. Furthermore, as the transient dynamics are not included in such an analysis, the examination of the system dynamics is investigated separately. The attention is turned on the interaction between sub-systems, as we have pointed out in section 1.1.4 that the effect of coupling represents a fundamental issue in Earth System modelling.

The structure of the thesis reflects the increasing complexity of uncertainties we are confronted with. We will highlight the whole chain of uncertainties in the process of modelling as classified in Eqs. (1.1)–(1.4) and reveal suitable ways of dealing with them considering a key example from the climate system, i.e. the Indian monsoon, which is an annual recurring large-scale climate phenomenon that brings vital rain to India. In chapter 2 we concentrate on the uncertainty study of a box model of the Indian monsoon that shows an abrupt shift from a wet to a dry monsoon regime, as we have demonstrated in Zickfeld et al. (2005). As this regime transition could be triggered by anthropogenic disturbances, such as aerosol forcings or forest conversion, we will build on this model and analyse the uncertainties concerning the occurrence and the position of this bifurcation in relation to the present-day state of this system. The investigation will focus on the parameter uncertainties and the uncertainties in certain parameterisations, as classified in Eqs. (1.1) and (1.2).

Singular points in the Earth System, such as bifurcation points leading to regime transitions, are found in a number of reduced form models, as examples from the thermohaline circulation (Stommel 1961; Rahmstorf 1996, e.g.), the greening of the Sahara (Brovkin et al. 1998), paleoclimatic transitions in glacial oscillations (Tziperman and Gildor 2003), and last but not least the monsoon (Kumar Mittal et al. 2005; Zickfeld et al. 2005) show. We will introduce a new method of dealing with parameter uncertainties with respect to a bifurcation, which builds on the combination of a bifurcation analysis with ensemble simulations generated by multiple parameter settings and aims at sampling the whole parameter space of a model. In chapter 2 we apply this method to analyse the bifurcation in the monsoon model.

The uncertainty concerning external forcing has to be incorporated in an uncertainty analysis, as the Indian monsoon is not an isolated phenomenon but is embedded in the



interplay of several large-scale phenomena. The Indian summer monsoon is crucially influenced by ENSO, a phenomenon representing the interaction between the equatorial Pacific Ocean and the atmospheric dynamics. We aim to identify the link between these two phenomena in chapter 3 and address the uncertainties described in Eq. (1.3) that are related to the mechanism  $h$  through which these two phenomena interact. We face these uncertainties by testing different hypotheses of possible coupling mechanisms and succeed in reproducing the observed time series of the monsoon precipitation with the model of the Indian monsoon. Since not just the link for the past, but also for the future under enhanced greenhouse warming is uncertain, we investigate future projections from different GCM models to gain more insight about the functional relationship  $h$  of Eq. (1.3).

The main aspect of chapter 4 is the investigation of uncertainties that arise from the difference of coupling model components as described in Eq. (1.4) in relation to forcing one module with data as illustrated in Eq. (1.3). We compare coupled nonlinear climate models and their simplified forced counterparts with respect to predictability and phase space topology. The latter represents a particular type of coupling, where the transient behaviour of one system component is prescribed by data or some other external information source. Such a simplifying technique is often employed in Earth System models in order to save computation time, in particular when massive model inter-comparisons need to be carried out. Here we will address the interplay of initial condition uncertainty and model structure uncertainty. Our contribution to the debate is based on the investigation of two representative ocean-atmosphere models, in particular a GCM and a conceptual model, where for both models the fully coupled and a replica-like simulator embracing corresponding components are analysed.

Chapter 5 summarises the findings and gives an outlook for further strategies to proceed with uncertainty in climate research.



## Chapter 2

# Uncertainty analysis of a model of the Indian Monsoon

### 2.1 Motivation and Introduction

The Indian Monsoon is an annual recurring phenomenon that brings vital rain to India. Life in India depends strongly on the monsoon rain and its effects on India's agriculture (Parthasarathy et al. 1992; Webster et al. 1998). A weak summer monsoon, as e.g. in 2000, can be accompanied by poor harvests and food shortages and a lack of fresh water among the rural population, which constitutes two thirds of India's total population. On the other hand, a monsoon with higher precipitation than normal, as e.g. in 2005, can cause disastrous conditions with life-threatening floods, again leading to a failure of harvest and food shortage.

Climatologically, the Indian Monsoon is part of a large-scale circulation pattern, known as the Asian Monsoon. The summer monsoon investigated here occurs from June to September and develops due to thermal gradients between the warm Indian continent and the cooler temperatures in the Indian Ocean. The warmer air masses over land result in areas of low pressure whereas over the ocean the colder air masses yield higher pressures. This pressure gradient entails the supply of moisture over the Indian continent that ascends, condensates, and is released as precipitation. Several processes influence the Indian monsoon: the sea surface temperatures (SSTs) over the Indian Ocean (Clark et al. 2000; Kucharski et al. 2006, e.g.), land surface characteristics like soil moisture or the surface albedo (Meehl 1994; Claussen 1997; Robock et al. 2003, e.g.), large scale circulations like the Hadley and the Walker or trade wind circulation (Webster and Yang 1992; Krishnamurthy and Goswami 2000, e.g.), the orography, e.g. of the Tibetan Plateau (Liu and Yin 2002, e.g.), or the snow cover over Eurasia (Hahn and Shukla 1976; Dash et al. 2005, e.g.). Moreover, the Indian monsoon is strongly linked to other global scale phenomena, like El Niño / Southern Oscillation (ENSO) (Shukla and Paolino 1983; Meehl and Arblaster 1998; Kitoh et al. 1999; Latif et al. 2001, e.g.) or even the North Atlantic Oscillation (NAO) (Kripalani et al. 1997; Chang et al. 2001, e.g.).

The influence of anthropogenic activities on the Indian summer monsoon has been

investigated in a number of studies. Most of them indicate that emissions of greenhouse gases, that alter the heat budget of the system and therefore the land-sea temperature contrast, could increase the monsoon intensity and/or variability (Meehl and Washington 1993; Zwiers and Kharin 1998; May 2002). On the other hand, there is evidence of aerosol-induced reduction of precipitation as well (Patra et al. 2005, e.g.) or of no clear indication for an influence of global warming at all (Kripalani et al. 2003).

Climate research is in charge of providing a full understanding of the Monsoon system with its dependence on other climatological phenomena, e.g. ENSO. Moreover, the challenge is to put forecasts at disposal, so that the Indian population can adapt to perturbations of monsoon rainfalls below or above normal. At the first place this includes the need to gain an understanding in the effect of anthropogenic perturbations, e.g. land cover changes, climate change, or emissions of aerosols, on the monsoon precipitation.

In this chapter we will attend to the aforementioned tasks by analysing a model of the Indian Monsoon in consideration of perturbations due to climate change. For this study we use a box model of the Indian monsoon circulation that we have analysed in Zickfeld et al. (2005). The major finding is a saddle node bifurcation<sup>1</sup> in dependence on those parameters that influence the heat balance of the system, such as the planetary albedo or the atmospheric CO<sub>2</sub> concentration. The bifurcation implies a regime shift from a wet to a dry summer monsoon and would therefore have dramatic effects for the population of India. Hence, the guiding questions in this chapter are

- Which mechanism leads to the qualitative change in the Monsoon system?
- Which parameters influence this regime transition?
- How do simultaneously varied parameters influence the position and the occurrence of the bifurcation point?
- What are the main uncertainties in the model concerning the parameterisations or the choice of the considered physical processes?
- How does global change affect the Indian monsoon?

We address these questions by performing an uncertainty analysis that will cover the two types of internal model uncertainty as introduced in sections 1.1.1 and 1.1.2 that is related to uncertainty in parameters and parameterisations. The uncertainties due to the influence of external effects, e.g. of ENSO, will be the focus of chapter 3. As the occurrence of this bifurcation is dependent on the choice of parameters and of the implemented processes in the model, the required uncertainty analysis of the bifurcation will be twofold.

At the first place, we investigate the model uncertainties due to the involved processes and parameterisations as classified in Eq. (1.2), by replacing a parameter, which describes a whole mechanism, with a parameterisation, which consists of a family of functional relationships. This results in an analysis of a model hierarchy with a simplified model at

---

<sup>1</sup>A bifurcation point refers to an abrupt change of the stability properties of a dynamical system at a critical parameter value (Guckenheimer and Holmes 1996, e.g.).

the low end and a much more sophisticated model with the inclusion of e.g. large scale circulation patterns at the high end. Such an investigation of a model hierarchy has been performed by Dijkstra and Weijer (2003) for the thermohaline circulation, where models of different complexity were used to analyse the stability of the ocean circulation. A study with a number of reduced form models that show a possible breakdown of the North Atlantic overturning was performed by Titz et al. (2002). A general approach to deal with the problem of model uncertainty with respect to bifurcations was presented by Gross and Feudel (2006) that classifies the systems in an abstract way according to their structure by separating the analysis of the steady states from the information about the nonlinearities, i.e. bifurcations, in the model. Here we will concentrate on investigating a model at different levels of complexity in a systematic way with respect to the processes that are taken into account.

Secondly, we will carry out a detailed parameter uncertainty analysis of the model with respect to the regime transition. In the recent years multi parameter uncertainty analysis has more and more become a standard approach in climate modelling to reduce and to quantify model uncertainty. By a multi parameter uncertainty analysis we refer to an analysis where several parameters are varied *simultaneously* to cover the whole range of possible parameter combinations. As this is a very time consuming and computationally expensive procedure in large models, in most uncertainty analyses only a few parameters are varied at the same time. A detailed parameter study with 11 parameters has been performed by Schneider von Deimling et al. (2006) with the CLIMBER-2 model of intermediate complexity to reduce the range for climate sensitivity<sup>2</sup>. Stainforth et al. (2005) performed a similar study with a general circulation model (GCM) by investigating six parameters. In our case the challenge is to expand such an analysis by providing not only the multi parameter setting but additionally to perform a bifurcation analysis. Detailed parameter studies of bifurcations are undertaken e.g. by Kumar Mittal et al. (2005) for a paradigmatic monsoon model or by Longworth et al. (2005) for a box model of the thermohaline circulation. The Lorenz system (Lorenz 1984), describing the general atmospheric circulation in midlatitude, is investigated in numerous studies with respect to its bifurcations (Shilnikov et al. 1995; van Veen et al. 2001, e.g.). However, in most of these studies the bifurcation is followed in only two parameter directions. In this chapter we will investigate the robustness of the bifurcation against uncertainties in the multi-dimensional parameter space. For this purpose a novel approach is developed that combines a bifurcation analysis with a multi-parameter sampling technique. This investigation is related to the parameter uncertainty described in Eq. (1.1). A multi-run parameter analysis with a special focus on anthropogenically influenced parameters will test the robustness of the occurrence and position of the bifurcation.

In the following we will first present the results of the bifurcation analysis that were mainly analysed in Zickfeld et al. (2005) (section 2.2 and 2.3.1). We extend this study by deriving the normal form of this bifurcation (section 2.3.2) and by investigating the possible relevance of this bifurcation for paleo times (section 2.3.3). This analysis is followed by the

---

<sup>2</sup>Climate sensitivity is defined as the change in equilibrium global mean temperature following a doubling of atmospheric CO<sub>2</sub> content.

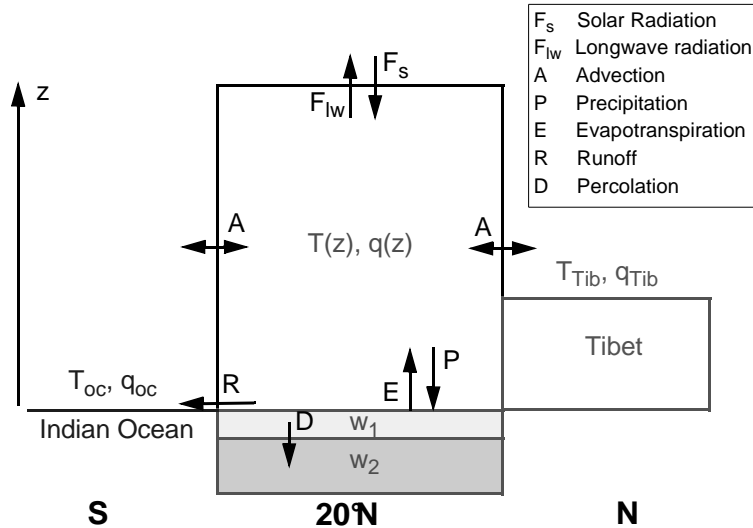


Figure 2.1: Schematic view of the box model of the Indian monsoon.  $T$  denotes temperature,  $q$  specific humidity.  $w_1$  and  $w_2$  are the soil moistures in the upper and lower soil layer. The variables inside the box ( $T(z), q(z), w_1, w_2$ ) are calculated prognostically, whereas the climatic conditions at the box boundaries ( $T_i, q_i$ , with  $i \in \{oc, Tib\}$ ) are externally prescribed. Courtesy of Kirsten Zickfeld.

uncertainty analysis related to structure (parameterisations) and parameters of the model concerning the bifurcation (section 2.4 and 2.5). A further analysis aims to investigate the performance of the model under climate change and to come up with possible changes of the monsoon system, to which the population in India could have to adapt to (section 2.5.6). Overall, we will come up with conclusions concerning the robustness of the bifurcation point and an estimate of the relevance of the bifurcation in terms of global change.

## 2.2 Model description and equations

The model used in this study is a box model of the monsoon circulation that was introduced in Zickfeld (2004) and which we analysed in detail in Zickfeld et al. (2005). In this section we will present the formulation of the model that exhibits a saddle-node bifurcation and that is subject to the uncertainty analysis in the following sections. The model comprises several parameterisations that are described in detail in Zickfeld (2004). In this thesis we will only introduce those parameterisations that are focus of the uncertainty analysis of the model. The parameters are listed in appendix A.2, whereas we keep close to the notation given in (Zickfeld 2004)<sup>3</sup>.

The model consists of one four-sided box which is centered over India and is delimited by the Indian Ocean at its eastern (E), southern (S), and western (W) boundaries and by the Tibetan Plateau (tib) at its northern boundary (cf. Fig. 2.1). In the vertical, the atmosphere is described by three layers: the surface layer, the free troposphere, and the

<sup>3</sup>The only change in reference to the cited work is that in the following the boundary conditions are prescribed as continuous functions in the seasonal cycle.

stratosphere. The underlying land compartment is represented by two soil layers. The prognostic variables in the model are the near-surface air temperature  $T_a$ , the specific humidity  $q_a$ , and the soil moisture  $w_1, w_2$  of the two soil layers. All other variables such as precipitation, evaporation, net long-wave radiation and surface wind are diagnosed from the above-mentioned four. Inside the box, the variables are described in terms of their spatial averages. The only meridional and zonal gradients are those between the box interior (i.e., the Indian sub-continent) and its boundaries, whose climatic conditions are externally prescribed with a seasonal cycle for the temperature  $T_{tib}, T_E, T_S, T_W$ , the relative humidity  $f_{tib}, f_E, f_S, f_W$ , and the cloudiness  $N_{tib}, N_E, N_S, N_W$ . The monsoon circulation is driven by the temperature gradient between the Indian peninsula and the adjacent surface air temperatures over the Indian ocean  $T_{oc} \in \{T_E, T_S, T_W\}$  and the temperature over the Tibetan Plateau, respectively.

The balance equations for the combined surface-plus-atmospheric heat, the atmospheric water vapour, and the upper/lower soil layer wetness describe the temporal evolution of the monsoon circulation:

$$\int_0^{H_a} c_p \rho \frac{\partial \theta}{\partial t} dz + h_s c_s \frac{\partial T_a}{\partial t} = F_{\downarrow}^{SL,TA} (1 - A_{sys}) - F_{\uparrow}^{LW,TA} + Ad_T + \mathcal{L} (C - E), \quad (2.1)$$

$$\int_0^{H_a} \rho \frac{\partial q}{\partial t} dz = E - C + Ad_v, \quad (2.2)$$

$$\frac{\partial w_1}{\partial t} = \frac{P - E - R}{f_1} - \frac{w_1 - w_2}{\tau}, \quad (2.3)$$

$$\frac{\partial w_2}{\partial t} = \frac{f_1}{f_2} \frac{w_1 - w_2}{\tau}, \quad (2.4)$$

where  $\theta = \theta(z)$  is the potential temperature and  $q = q(z)$  the vertical profile of the specific humidity. All prognostic and diagnostic variables in these equations are given in appendix A.1.

The left hand sides describe in Eq. (2.1) the vertically integrated heat and in Eq. (2.2) the water content from the ground up to the top of the atmosphere  $H_a$ , where  $\rho = \rho(z)$  is the height dependent air density. The first term on the right hand side of Eq. (2.1) is the incident solar radiation  $F_{\downarrow}^{SL,TA}$  at the top of the atmosphere that is a function of the insolation and the mean solar zenith angle, modified by the planetary albedo  $A_{sys}$ , which is the albedo at the top of the atmosphere. The latter is a sum of the albedos of stratus clouds ( $A_{st}$ ), cumulus clouds ( $A_{cu}$ ) and the clear sky atmosphere ( $A_{cs}$ ):

$$A_{sys} = N_{st} A_{st}^p + N_{cu} A_{cu}^p + (1 - N) A_{cs}^p, \quad (2.5)$$

where  $N$  is the total cloud amount and  $N_i$  with  $i \in \{st, cu\}$  describe the cloud covers. The total cloudiness  $N$  over India is a combination of stratus and cumulus cloud amounts with

$$N = 1 - (1 - N_{cu}) (1 - N_{st}), \quad (2.6)$$

where both types of clouds are functions of the specific humidity  $q_a$  and the vertical velocity

$w$  and  $N_{st}$  is additionally a function of the saturation specific humidity at the surface temperature  $T_a$ . In Eq. (2.5),  $A_i^p$  with  $i \in \{st, cu, cs\}$  are functions of the respective albedos  $A_i$  and the surface albedo  $A_s$ :

$$A_i^p = (A_i + (1 - A_i)^2 A_s) p_i. \quad (2.7)$$

$p_{cl} := p_{st} = p_{cu}$  and  $p_{cs}$  are the integral transmission functions. The surface albedo  $A_s$  is computed as the weighted sum of the albedos of vegetated and bare soil  $A_{sv}$  and  $A_b$ :

$$A_s = V A_{sv} + (1 - V) A_b \quad (2.8)$$

where  $V$  is the fractional vegetation cover. The dependence of the vegetation from precipitation  $P$  is calculated according to Brovkin et al. (1998) as

$$V = \begin{cases} 0 & \text{if } P < P_{cr} \\ 1 - \frac{1}{1 + a_v(P - P_{cr})^2} & \text{otherwise} \end{cases}, \quad (2.9)$$

where  $a_v$  is a parameter and  $P_{cr}$  is the critical threshold of the precipitation below which the vegetation cover cannot be sustained. The albedos of cumulus and stratus clouds and of the clear sky atmosphere again depend on several parameters, e.g. on the optical thickness of stratus and cumulus clouds  $\tau_{st}$  and  $\tau_{cu}$ :

$$A_i = b_{cl} \frac{(\tau_i)^{k_\tau}}{(\cos \xi)^{m_i}} \quad (2.10)$$

with  $i \in \{st, cu\}$  and

$$A_{cs} = \frac{b_{cs}}{(\cos \xi)^{m_{cs}}} \quad (2.11)$$

where  $b_i$  is the albedo of the semi-infinite cloud at a solar zenith angle of  $\xi = 0$  and  $k_\tau$ ,  $m_i$  are cloud droplets parameters.

The second term of Eq. (2.1) is the net outgoing longwave radiation  $F_\uparrow^{LW,TA}$ , that is – according to Budyko (1982) – a function of the atmospheric CO<sub>2</sub> concentration, the temperature  $T_a$  and the cloudiness  $N$  over India:

$$F_\uparrow^{LW,TA} = A_0 + B_0(T_a - T_0) - N(C_0 + D_0(T_a - T_0)), \quad (2.12)$$

where  $T_0$  is the reference temperature and the coefficients  $A_0, B_0, C_0, D_0$  are functions of the atmospheric CO<sub>2</sub> concentration  $pCO_2$  in relation to the reference CO<sub>2</sub> concentration  $pCO_2^0$ :

$$X_0 = X_{00} \left( 1 - \eta \ln \left( \frac{pCO_2}{pCO_2^0} \right) \right), \quad (2.13)$$

where  $X \in \{A, B, C, D\}$ .

The horizontal advection of heat  $Ad_T$  is described according to Petoukhov et al. (2000) as the vertical integral up to the height of the troposphere  $H_t$  over the sensible heat flux



due to the horizontal circulation. It is a sum of the contributions from the local monsoon circulation and the large-scale Hadley and Walker circulations. The contribution from the monsoon circulation  $u_{m,i}$  at the  $i^{\text{th}}$  boundary ( $i \in \{E, S, W, tib\}$ ),  $Ad_T^{m,i}$ , can e.g. be expressed as:

$$Ad_T^{m,i} \sim \int_0^{h_m} u_{m,i}(z) \rho \theta(T_i) dz + \int_{h_m}^{H_t} u_{m,i}(z) \rho \theta(T_a) dz. \quad (2.14)$$

Here  $\theta(T_i)$  is the potential temperature at the  $i^{\text{th}}$  boundary and  $\theta(T_a)$  that over India<sup>4</sup>. Note that Eq. (2.14) is given for summer conditions, when the temperature over land is warmer than over the adjacent ocean and the surface (upper troposphere) monsoon circulation is directed from the ocean (India) towards India (the ocean). In our model both below and above the monsoon turning height  $h_m$  the vertical profile of the monsoon winds is assumed to be constant. The surface winds associated with the local monsoon circulation,  $u_{m,i}^0$ , are computed from the temperature difference between India and the respective boundary:

$$u_{m,i}^0 \sim \frac{\sin(\alpha_0) H_t}{L} (T_a - T_i), \quad (2.15)$$

where  $L$  is the box length,  $\sin(\alpha_0)$  the cross-isobar angle. The winds above the turning height are computed from the continuity equation. The cross-isobar angle  $\sin(\alpha_0)$  describe the angle between the wind vector and an isobar and depends amongst others on the proportion between the depth of the surface layer  $z_s$  and the surface roughness  $z_0$ .

The Hadley circulation  $v_H$  is modelled in dependence on the temperature difference between the Tibetan Plateau and the equatorial Indian Ocean and gives an additional contribution to the advection of heat which is described similarly to Eq. (2.14). The third contribution to the horizontal advection of heat  $Ad_T$  stems from the zonal trade wind circulation  $u_{tr}$ . In our model the zonal winds in the upper and lower troposphere (i.e. above and below the turning height  $h_{tr}$ ) have opposite directions. For the whole atmospheric column the vertical profile of the zonal winds is approximated by a linear one with  $u_{tr}(z) = u_{tr}^{max}(z - h_{tr})/(H_t - h_{tr})$ . The seasonal course for  $u_{tr}^{max}$ , which reverses its direction from summer to winter, is derived from the climatological mean for the 200 hPa level. The contribution of the zonal winds to the advection of heat,  $Ad_T^{tr}$ , is described similarly to the advection of the monsoon circulation in Eq. (2.14) by a vertical integral of the trade winds  $u_{tr}$ , the height dependent air density  $\rho(z)$  and the difference between the potential temperatures at the eastern (western) boundary  $\theta(T_E)$  ( $\theta(T_W)$ ) and that over the Indian peninsula,  $\theta(T_a)$ . For  $u_{tr}^{max} > 0$ , the equation reads:

$$Ad_T^{tr} \sim \int_0^{h_{tr}} |u_{tr}(z)| \rho(z) (\theta(T_E) - \theta(T_a)) dz + \int_{h_{tr}}^{H_t} |u_{tr}(z)| \rho(z) (\theta(T_W) - \theta(T_a)) dz. \quad (2.16)$$

<sup>4</sup>Note that for the northern boundary Eq. (2.14) takes a slightly different form due to the elevation of the Tibetan Plateau.

For  $u_{tr}^{max} < 0$ ,  $\theta(T_W)$  is replaced by  $\theta(T_E)$  and vice versa. Substituting the potential temperatures with the according specific humidities in all three advection terms gives the formulation for the advection of moisture.

The monsoon winds at the surface  $u_{m,i}^0$  and the Hadley circulation at the surface  $v_H^0$  result in the vertical velocity  $w$  at the height of the planetary boundary layer (PBL)  $h_{PBL}$  that is the lowest layer of the troposphere:

$$w = \left( \sum_i u_{m,i}^0 + v_H^0 \right) \frac{h_{PBL}}{L}, \quad (2.17)$$

where  $h_{PBL}$  is the vertical depth of the PBL height.

The condensation rate  $C$  is set equal to the precipitation  $P$  with

$$C = P = \frac{N}{\tau_P} \int_0^{H_t} \rho q dz, \quad (2.18)$$

where  $\tau_P$  is the turnover time of water in the atmosphere that is a function of the vertical velocity  $w$ . The evapotranspiration  $E$  consists of the contributions from the transpiration from the vegetated soil and the evaporation from the bare soil. The latter is described in a bulk transfer approach (Hansen et al. 1986). Furthermore, in Eq. (2.1)  $\mathcal{L}$  refers to the latent heat of evaporation,  $c_p$  denotes the specific heat of air at constant pressure,  $h_s$  the depth of the upper soil layer, and  $c_s$  the heat capacity per unit soil volume which increases along with the water content of the soil.

Eqs. (2.3) and (2.4) describe the wetness  $w_1$  and  $w_2$  in the  $i^{\text{th}}$  layer for the soil moisture, where the runoff  $R$  is proportional to precipitation and the soil moisture in the upper layer:

$$R = K_r P w_1, \quad (2.19)$$

with the runoff constant  $K_r$ .  $f_1$  and  $f_2$  are the field capacities of the two layers and the diffusion between the two layers is described by an exponential law with the time constant  $\tau$ .

The vertical profile of the temperature  $T(z)$  is parameterised in terms of the near surface value  $T_a$  with a linear profile in  $z$  the troposphere ( $T(z) = T_a - \Gamma z$ ) and a constant profile in the stratosphere ( $T(z) = T_a - \Gamma H_t$ ). The lapse rate  $\Gamma$  is described as suggested in Petoukhov et al. (2003):

$$\Gamma = \Gamma_0 + \Gamma_1 (T_a - T_0) (1 - a_q q_a^2) - \Gamma_2 N_{cu}. \quad (2.20)$$

with parameters  $\Gamma_0, \Gamma_1, \Gamma_2, a_q$ . The humidity  $q(z)$  is modelled with an exponentially decreasing profile in  $q_a$  with

$$q(z) = q_a \exp\left(-\frac{z}{H_e}\right), \quad (2.21)$$

where  $H_e$  is the water vapour scale height.

Despite its high degree of idealisation, the model includes the most important physical processes of the monsoon system. The model satisfactorily captures relevant aspects of the

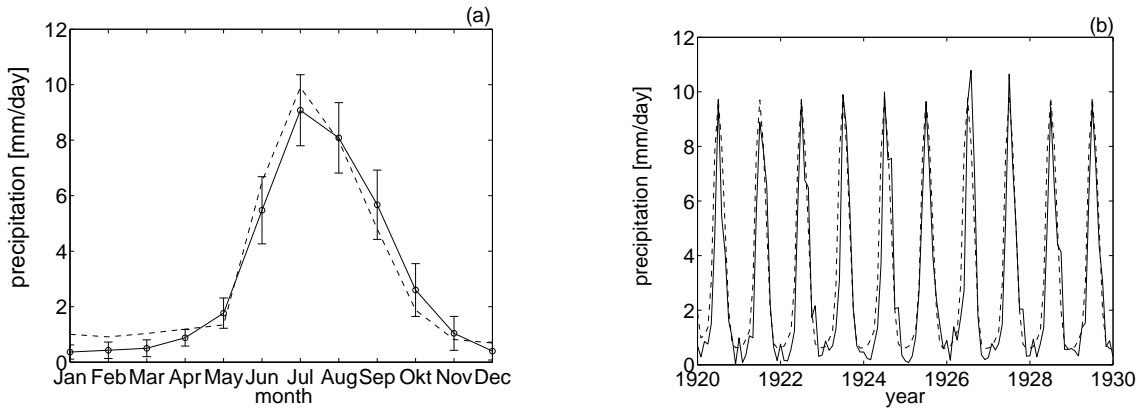


Figure 2.2: Comparison of simulated and observed values for the monthly mean rainfall over India (AIR index, Parthasarathy et al. 1995). (a) Monthly mean values of the Indian monsoon rainfall. The solid line represent the observations (with standard deviations) for the period of 1871-2003, the dotted line is the model result from the model described above where the dynamics is governed by the seasonal cycle of the boundary conditions, (b) time series of the observations in comparison to the simulated data, where the simulated data have a time step of 12 hours.

observed monsoon dynamics, such as the seasonal course of precipitation averaged over India (cf. Fig. 2.2), where we compare the simulation with observations from 1871-2003 for the All Indian Rainfall (AIR) defined in Parthasarathy et al. (1995). Deviations from the observed characteristics arise mainly in the value of winter precipitation (which is somewhat high in the model) and in the timing of the summer monsoon onset. The higher winter values could be a result of the temperature over India that is warmer in the model than in the observations. Even in winter the temperatures over land are slightly warmer than over the ocean so that the land-sea temperature gradient is not captured adequately, leading to higher winter precipitation than observed.

## 2.3 Stability of the Indian summer monsoon

### 2.3.1 Bifurcation analysis of the model M1

In Zickfeld et al. (2005) we have shown that a reduced (or basic) version of the above model undergoes a saddle node bifurcation in dependence on those parameters that influence the heat budget of the system. In this section this result will be recapitulated and extended by additional analyses of this bifurcation (section 2.3.3 and 2.3.2). The chosen method for the investigation is a bifurcation analysis, that studies possible changes in the stability properties of a system in dependence on one or more parameters. Many software packages are available for this purpose, e.g. AUTO (Doedel 1981), CONTENT (Kuznetsov et al. 1997) or CANDYS (Feudel and Jansen 1992), which all build on combining the solution of an eigenvalue problem to determine the linear stability of an equilibrium, with a method of following this solution along a path in dependence on a parameter. New methods have also been developed to handle the eigenvalue problem for large matrices (Dijkstra 2005), so

that bifurcation analysis is in principle possible for models with a large number of degrees of freedom as well. Here we will use the software AUTO that can perform a bifurcation analysis of ODEs that are subject to initial conditions, boundary conditions, and integral constraints.

The reduced or basic version of the model, denoted as M1 in the following, is deduced from Eqs. (2.1)–(2.4). As the summer rainfall is the most important monsoon characteristics, where India receives more than 80% of its annual rainfall, the boundary conditions and the parameters are fixed to summer conditions. Moreover the following assumptions are applied:

1. prescription of the planetary albedo  $A_{sys}$  (i.e., neglecting the dependence of  $A_{sys}$  on the surface albedo  $A_s$ , cumulus and stratus clouds and their albedos, cf. Eq. (2.5)),
2. prescription of cloudiness  $N$  (i.e., ignoring the dependence of the cloud cover from cumulus and stratus clouds and from the relative humidity and the vertical velocity),
3. prescription of turnover time of water in the atmosphere  $\tau_p$  (i.e., neglecting the dependence of  $\tau_p$  from the vertical velocity  $w$ ),
4. equality of effective and potential evapotranspiration (i.e., neglecting the dependence on soil type, soil moisture and vegetation characteristics),
5. neglecting the Hadley and trade wind circulation (i.e., implying that the only circulation is the local monsoon circulation),
6. prescription of fractional vegetation cover with  $V = 1$  for  $P > P_{cr}$  (i.e., ignoring the dependence of the vegetation  $V$  from precipitation  $P$  in Eq. (2.9)),
7. equal conditions at all three ocean boundaries ( $T_{oc} \equiv T_E = T_W = T_S$ ) and neglecting the boundary to the North.

As mentioned before, the most notable result of this model is the occurrence of a saddle node bifurcation in dependence on those parameters that influence the heat balance of the system. The crucial bifurcation parameters are in the first place those that are influenced by human activities, such as the planetary albedo  $A_{sys}$ , which is affected by land cover changes or the atmospheric CO<sub>2</sub> concentration, which is increased by greenhouse gas emissions. Secondly, those parameters are of special interest that are subject to natural variability, such as insolation. We will first concentrate on the occurrence of a saddle node bifurcation in dependence on the planetary albedo  $A_{sys}$  (cf. Fig. 2.3). The present day value of  $A_{sys} = 0.467$  is also plotted in Fig. 2.3 for comparison. Increasing  $A_{sys}$  from today's value on leads to a sudden change from a wet to a much dryer regime that is reached through a saddle-node bifurcation (point SN1 in Fig. 2.3). Here the stable solution loses its stability until it again becomes stable through a second saddle node (SN2 in Fig. 2.3). This dry regime is characterised by a much weaker hydrological cycle as a result of the reduced heating over land as the planetary albedo  $A_{sys}$  and therefore the reflected solar radiation is increased. There is also a certain range of  $A_{sys}$  (between SN2 and SN1), where a bistable regime is present, so switches from wet to dry regimes are also possible without

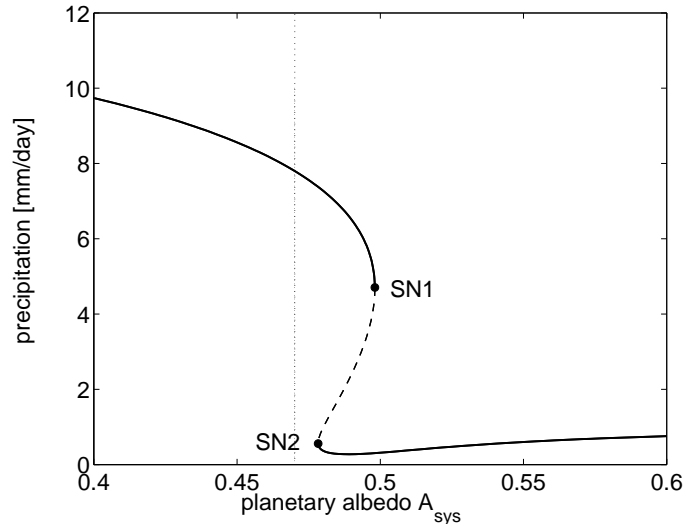


Figure 2.3: Bifurcation diagram for the summer monsoon precipitation in dependence on the planetary albedo  $A_{sys}$  for the basic model M1. SN1 and SN2 mark the saddle node bifurcations (with  $A_{sys,SN1} = 0.498$ ), the vertical dotted line the present-day value of  $A_{sys} = 0.47$ .

reaching the bifurcation point but due to suddenly changing boundary conditions through climate change for example. The bistability brings about a hysteresis, implying that once the monsoon has undergone a transition to the dry regime, the planetary albedo has to be reduced below the second bifurcation point SN2, until the system can operate in the wet regime again. This would certainly affect the Indian population and requires mitigation strategies, as no easy “step backwards” is possible.

The mechanism that is responsible for the bifurcation can be interpreted in terms of the moisture-advection feedback. During the summer the monsoon circulation transports the humid air from the surrounding Indian Ocean towards India. As the land over India is much warmer than over the ocean, the air rises, cools down at the same time and condensates. This condensation leads to the release of large amounts of heat in the troposphere, entailing a strengthening of the upper level pressure gradient between land and ocean and in turn of the upper branch of the monsoon circulation. Increasing the albedo of the system leads to a cooling of the temperatures over land in relation to those over the ocean. When the land-sea pressure gradient gets too small the wet air is no longer carried inland and the monsoon circulation breaks down. Once the system resides in the dry regime it needs a larger temperature gradient or a smaller value for the albedo than for the destabilisation to get the monsoon circulation started again, leading to the observed hysteresis. This regime shift can partly be seen in the seasonal cycle of the monsoon, where in July suddenly the onset on the monsoon begins, until in September/October the land-ocean temperature gradient gets too small to sustain the monsoon advection.

The second saddle node bifurcation results from a transition from summer to winter regime, whereby the vertical velocity  $w$  changes its sign from positive to negative. This implies a different set-up with inversed advection terms in the model. As this is an intrinsic

“built-in” effect of the model, we do not investigate this point any further, except for the fact of the possibility of a bistable regime.

The question remains whether the value of the planetary albedo at which the regime transition occurs can be reached by plausible anthropogenic perturbations. This question was already addressed in Zickfeld (2004), p. 59 and we will sum up the main results here. The planetary albedo that characterises the reflexivity of the Earth at the top of the atmosphere and is used as the bifurcation parameter here, can be altered by anthropogenic actions. This includes the effect of changed land-cover conditions, such as forest clearance would bring about. Moreover, increasing concentrations of scattering aerosol, caused by fires and the consumption of fossil fuels, would affect the planetary albedo. With an estimate of the direct and indirect effect of the scattering aerosols an increase of the planetary albedo of about 9% (from 0.47 to 0.51) can be reached. Land-cover changes towards desert attain a similar value (0.50). As we will see in section 2.3.3, higher CO<sub>2</sub> concentrations shift the bifurcation point further away from today’s value. Nevertheless, as for a CO<sub>2</sub> concentration of 560 ppm (corresponding to a doubling of the pre-industrial value) the bifurcation point lies at a value of 0.51. One can conclude that aerosol emissions alone or in combination with processes affecting the land surface such as desertification could push the system across the critical threshold even under increased CO<sub>2</sub> conditions.

Another possible scenario to be considered in this context is the “roller coaster effect” that was described in Zickfeld et al. (2005). As the aerosols and the CO<sub>2</sub> concentration have opposite effects on the intensity of the monsoon, a scenario is plausible where initially the intensity of the monsoon is reduced due to continuing aerosol emissions. On the other hand, as CO<sub>2</sub> concentration rise and aerosol control strategies begin to take effect, this development could push the system back into a wet monsoon regime within a very short time.

Despite the fact that the model is a conceptual one that ignores e.g. the regional and global-scale effects, it includes the most important processes and we can therefore rely on the qualitative model results. Although the quantitative results have to be regarded with care, we can highlight the most influential mechanisms and parameters that determine the uncertainty with respect to the position of the bifurcation and the occurrence of the bifurcation at all. This will be done in detail in section 2.5 and 2.4. Although the probability of such a breakdown cannot be inferred from this reduced form model, the possibility of this extreme event has to be taken into account when analysing the Indian monsoon under global change.

In the remaining sections of this chapter we will go beyond the analysis that we presented in Zickfeld et al. (2005): we will derive the normal form of the bifurcation, highlight the possible relevance of the bifurcation for paleo times, and affiliate a systematic uncertainty analysis of the bifurcation point.

### 2.3.2 Normal form of the bifurcation

To gain an understanding of the entire mechanism behind the bifurcation, we will reduce the model in a physical way. We assume that we have an infinite reservoir of the soil moisture, so the two soil layers merge to one and their soil moistures  $w_1, w_2$  are set constant.

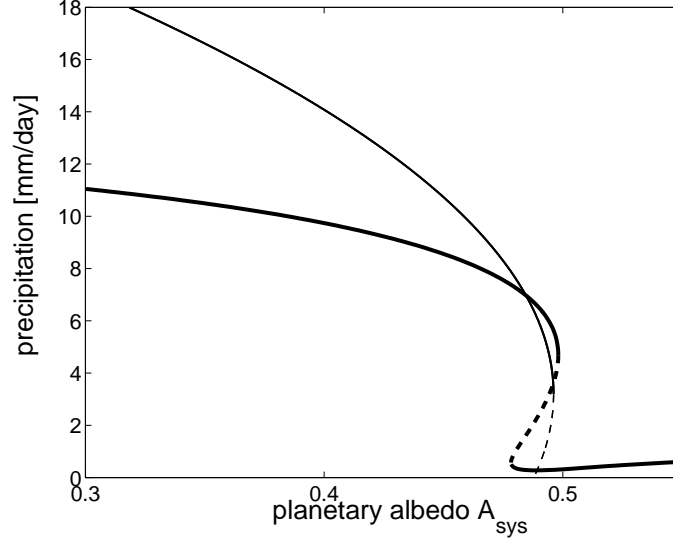


Figure 2.4: Comparison of the bifurcation diagram for the basic model M1 and the simplified version. The thick line represents the bifurcation diagram with respect to the planetary albedo  $A_{sys}$  for the basic model M1, adopted from Fig. 2.3, the thin line shows the bifurcation diagram for the model with the simplifications described in Eqs. (2.22) and (2.23).

The net outgoing longwave radiation at the top of the atmosphere  $F_{\uparrow}^{LW,TA}$  is no longer dependent on the temperature over India, but is as well considered to be constant with  $F_{\uparrow}^{LW,TA} = A_0$  (cf. Eq. (2.12)). The dependence of the lapse rate from the temperature and the specific humidity is ignored, so that  $\Gamma = \Gamma_0$  (cf. Eq. (2.20)). The evapotranspiration is calculated as the difference between precipitation and runoff with  $E = P - R$ , which holds for the steady state (cf. Eq. (2.3)). Furthermore, as we consider the monsoon circulation to be the main driver for the advection of heat and moisture, we neglect the dependence on the specific humidity  $q_a$  in the term for the advection of moisture, by setting  $q_a$  constant here with  $q_a = q_{a,const}$ .

We end up with a two dimensional differential equation for  $q_a$  and  $T_a$  (for  $T_a > T_{oc}$ ):

$$\dot{q}_a = -K_r w_1 P + C_{Adv} (T_a - T_{oc}) \quad (2.22)$$

$$\begin{aligned} \dot{T}_a = & L K_r w_1 P + F_{\downarrow}^{SL,TA} (1 - A_{sys}) - F_{\uparrow}^{LW,TA} \\ & - C_{AdT} (T_a - T_{oc})^2 + C_{AdT} C_{\gamma} (T_a - T_{oc}) \end{aligned} \quad (2.23)$$

where  $C_{Adv}$  and  $C_{AdT}$  sum up the constant factors of the advection terms of moisture and heat and are given in appendix B.  $C_{\gamma}$  is a constant that depends amongst others from the lapse rate coefficient  $\Gamma_0$  and the box length  $L$  of India at the boundaries (cf. appendix B). This system still leads to the occurrence of the bifurcation (cf. Fig. 2.4), so despite these assumptions we qualitatively find the same behaviour of the system. We then consider a steady state for the specific humidity with the same argument as before when we set  $q_a$  constant in the advection term of moisture, which will certainly hold in the vicinity of the

bifurcation. This gives us an expression for the precipitation  $P$  that can substitute the term for  $P$  in the differential equation for  $T_a$ . This further reduction results in an ODE for  $T_a$ :

$$\dot{T}_a = -C_{AdT} (T_a - T_{oc})^2 + (C_{Adv} L + C_{AdT} C_\gamma) (T_a - T_{oc}) + F_{\downarrow}^{SL,TA} (1 - A_{sys}) - F_{\uparrow}^{LW,TA}. \quad (2.24)$$

This expression can be simplified by introducing a new variable  $\tilde{T}_a$  with

$$\tilde{T}_a = \left( C_{AdT} (T_a - T_{oc}) - \frac{C_{Adv} L + C_{AdT} C_\gamma}{2} \right), \quad (2.25)$$

that leads to an ODE for  $\tilde{T}_a$ :

$$\dot{\tilde{T}}_a = \mu - \tilde{T}_a^2, \quad (2.26)$$

with

$$\mu = \left( \frac{C_{Adv} L + C_{AdT} C_\gamma}{2} \right)^2 + C_{AdT} \left( F_{\downarrow}^{SL,TA} (1 - A_{sys}) - F_{\uparrow}^{LW,TA} \right). \quad (2.27)$$

Eq. (2.26) is exactly the normal form of a saddle node bifurcation in  $\tilde{T}_a$  with the bifurcation parameter  $\mu$  (Guckenheimer and Holmes 1996, e.g.). For  $\mu > 0$  a positive stable and a negative unstable solution exists that collide in a saddle node bifurcation at  $\mu = 0$  and vanish for  $\mu < 0$ .

The fact that the – scaled and centered – temperature difference  $(T_a - T_{oc})$  is the crucial variable strengthens the assumption that this is the main driver for the monsoon circulation. It is obvious that when the planetary albedo reaches the bifurcation point  $A_{sys,crit}$  at

$$A_{sys,crit} = 1 + \frac{(C_{Adv} L + C_{AdT} C_\gamma)^2}{4 C_{AdT} F_{\downarrow}^{SL,TA}} - \frac{F_{\uparrow}^{LW,TA}}{F_{\downarrow}^{SL,TA}}, \quad (2.28)$$

$\mu$  crosses from positive to negative values and the physical solution for  $\tilde{T}_a$  in Eq. (2.26) disappears. From Eq. (2.27) it can also be seen that the outgoing longwave radiation  $F_{\uparrow}^{LW,TA}$  and the incident solar radiation at the top of the atmosphere  $F_{\downarrow}^{SL,TA}$  play an important role for the location of the bifurcation and can as well serve as bifurcation parameters, just as most other parameters in this functional relationship.

Analysing the parameters in the factors  $C_{Adv}$  and  $C_{AdT}$  in detail shows that they depend amongst others on the box length  $L$  of India at the boundaries, which controls the amount of heat and moisture exchanged between ocean and land, on the specific humidity  $q_{oc}$  over the ocean boundary, which determines the amount of moisture being advected, on the height of the planetary boundary layer  $h_{PBL}$ , which determines the height of the ascending branch of the monsoon circulation, and on the cross-isobar angle  $\sin(\alpha_0)$ , which influences the strength of the monsoon circulation (cf. Eq. (2.15)). This analysis shows the strong dependence of the bifurcation from those values, which determine the heat



balance of the system either via the advection of heat and moisture ( $C_{Adv}$  and  $C_{AdT}$ ) or directly through the incoming and out-going radiation. The collective dependence of the bifurcation point on the large number of parameters will be scrutinised in section 2.5.

### 2.3.3 Relevance of the bifurcation for paleo times

From Eq. (2.1) it can be deduced that all terms on the right hand side that are not dependent on one of the four variables can serve as bifurcation parameters with respect to which the saddle-node bifurcation occurs. In a physical sense these are those parameters that influence the heat balance of the system. As we have seen from the generalised bifurcation parameter  $\mu$  of the normal form (cf. Eq. (2.27)), two important parameters are the incoming solar radiation  $F_{\downarrow}^{SL,TA}$  and the  $\text{CO}_2$  concentration  $p\text{CO}_2$  that influences the outgoing longwave radiation at the top of the atmosphere  $F_{\uparrow}^{LW,TA}$  (cf. Eq. (2.12)). These are interesting parameters when considering that during the last 300,000 years both have varied in a wide range. Studies indicate that during the last glacial period (Burns et al. 2003) and the Holocene (Gupta et al. 2003) the Indian monsoon has undergone a number of abrupt changes. A proxy from the Arabian Sea suggests that several abrupt changes of the monsoon occurred during the last 350,000 years (Wang et al. 2005; Prabhu et al. 2004). It is a matter of debate, whether these abrupt changes in the monsoon intensity are linked to abrupt changes in other parts of the climate system, e.g. the North Atlantic oscillation (Gupta et al. 2003), or whether these changes could be linked to variations of the solar activity, as put forward by Bond et al. (2001) and Sarnthein et al. (2002). A 160,000 year stalagmite record from Dongge Cave, China, shows impressively a high correlation between abrupt changes in the Asian monsoon and the solar radiation (Yuan et al. 2004).

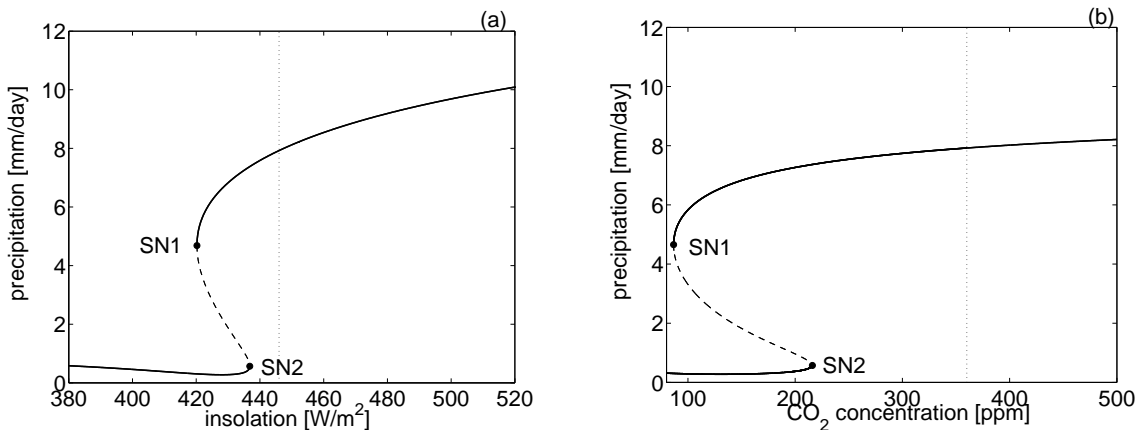


Figure 2.5: Bifurcation diagram for the summer monsoon precipitation in dependence on (a) the insolation  $F_{\downarrow}^{SL,TA}$  and (b) the  $\text{CO}_2$  concentration. SN1 and SN2 mark the saddle node bifurcations, the vertical dotted line the present day value.

With the model of the Indian summer monsoon we can show that an abrupt change of the monsoon intensity could indeed be triggered by a change in insolation. If the incoming

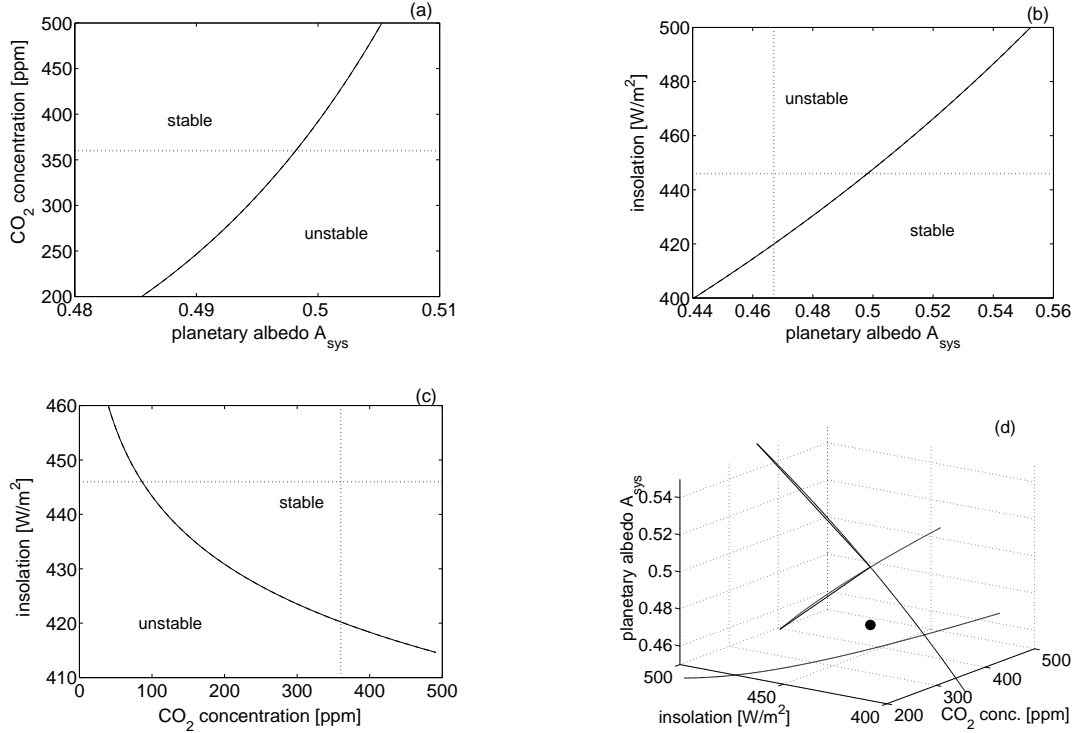


Figure 2.6: Following of the saddle-node bifurcation SN1 in two parameter directions: (a) SN1 for CO<sub>2</sub> concentration against planetary albedo  $A_{sys}$ , (b) SN1 for insolation against planetary albedo  $A_{sys}$ , (c) SN1 for insolation against CO<sub>2</sub> concentration, (d) cumulated dependencies of SN1 from (a)-(c) in a 3-D plot. The dotted line and the thick dot, respectively, mark the present day value in each case. The second saddle-node bifurcation SN2 is neglected here. Stable and unstable regimes are indicated.

solar energy is too small, the monsoon circulation can no longer be sustained and shifts to a dry regime with less precipitation. A destabilisation of the monsoon occurs at a critical value of  $420 \text{ W m}^{-2}$  (Fig. 2.5a) compared to the present day value of  $446 \text{ W m}^{-2}$  and to the observed range for paleo times of about  $420 \text{ W m}^{-2}$  to  $510 \text{ W m}^{-2}$  for June insolation at  $20^\circ\text{N}$  (Berger 1978). In the study by Yuan et al. (2004) the abrupt changes occur at an insolation of about  $460 \text{ W m}^{-2}$  but to compare these values, we would have to adjust the boundary conditions to interglacial conditions. We will refrain from this here, as our focus is more on the entire mechanism than on the absolute value.

A similar picture with a regime shift in precipitation arises when the CO<sub>2</sub> concentration is chosen as the bifurcation parameter (Fig. 2.5b). A lower value for the CO<sub>2</sub> concentration increases the outgoing radiation and decreases the heat budget of the monsoon and therefore reaches the bifurcation point. Increasing CO<sub>2</sub> concentrations, on the other hand, would increase the summer precipitation although the slope is not very steep in the vicinity of today's value. Nevertheless, the increase of summer precipitation with increasing CO<sub>2</sub> concentrations could play a role when considering the “roller coaster effect” mentioned before.

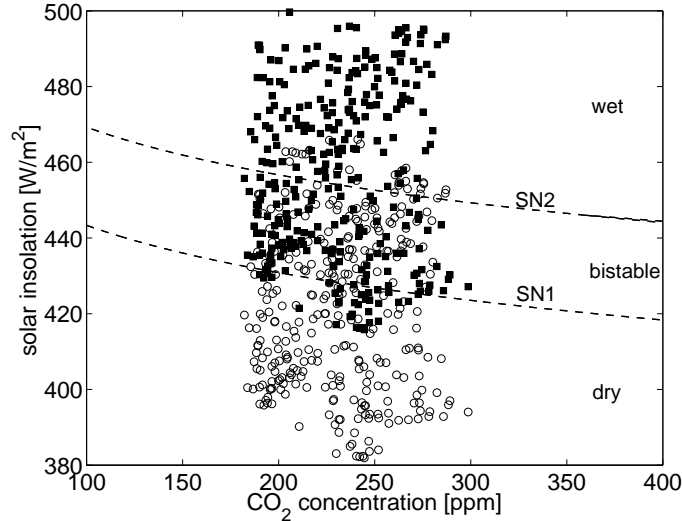


Figure 2.7: Same plot as in Fig. 2.6c but with paleo data for insolation against  $\text{CO}_2$  concentration. The dashed lines mark the saddle node SN1 and SN2, the black squares symbolise the data for insolation in June at  $15^\circ\text{N}$ , the circles the ones at  $5^\circ\text{N}$ . The points that lie below the dashed line of SN1 indicate possible states of the dry monsoon regime, the points between SN1 and SN2 are in the bistable regime, where a wet as well as a dry monsoon is possible, and the points above SN2 are in the wet regime (cf. Fig. 2.5a). The data are from Barnola et al. (1987) for the  $\text{CO}_2$  concentration and from Berger (1987) for the insolation.

Following the saddle node bifurcation in two parameter directions (cf. Fig. 2.6a,b) indicates that the bifurcation point exists throughout the entire possible range of historically observed insolation and  $\text{CO}_2$  concentrations that lie between 180 and 300 ppm for the last 420,000 years (Petit et al. 1999). For lower  $\text{CO}_2$  concentrations than today the bifurcation point SN1 for the planetary albedo is closer to today's value and the other way round for higher  $\text{CO}_2$  concentrations than today. An interesting point is the simultaneous dependence of the bifurcation point from the  $\text{CO}_2$  concentration and the insolation (Fig. 2.6c). In situations with a high (low)  $\text{CO}_2$  concentration and a low (high) insolation the system can reach the bifurcation point. To investigate the relevance for paleo times, we analyse the observed values over the last 300,000 years for  $\text{CO}_2$  concentration and insolation (Fig. 2.7). The data used here are the  $\text{CO}_2$  concentrations from the Vostok ice core (Barnola et al. 1987) and the insolation calculated after Berger (1978). Indeed, there are times when an abrupt change could have occurred due to this mechanism, as indicated in Figs. 2.7 and 2.8. Paleoclimate records of the Indian monsoon are rare, but recently Prabhu et al. (2004) presented with 200-ka the longest pollen record so far. This study indicates some changes of the Indian monsoon system between wet and dry regimes. The regime transitions occurred at about 30, 70, and 180 ka BP (from dry to wet) and at 10, 55, and 130 ka BP (from wet to dry). Some of these transitions are at similar times as the ones where in our model  $\text{CO}_2$  concentration and insolation provide the possibility of a regime shift. For the correct interpretation and estimation of the length of these different

phases, one must also keep in mind the hysteresis, implying that once the system resides in the dry regime it has to be pushed above the saddle node SN2 again (cf. Fig. 2.7).

To come up with a more robust conclusion, we would have to adopt the boundary conditions to paleo climate that we ignored for this preliminary estimation. Here we only want to motivate and demonstrate the possibility of an abrupt monsoon transition from a wet to a dry regime in dependence on changing boundary conditions that could have been important in the past.

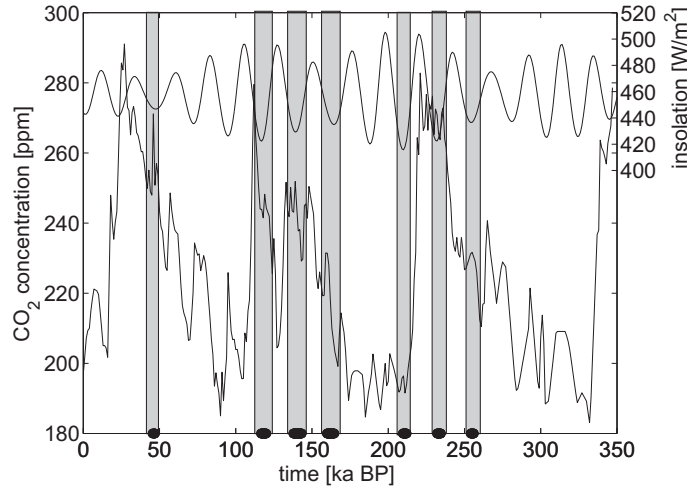


Figure 2.8: Time series of CO<sub>2</sub> concentration and insolation in June at 15°N. The grey bars mark the times, when the data fall below the saddle node line SN1 from Fig. 2.7, indicating a dry regime with a preceding regime shift from wet to dry. The data are from Barnola et al. (1987) for the CO<sub>2</sub> concentration and from Berger (1987) for the insolation.

## 2.4 Uncertainty analysis of the bifurcation: the model hierarchy

We have seen that all processes that alter the heat budget of the system are relevant for the occurrence of the bifurcation. In the following uncertainty analysis we will focus on the processes and parameterisations (cf. Eq. (1.2)) in discrimination to an in-depth parameter study that will be carried on in section 2.5. Here we want to address the question whether the bifurcation is robust against changes of parameterisations and against an increasing number of represented processes. These processes include e.g. the explicit formulation of the Tibetan Plateau or the dependence of the vegetation cover on precipitation. Bit by bit we extend the model by implementing more and more processes, starting with the basic model M1 described in section 2.3.1 and successively investigate the more sophisticated model versions M2, M3, and M4. This analysis results in the examination of a model hierarchy with increasing complexity.

So far we have analysed the steady state of the summer monsoon model and have neglected the dependence on the seasonal cycle in the model. We implement the seasonal

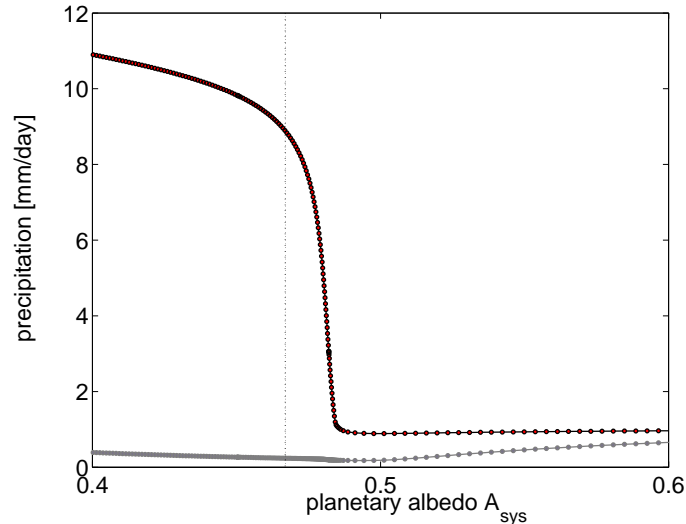


Figure 2.9: Bifurcation diagram for the monsoon precipitation in dependence on the planetary albedo  $A_{sys}$  for the basic model M1, whereas the boundary conditions in the model evolve according to a seasonal cycle. The black (grey), dotted line marks the maximum (minimum) of the stable periodic orbit, which corresponds to summer (winter) conditions. The vertical dotted line is the present day value. Compare with Fig. 2.3.

cycle for the boundary conditions of the ocean temperature  $T_{oc}$ , the relative humidity  $f_{oc}$ , the cloudiness  $N_{oc}$  over the ocean, and the incoming solar radiation  $F_{\downarrow}^{SL,TA}$ . In the system with the consideration of the seasonal cycle we also discover an abrupt transition from a wet to a dry summer regime (cf. Fig. 2.9). The saddle node bifurcation vanishes; nonetheless, a strong nonlinear dependence of precipitation on the planetary albedo can be deduced that goes along with a steep decrease in rainfall within a small range of the planetary albedo that could be crossed within a very short time. Interestingly, the point of the regime shift lies nearer to today's value in comparison to the steady state analysis.

As the implementation of the seasonal cycle gives qualitatively no other picture, we proceed with the investigation of the system fixed to summer conditions, as this system allows us to compare one particular point (the saddle node) between different model versions in this setting.

#### 2.4.1 Model M2: Calculation of clouds and planetary albedo

In the basic version M1 of the model (cf. section 2.3.1) the total cloudiness  $N$  is prescribed, which constitutes a strong simplification as it ignores the influence of cumulus and stratus clouds, of the relative humidity, and of the vertical velocity on cloud cover. In the first upgrade of the model we will therefore explicitly model the cloudiness  $N$ . This brings about that the planetary albedo  $A_{sys}(N)$  is no longer modelled as a constant, since it depends on cumulus and stratus clouds as well: Eq. (2.5) shows that  $A_{sys}$  is a function the albedos of stratus and cumulus clouds  $A_{cu}$  and  $A_{st}$  and of the clear-sky atmosphere  $A_{cs}$ , again depending on a number of parameters (cf. Eq. (2.7) and (2.10)). This extension

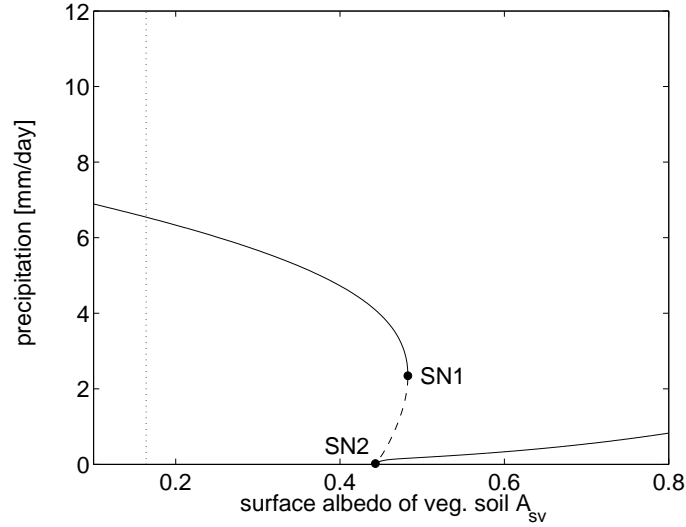


Figure 2.10: Bifurcation diagram for the summer monsoon precipitation in dependence on the albedo of the vegetated soil  $A_{sv}$  for model M2. The saddle node bifurcation is reached at  $A_{sv} = 0.483$ . The vertical dotted line marks the present day value of  $A_{sv}=0.164$ .

entails that here and in the following the albedo of the vegetated soil  $A_{sv}$  serves as the bifurcation parameter. In this model version  $A_{sv}$  is equal to the surface albedo  $A_s$  as the fractional vegetation cover is set equal to  $V = 1$  unless the precipitation falls below a critical threshold (cf. Eq. (2.8) and (2.9)). This model version M2 now includes the items 1. and 2. from page 18 that were ignored in the basic formulation of model M1.

The implementation of these parameterisations does not alter the qualitative behaviour substantially, but allows for a more detailed analysis of the contribution from the individual processes. Despite these additional parameterisations the bifurcation point is maintained. It is reached at  $A_{sv} = 0.483$  (cf. Fig. 2.10), a value that is far from the present day value of  $A_{sv} = 0.164$  determined from satellite data (MODIS 2006). The implemented explicit calculation of the clouds leads to a stabilising (negative) feedback mechanism that operates in the following way: less precipitation due to a higher albedo leads to lower amounts of stratus and cumulus clouds, which decreases the planetary albedo and in return brings about more precipitation. This mechanism shifts the bifurcation point to higher values of the albedo.

#### 2.4.2 Model M3: Consideration of Hadley and trade wind circulation

The major change in the version M3 of the model affects the wind driven circulation, as Hadley and trade wind circulation are considered. Additionally, in this model set-up the turnover time of water in the atmosphere  $\tau_P$  (cf. Eq. (2.18)) is explicitly calculated as a function of the vertical velocity  $w$  and is no longer constant. The Hadley circulation  $v_H$  is modelled with an influence on the vertical velocity  $w$  (cf. Eq. (2.17)), the total wind velocity  $v_0$  at the surface, and on the advection of heat and moisture. The trade winds affect the same mechanisms apart from the vertical velocity since they are homogenous across India.

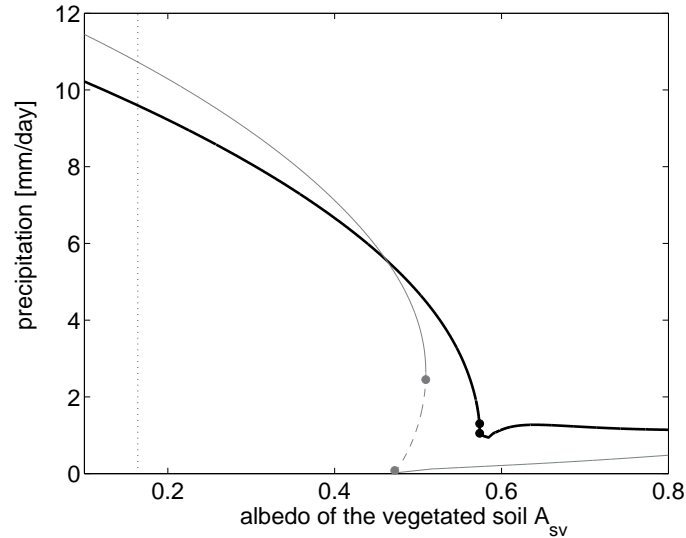


Figure 2.11: Bifurcation diagram for the summer monsoon precipitation in dependence on the albedo of the vegetated soil  $A_{sv}$  for model M3 (thick black curve) with the inclusion of the large scale circulations and the explicit calculation of the lifetime of clouds. The bifurcation point is at  $A_{sv} = 0.573$ . The thin grey curve is the bifurcation diagram of model M3 only with the explicit calculation of the lifetime of clouds but without the implementation of Hadley and trade wind circulation. The vertical dotted line marks the present day value of  $A_{sv}=0.164$ .

With these parameterisations the model now additionally includes the neglected items 3.–5. from page 18.

Fig. 2.11 shows that the bifurcation point is preserved<sup>5</sup> but moves even further to higher values of the albedo of the vegetated soil  $A_{sv}$ . In comparison to the model M2 (cf. section 2.4.1) the precipitation is always higher, which can be attributed to the explicit calculation of the lifetime of the clouds  $\tau_p$ . The shift of the bifurcation point to higher values is mainly due to the inclusion of the large-scale circulations, as indicated in Fig. 2.11. Moreover, the Hadley and trade winds decrease the steepness of the regime shift and let nearly vanish the bistable regime.

The Hadley and the trade wind circulation have a major influence on the advection of heat and moisture. Two conflicting effects arise from these additional circulations: on the one hand, both circulations deliver heat away from India to the surrounding ocean, resulting in a decline of the land-sea temperature gradient and therefore in a decline of the precipitation (compare the black and the grey line in Fig. 2.11). On the other hand, the Hadley and trade wind circulations deliver additional moisture to India but as the difference of the relative humidity between land and adjacent ocean and therefore the contribution of the trade winds is negative for lower values of the albedo, this effect can only come into play for albedo values of  $A_{sv} > 0.5$  and results in a shift of the bifurcation point to higher values of the albedo.

<sup>5</sup>This holds only, when the surface velocities for Hadley and trade wind circulation are not too high, indicating an important role of the evapotranspiration that depends on the surface velocity.

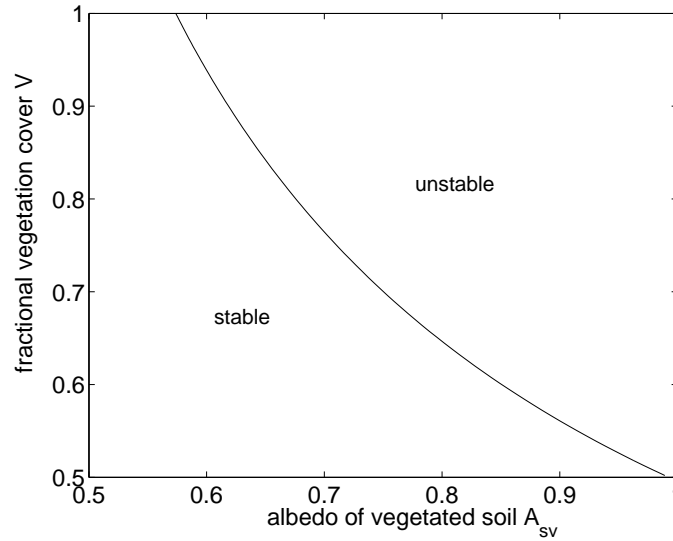


Figure 2.12: Path following of the saddle node bifurcation for model M3 in the two parameter directions for the albedo of the vegetated soil  $A_{sv}$  and for the fractional vegetation cover  $V$  (for  $P > P_{cr}$ ). Here  $V$  is considered as a constant parameter.

### 2.4.3 Model M4: Explicit modelling of an active vegetation and the Tibetan Plateau

In this model version we will additionally consider item 6. and 7. from page 18. At the first place, this includes the explicit calculation of the fractional vegetation cover  $V$  that influences the surface albedo (cf. Eq. (2.8)) and the evapotranspiration, where soil types and vegetation characteristics play an important role. Fig. 2.12 shows that the fractional vegetation cover  $V$ , when considering  $V$  as a constant parameter, has a decisive influence on the location of the bifurcation point. We will now include the dependence of the vegetation on precipitation as described in Eq. (2.9). The vegetation fraction determines the fraction of the albedo of the vegetated soil  $A_{sv}$  and of the bare soil  $A_b$  in the calculation of the surface albedo (cf. Eq. (2.8)). The lower the fractional vegetation cover, the higher is the required value of the albedo of the vegetated soil  $A_{sv}$  to reach the bifurcation point given a fixed value for  $A_b$ , as  $A_b$  is generally lower than  $A_{sv}$ . It appears that the influence of the precipitation on the vegetation lets vanish the bifurcation point (cf. Fig. 2.13). The loss of the bifurcation can be explained by the stabilising feedback of the vegetation. When precipitation declines, the vegetation fraction declines as well, which decreases the surface albedo  $A_s$  and in turn increases the precipitation, leading to a stabilisation through the negative feedback.

Two major limitations concerning this approach of including the vegetation are obvious: in the first place, the parameterisation of the vegetation in dependence of precipitation (cf. Eq. 2.9) is a very simplified one with more or less an on-off switch, which is only valid for conditions e.g. as in the Sahara. Secondly, as the vegetation certainly determines the albedo of the vegetated soil  $A_{sv}$ , it would be more appropriate to consider this dependence, so that the vegetation itself can serve as a bifurcation parameter. In addition with a



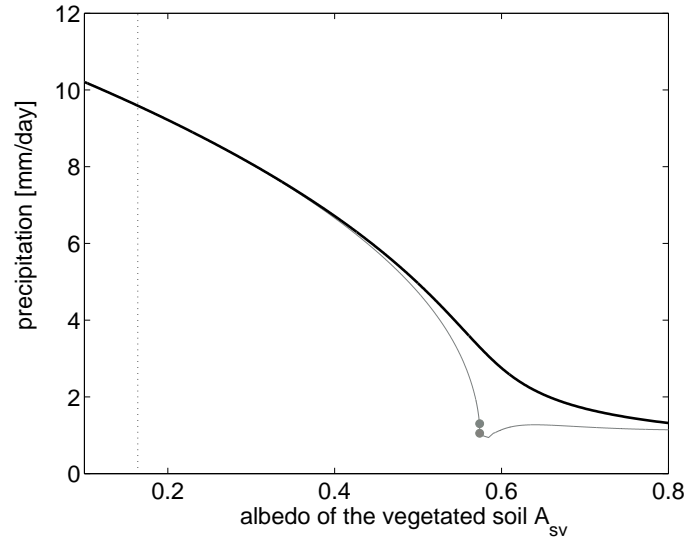


Figure 2.13: Bifurcation diagram for the summer monsoon precipitation in dependence on the albedo of the vegetated soil  $A_{sv}$  for model M4 (thick black curve) with an active vegetation. The dependence of the vegetation on precipitation is captured explicitly. The thin grey curve is the bifurcation diagram of model M3 as in Fig. 2.11 with a constant vegetation of  $V = 1$ . The vertical dotted line marks the present day value of  $A_{sv}=0.164$ .

more sophisticated parameterisation concerning the dependence of precipitation, this could result in a model version, where the bifurcation point is sustained.

The last parameterisation to consider concerns the boundary conditions and implies the need for an explicit modelling of the Tibetan Plateau. The ocean boundaries differ only in the cloud covers and a higher temperature  $T_E$  at the eastern ocean boundary. This consideration changes the bifurcation diagram only marginally. The modelling of the Tibetan Plateau, however, where the temperature difference between the box and the northern boundary is taken at the height of the Tibetan Plateau, has an influence on the bifurcation behaviour. The bifurcation point vanishes in this formulation of the model (cf. Fig. 2.14), which also holds for a constant vegetation. For lower values of the albedo the precipitation is lower than in model M3, which is due to the fact that the air over the Tibetan Plateau is dryer than the air over India. It therefore transports moisture away from the Indian subcontinent.

In our model the contribution of the Tibetan Plateau is not that influential as reported from other studies (Yanai et al. 1992; Ye and Wu 1998; Wu and Zhang 1998, e.g.). We therefore implement another formulation of Tibet with the inclusion of the katabatic winds (Prantl 1942), which describe the flow from the high elevations of mountains or plateaus down their slopes to the planes below, but the influence remains small. To account for the high relevance of the Tibetan Plateau for the Indian monsoon, an idea could be to adopt another point of view, where the Tibetan Plateau is no longer modelled as a boundary condition but as a second box in the model. This is also an important point in the context of altering conditions under climate change (e.g. thawing of permafrost, land use changes,

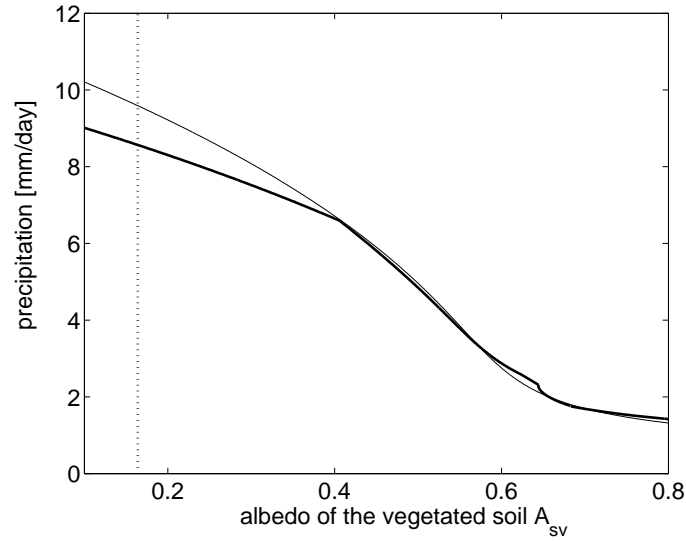


Figure 2.14: Bifurcation diagram for the summer monsoon precipitation in dependence on the albedo of the vegetated soil  $A_{sv}$  for model M4 (thick black curve) with an active vegetation and the inclusion of the Tibetan Plateau. The thin grey curve is the bifurcation diagram of this model as in Fig. 2.13 with an active vegetation but without the Tibetan Plateau. The sharp bend at  $A_{sv} = 0.42$  and  $0.7$  is due to discontinuities in some expressions.

etc.) over the Tibetan Plateau, which will certainly influence the monsoon dynamics.

All in this, the structural uncertainty analysis related to parameterisations has shown that the bifurcation behaviour is sustained against a number of considered processes. With the inclusion of the explicit formulation of the vegetation cover and the Tibetan Plateau, however, the bifurcation point vanishes. On the other hand, the qualitative behaviour including a strong decrease in precipitation with increasing surface albedo can be observed in all model versions. In the next section we will analyse the parameter uncertainties in this model in detail.

## 2.5 Uncertainty analysis of the bifurcation: multi-run parameter uncertainty analysis

In this section we will introduce the development and application of a novel method to quantify the influence of parameter uncertainties on the occurrence of a bifurcation point. The innovative point is that this technique allows investigating the position of the bifurcation point in the whole parameter space. As a general method it can be applied to many systems; in this chapter we will exemplarily adopt this method to test the robustness of the bifurcation point in the monsoon model.

Whereas in the last section we have analysed the structural uncertainty of the model in detail, we now want to investigate the influence of parameter uncertainty and deepen the discussion of section 2.3, where a number of parameters were shown to influence the position of the bifurcation. To estimate the relevance of the bifurcation it is not just important to analyse whether this point could be reached by anthropogenic perturbations, as briefly investigated in section 2.3.1. Moreover, it is indispensable to perform a multi parameter uncertainty analysis to investigate the dependence of the model results on the choice of the parameters to test the robustness of the occurrence of the bifurcation point. This brings about the need to follow the bifurcation point in several parameter directions.

### 2.5.1 Method

The bifurcation analysis program AUTO (Doedel (1981), cf. section 2.3.1) provides the possibility to follow such a point in two parameter directions, as it was done e.g. in Fig. 2.6a-c. CONTENT (Kuznetsov et al. 1997), another bifurcation analysis software, is indeed able to handle a continuation in three parameter directions, but that is still not enough for our model with nearly 60 parameters. To realise the multi-parameter analysis we develop a new method based on the combination of a multi-run simulation environment with AUTO that will be described in the following.

As AUTO depends on a stable state of the system as a starting point, we first integrate the model until it reaches equilibrium. We then start the qualitative analysis using AUTO, run the bifurcation analysis, and repeat this for several parameter settings to scan the high dimensional parameter space for the occurrence of the bifurcation. In detail, the multi parameter bifurcation analysis has to carry out the following steps:

1. provide a (large) set of parameters with their uncertainty ranges and draw a sample from the resulting parameter space according to the goal of the analysis,
2. choose one point from the sample and find the equilibrium state for this specific parameter setting,
3. start AUTO with this equilibrium state and run a bifurcation analysis against the specified bifurcation parameter,
4. repeat step 2. and 3. for all parameter sampling points as defined in step 1.

The processing of these steps is realised with the simulation environment SimEnv (Flechsig et al. 2005; SimEnv 2006) that draws samples from the parameter space, where each sample corresponds to the goal of the sensitivity experiment (step 1). Different sampling strategies are applied that correspond with methods to deal with model parameter sensitivity and uncertainty. The model under investigation is then interfaced to the simulation environment that successively performs steps 2.-4. During experiment post-processing, the combined state and parameter space is investigated and sensitivity and uncertainty measures are derived. Here sensitivity is related to the bifurcation point of the system and it is analysed whether and at which value the saddle node bifurcation occurs for a certain parameter setting.

To the best of our knowledge, such a systematic investigation of a bifurcation point has not been performed anywhere else before. As this method is model-independent, it can be used for a variety of models (e.g. for a box model of the thermohaline circulation), where the robustness of a certain bifurcation point is of interest. The only constraint is related to the dimensionality of the model that is restricted by AUTO to a limited number of ODEs and parameters.

### 2.5.2 Model and parameters

The model applied for this investigation is the model M2 instead of the basic model M1, as it includes the explicit formulation of clouds and allows to discriminate between the different contributions to the planetary albedo (cf. section 2.4.1). We choose this model as it allows for a detailed analysis of single parameters that are subject to anthropogenic disturbances, which are important to study in terms of the integrated assessment of climate change. As in this model the fractional vegetation cover  $V$  is equal to 1 (for  $P > P_{cr}$ ), we regard the surface albedo  $A_s$  as the bifurcation parameter, which is equal to the surface albedo of the vegetated soil  $A_{sv}$  here (cf. Eq. (2.8)). The choice of a fixed bifurcation parameter in this multi parameter bifurcation analysis does not constitute a constraint. The same analysis can be carried out for different bifurcation parameters, where the surface albedo  $A_s$  is then regarded as a “regular” parameter.

We investigate 40 out of approximately 60 model parameters, listed in Table 2.1, that either influence the heat budget of the system, depend on anthropogenic influence, or are tuneable parameters in the model. Other parameters that are not included in this analysis are physical constants (e.g. the gravity constant  $g$ ) or have only an influence on the transient dynamics but not on the equilibrium state (e.g. the field capacities of the soil layers  $f_1$  and  $f_2$ ). We distinguish the parameters that refer to observational quantities (e.g. for the ocean temperature  $T_{oc}$ ) from the entire model parameters and determine the uncertainty ranges of the former by analysing the observed values for the period 1948-2004 from the NCAR/NCEP reanalysis (Kalnay et al. 1996) or by including future projections (e.g. for the CO<sub>2</sub> concentration  $pCO_2$ ). For the other parameters we simply assume a  $\pm 5\%$  or  $\pm 10\%$  deviation from the value in the reference model with the default values given in appendix A.2. The parameter ranges are chosen such that they are equally likely and associated with the same uncertainty. We assume that the parameters are equally distributed over their ranges, an assumption that certainly constitutes a bias, but as we

focus on qualitative changes this assumption does not affect our conclusions. Besides the full parameter set, denoted as  $P_{40}$  in the following, we will investigate subsets of the most influential parameters.

We will carry out the systematic approach starting with a *Monte Carlo analysis* that allows a study of the error propagation of the parameter uncertainties in the model. We proceed with a *global sensitivity analysis* to deduce the most influential parameters that is followed by a *deterministic parameter screening* to investigate how the model performs under changes of these parameters. These investigations cover the full range of multi parameter uncertainty analyses. Additionally, we investigate the effect of the anthropogenically influenced parameters in a separate parameter screening to tie up to the discussion whether the saddle node bifurcation can be reached by anthropogenic perturbations and whether the abrupt regime transition could be relevant under global change.

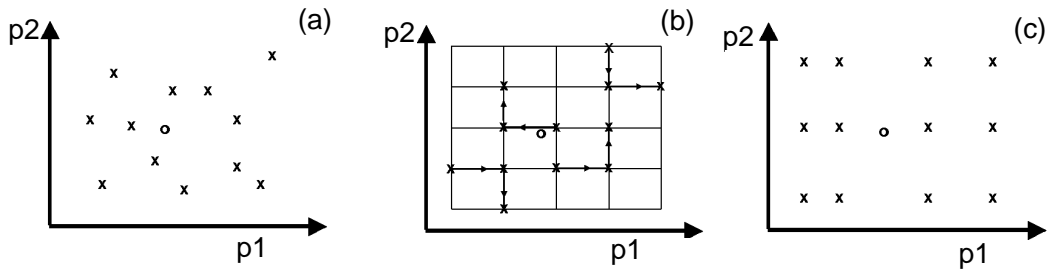


Figure 2.15: Applied SimEnv parameter space sampling strategies. Examples for a two-dimensional parameter space  $P_2=(p_1,p_2)$ : (a) Monte-Carlo analysis with a sampling according to probability density functions, (b) global sensitivity analysis to deduce a qualitative ranking of the parameters with respect to the bifurcation SN1, (c) deterministic parameter screening to investigate the model's behaviour. The point "o" marks the default value, the crosses "x" denote the sampling points. The sampling strategies are described in detail in the text.

### 2.5.3 Monte-Carlo analysis

A Monte Carlo analysis (MCA) relates uncertainties in parameter values to uncertainty in an output quantity and therefore demonstrates the error propagation through a model. As our model is a conceptual one we have – in contrast to similar studies with GCMs – the advantage that it requires only limited computational resources. We implement a Latin hypercube sampling (McKay et al. 1979) to reduce the total randomness (cf. Fig. 2.15a). For the parameter set  $P_{40}$  we perform 20,000 runs where 96.4% of them show a saddle node bifurcation, so the occurrence of the saddle node bifurcation is a very robust result in this model under parameter uncertainty and not just due to a specific choice of parameters. The distribution of the bifurcation points shows approximately a normal distribution around the mean value of  $A_s = 0.486$  (cf. Fig. 2.16). The standard deviation is  $\sigma = 0.04$ , which corresponds to about 10% of the mean value. The 5% and 95% quantile are at  $A_s = 0.56$  and  $A_s = 0.43$ . It is reasonable to discuss these results in relation to today's value for the surface albedo over India and to possible changes in this value. The present day value

of the surface albedo derived from satellite data (MODIS 2006) is approximately 0.164. The surface albedo has a possible range from  $A_s = 0.12$  for evergreen broadleaf trees to  $A_s = 0.3$  for desert (Dickinson et al. 1986). Hence, even conversion of the total land-cover to desert would not lead to a transgression of the bifurcation point. On the other hand, this shows that the uncertainty in the output of the model has nearly the same magnitude as the uncertainty concerning the value of the albedo due to different vegetation types.

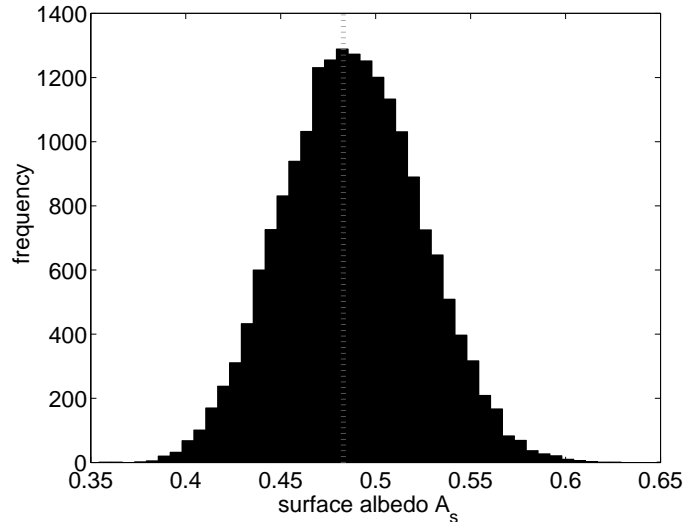


Figure 2.16: Frequency of the value of the surface albedo  $A_s$  at the bifurcation point SN1. Results from a Monte-Carlo analysis for the parameter set  $P_{40}$  sampled with a Latin hypercube scheme. The mean value is  $A_s = 0.487$ , the median lies at  $A_s = 0.486$ . The vertical dotted line at  $A_s = 0.483$  marks the default value of  $A_s$ , cf. Fig. 2.10.

#### 2.5.4 Global sensitivity analysis

The main idea of the global sensitivity analysis (GSA) is to identify those parameters that influence the model output the most (the least) and to come up with a qualitative ranking of the parameters according to their importance. In our case the sensitivity measures are related to the occurrence and the position of the bifurcation point. The method applied by SimEnv is the Morris method (Morris 1991), modified by Campolongo et al. (2005). For the GSA we again investigate the parameter set  $P_{40}$  with the specified ranges that are subdivided into  $m = 6$  equal intervals for each parameter here. On the resulting regular grid of  $40^{m+1}$  grid points the GSA randomly lays trajectories through this 40-dimensional space, whereby two adjacent points on a trajectory differ in one parameter  $p_i$  only. The points are simultaneously adjacent grid points and each  $p_i$  is varied only once on every trajectory. In the parameter space this results in trajectories with  $40+1$  points. For  $m = 4$  and two parameters this is exemplarily shown in Fig. 2.15b for four trajectories. Measured is the distance  $\Delta F_{ij}$  between the two values for the surface albedo  $A_s$  at the bifurcation point of the  $j^{\text{th}}$  trajectory with respect to the parameter  $p_i$  that is varied.

Table 2.1: Parameter set  $P_{40}$  with the ranges that are chosen for the sensitivity analyses. The entries in this list are ranked according to their importance deduced from the GSA: the first parameter is the most sensitive one, the last the one with the least influence.  $\mu$  is the mean of the absolute distance  $|\Delta F|$  (see text) with respect to the particular parameter. The last column categorises, which physical process or variable is influenced by the parameter:  $A_{cs}$  and  $A_{cl}$  indicates an influence on the albedo of the clear sky and the clouds, respectively,  $F_{\uparrow}$  on the outgoing radiation,  $\Gamma$  on the vertical temperature profile,  $h_{PBL}$  on the planetary boundary layer,  $\Gamma$  on the lapse rate, and N on the clouds. The parameter above the line (except  $A_{00}$ ) configure the parameter set  $P_{S5}$ .

	parameter [unit]	range in [unit]	$\mu$ [ $10^{-3}$ ]	infl. on
$p_{cs}$	integral transmission func. in clear-sky atm. [1]	0.72–0.86	12.23	$A_{cs}$
$B_{00}$	parameter of Budyko formula [ $W/m^2/K$ ]	1.6–2.3	11.37	$F_{\uparrow}$
$A_{00}$	parameter of Budyko formula [ $W/m^2$ ]	225–235	5.87	$F_{\uparrow}$
$C_k$	constant for determination of eddy diffusivities [1]	0.1–0.8	3.87	$h_{PBL}$
$\tau_{st}$	optical thickness of stratus clouds [1]	5–15	3.47	$A_{cl}$
$\Gamma_0$	lapse rate coefficient [ $K/m$ ]	$(5.4-6.6)\cdot 10^{-3}$	3.13	$\Gamma$
$p_{cl}$	integral transmission func. in cloudy atm. [1]	0.93–1	3.12	$A_{cl}$
$C_h^1$	constant for determination of $h_{PBL}$ for $w > 0$ [1]	2–6	2.89	$h_{PBL}$
$f_{oc}$	relative humidity at the ocean boundary [1]	0.7–0.86	2.74	$A_{cl}$
$T_{oc}$	temperature at the ocean boundaries [K]	298–303	2.70	
$b_{cl}$	albedo of the semi-infinite cloud at $\xi = 0$ [1]	0.038–0.057	2.65	$A_{cl}$
$L$	box length [m]	$(4-9)\cdot 10^6$	2.40	
$pCO_2$	volume concentration of $CO_2$ [ppm]	300–440	2.34	$F_{\uparrow}$
$z_0$	surface roughness length for vegetated soil [m]	0.01–0.8	2.22	
$k_{\tau}$	cloud albedo parameter [1]	0.59–0.72	2.15	$A_{cl}$
$F_{\downarrow}$	downward solar radiation [ $W/m^2$ ]	442–450	2.14	
$b_1$	cumulus cloudiness parameter [m/s]	$(0.5-2.5)\cdot 10^{-3}$	2.09	N
$a_q$	lapse rate coefficient [ $kg^2/kg^2$ ]	700–4000	1.99	$\Gamma$
$z_s$	surface layer height [m]	10–100	1.87	
$C_k^1$	const. for calc. of the kinematic viscosity	8–20	1.67	$h_{PBL}$
$\tau_0$	characteristic precipitation time [1]	$(2.5-6)\cdot 10^6$	1.53	
$N_{cu}^0$	reference cumulus cloud amount [1]	0.3–0.9	1.39	N
$\Gamma_1$	lapse rate coefficient [ $1/m$ ]	$(4.5-6.5)\cdot 10^{-5}$	1.16	$\Gamma$
$a_1$	stratus cloudiness parameter [1]	0.64–0.96	1.15	N
$L_m$	distance between upward and downward motion [m]	$(1-2)\cdot 10^6$	1.06	
$u_{mean}$	mean zonal wind velocity at the height of PBL [m/s]	1.5–3.5	1.05	
$H_e$	specific humidity scale height [m]	$(1.8-2.2)\cdot 10^3$	0.99	
$b_{cs}$	clear-sky albedo at $\xi = 0$ [1]	0.02–0.07	0.95	$A_{cs}$
$\tau_{cu}$	optical thickness of cumulus clouds [1]	10–30	0.94	$A_{cl}$
$H_t$	height of the troposphere [m]	$(12-15)\cdot 10^3$	0.83	
$C_{00}$	parameter of Budyko formula [ $W/m^2$ ]	57–61	0.78	$F_{\uparrow}$
$D_{00}$	parameter of Budyko formula [ $W/m^2/K$ ]	0.6–0.7	0.66	$F_{\uparrow}$
$K_r$	runoff parameter [1]	0.3–0.95	0.65	
$m_{cl}$	cloud albedo parameter [1]	0.64–0.96	0.63	$A_{cl}$
$\eta$	$CO_2$ sensitivity parameter [1]	0.03–0.05	0.5	$F_{\uparrow}$
$b_2$	cumulus cloudiness parameter [ $kg/kg$ ]	$(25-35)\cdot 10^{-3}$	0.42	$A_{cl}$
$\Gamma_2$	lapse rate coefficient [ $K/m$ ]	$(0.8-1.2)\cdot 10^{-3}$	0.37	$\Gamma$
$N_{oc}$	fraction of cloud cover over the ocean [1]	0.5–0.9	0.39	N
$a_2$	stratus cloudiness parameter [1]	0.07–0.15	0.26	$A_{cl}$
$a_3$	stratus cloudiness parameter [m/s]	$(0.8-1.2)\cdot 10^{-3}$	0.06	$A_{cl}$

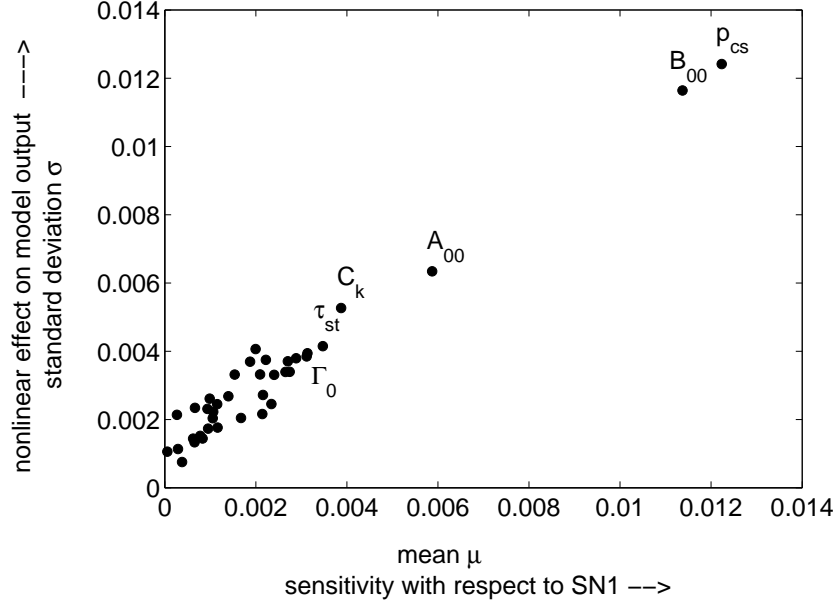


Figure 2.17: Results from the GSA with 41,000 runs with respect to the value of  $A_s$  at the bifurcation point.  $\mu$  is the mean distance between the bifurcation points for two different parameter settings,  $\sigma$  is the corresponding standard deviation, see explanation in the text. The six most influential parameters are marked.

Two statistical measures are derived for each parameter  $p_i$  from this analysis: the mean absolute value  $\mu_i = \text{mean}(|\Delta F_i|)$  and the standard deviation  $\sigma_i = \sigma(\Delta F_i)$  over all trajectories. A high mean value  $\mu_i$  is interpreted as an important overall influence of the parameter  $p_i$  on the model output (Saltelli et al. 2004). A high variance  $\sigma_i$  indicates that the parameter is involved in interactions with other parameters with respect to the model output or that the effect of the parameter on the model output is non-linear. The values for  $\mu_i$  can directly be interpreted in terms of the bifurcation point: on average the saddle node is shifted about  $\mu_i$  units when the parameter  $p_i$  is varied from one grid point to an adjacent one in the given range.

Here we randomly sample 1000 trajectories, resulting in 41,000 sample points and single model runs in total, where only 1,236 do not show a saddle node bifurcation and 1,478 runs cannot be included in the analysis as they show an abnormal termination. This means that in 93 % of the runs a saddle node bifurcation occurs, confirming again that the bifurcation point is a very robust feature of the model.

The ranking according to the value of  $\mu$  deduced from this analysis is listed in Table 2.1. This order obviously depends on the choice of the parameter ranges: altering the ranges of the parameters will probably change the ranking. However, by performing a second GSA with slightly different ranges for some of the parameters, we could confirm the ranking from Table 2.1 with only minor exceptions. As the choice of the uncertainty range is somewhat arbitrary, the absolute value of the mean distance  $\mu$  has to be considered in the interpretation as well, especially as we obtain a clustering concerning the parameter-related sensitivity of the bifurcation, where only a few are sensitive and most of the others



lie very near to each other (cf. Table 2.1 and Fig. 2.17). The GSA allows us to deduce two parameter subsets: The set of the five most influential parameters  $P_{S5}$  and the subset  $P_{A5}$  that includes the five most influential parameters that are subject to anthropogenic disturbances. These parameter sets will be further investigated in section 2.5.5 and 2.5.6.

Categorising the parameters by their effect on certain variables or processes, it attracts attention that the most influential parameters determine the albedo of the clear sky and the clouds, respectively, and therefore the planetary albedo (cf. the last column in Tab. 2.1), the outgoing longwave radiation  $F_{\uparrow}^{SL,TA}$  (cf. Eq. (2.12)), the height of the planetary boundary layer  $h_{PBL}$ , or the lapse rate  $\Gamma$  (cf. Eq. (2.20)). Most of these variables were shown to determine the bifurcation point, when analysing the normal form of the bifurcation (cf. Eq. (2.27)).

### 2.5.5 Deterministic parameter screening

We perform the deterministic parameter screening (cf. Fig. 2.15c) as an in-depth parameter uncertainty analysis to investigate how the model behaviour changes in dependence on specific parameters. To make sure that all model features are depicted but that the sample space is not too large to hamper the interpretation of results, the set of the five most influential parameters  $P_{S5}$  is chosen for the analysis.

From the GSA we have deduced the qualitative ranking of the parameters with respect to their influence on the location of the saddle node bifurcation. As we want to highlight here the qualitative aspects of particular processes, we omit the parameter  $A_{00}$  as it describes the same physical process as parameter  $B_{00}$  (outgoing longwave radiation, cf. Eq. (2.12)). The parameter set  $P_{S5}$  includes:

1. the integral transmission function of the clear-sky atmosphere  $p_{cs}$  that determines the albedo of the clear sky and thus the planetary albedo (cf. Eq. (2.7)),
2. the parameter  $B_{00}$  of the Budyko formula that determines the outgoing longwave radiation (cf. Eqs. (2.12) and (2.13)),
3. the constant for the determination of eddy diffusivities  $C_k$ , that influences the height of the planetary boundary layer  $h_{PBL}$ ,
4. the optical thickness of stratus clouds  $\tau_{st}$ , that controls the albedo of the clouds (cf. Eq. (2.10)), and
5. the parameter  $\Gamma_0$  of the lapse rate (cf. Eq. (2.20)), that determines the advection of heat.

Some of the processes the parameters describe were already mentioned in section 2.3.2 when introducing the normal form of the bifurcation as those controlling the bifurcation.

We separate each parameter range from  $P_{S5}$  into  $m = 4$  equidistant intervals. The resulting  $5^5$  grid represents the sample size with 3125 sample points, where all of the corresponding model runs show the saddle-node bifurcation. To visualise this 5-D parameter space we hold constant three parameters in each case. We calculate the maximum and

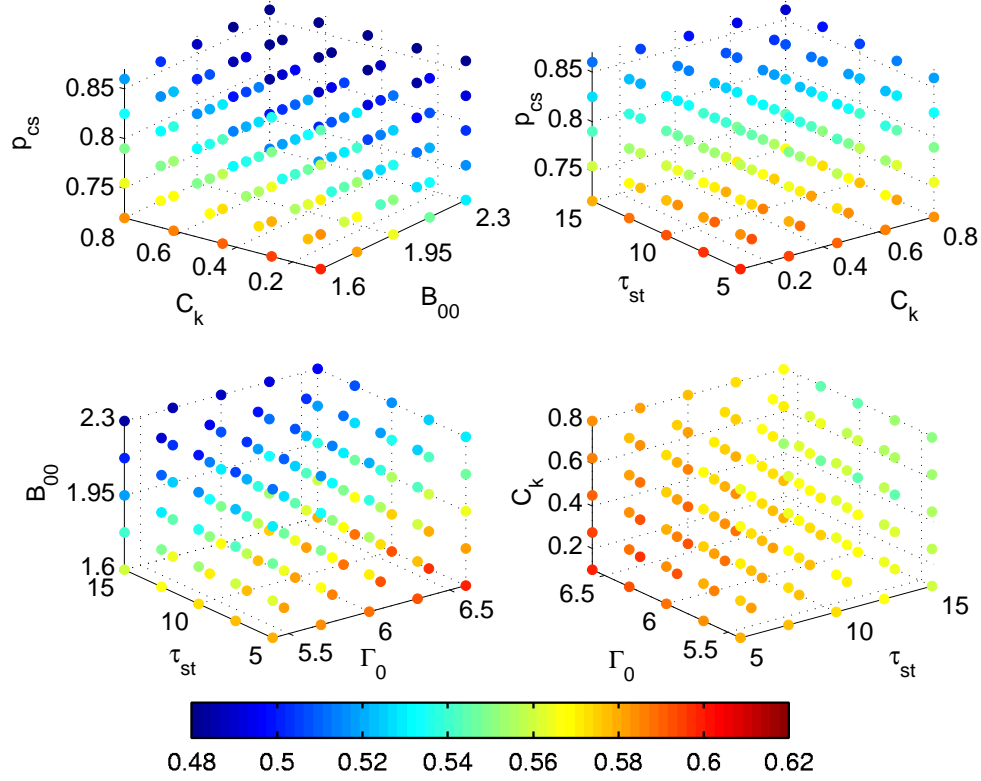


Figure 2.18: Maximum value for the surface albedo  $A_s$  at the saddle node bifurcation in dependence on the parameter set  $P_{S5} = (p_{cs}, B_{00}, C_k, \tau_{st}, \Gamma_0)$ . The colour represents the maximum value of the surface albedo  $A_s$  at the bifurcation point over those two dimensions that are not shown. The units for the parameters are for  $B_{00}$ : [W/K/m<sup>2</sup>],  $\Gamma_0$ : [ $10^{-3}$ K/m] and [1] for the others.

minimum, respectively over the 25 values – corresponding to the other two dimensions that are not shown – for the bifurcation parameter  $A_s$  at each point in the 3-D space. In total we obtain 10 3-D plots for the maximum and the minimum, respectively. We have chosen four in each case to illustrate the results (Figs. 2.18 and 2.19). Fig. 2.21 shows the difference between the maximum and the minimum, indicating an uncertainty range for the value at the bifurcation point with respect to the other two parameters that are not shown. From this analysis we can conclude, whether the change of the position of the saddle node bifurcation in dependence on one parameter  $p_i$  is linear (or non-linear) or whether an increase of  $p_i$  leads to an increase or decrease of the value for the surface albedo at the bifurcation point.

The direction from a low to a high value for  $A_s$  in each 3-D subspace is the same for the maximum and the minimum. For all 10 parameter combinations the variation in the values is continuous, there is no abrupt change or reversion of the direction of increasing values for  $A_s$ . The range for the surface albedo  $A_s$  in each 3-D subspace resembles the ranking from Table 2.1: the higher the rank of the involved parameters the broader is the range for the surface albedo  $A_s$ . Moreover, the cumulated Figs. 2.18 and 2.19 show that

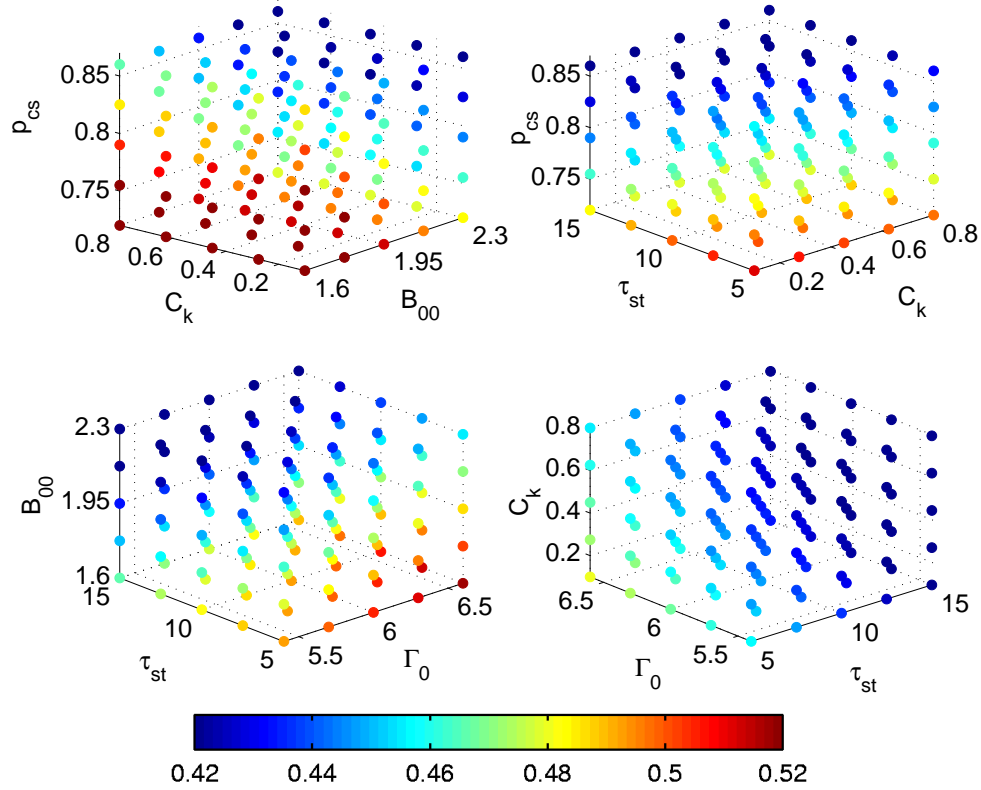


Figure 2.19: Same as Fig. 2.18 but for the minimum of the saddle-node bifurcation.

these five parameters alone cover a large range and particularly the part of the higher values for the albedo of the total uncertainty range evaluated by the MCA (cf. Fig. 2.20).

The directions of increasing values for  $A_s$  can be interpreted by analysing the involved processes that are represented by the parameters. In section 2.3.1 we have seen that the mechanism for the bifurcation strongly depends on the land-sea pressure and temperature gradient and therefore on the energy balance over India. All processes affecting this mechanism will certainly alter the position of the bifurcation point. The effect of the five most influential parameters can be related to this mechanism: A smaller albedo of the clear sky (represented by  $p_{cs}$ ) and hence a higher incoming solar radiation results in a higher amount of available energy and in more precipitation (cf. Fig. 2.3). Therefore a higher value for  $A_s$  is needed to get below the critical value where the monsoon circulation cannot be sustained any more. The heat balance equation explains the influence of the parameter  $B_{00}$  that directly influences the outgoing radiation: the lower  $B_{00}$ , the higher is the available amount of heat and therefore the value of  $A_s$  at the bifurcation.  $C_k$  determines the height of the planetary boundary layer  $h_{PBL}$  and the strength of the monsoon circulation  $u_{m,i}$ . As in the latter  $C_k$  enters with the inverse, a higher value for  $C_k$  results in a lower value for the maximum and minimum at the bifurcation point. The optical thickness of the stratus clouds  $\tau_{st}$  has a similar effect on the albedo as  $p_{cs}$ , so a lower value for  $\tau_{st}$  leads to higher values for the bifurcation point as well. The lapse rate coefficient  $\Gamma_0$  describes the vertical temperature profile (cf. Eq. (2.20)): the higher  $\Gamma_0$ , the lower is the temperature

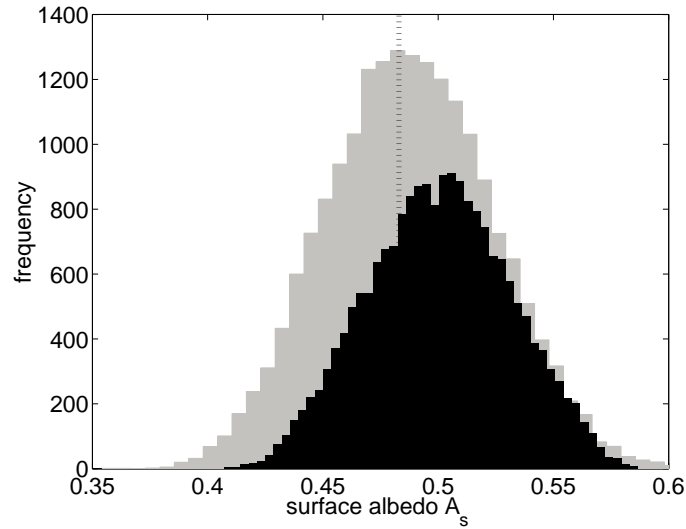


Figure 2.20: Results from the Monte Carlo analysis for the whole parameter set  $P_{40}$  (grey) and for the five most influential parameters  $P_{55}$  (black) both sampled with a Latin hypercube scheme. The figure displays the frequency of the value of the surface albedo  $A_s$  at the bifurcation point. The vertical dotted line at  $A_s = 0.483$  marks the default value of  $A_s$ , cf. Fig. 2.10.

at a specific height  $z$  and the lower is the advection of heat by the upper tropospheric circulation from land to the ocean. This implies that more energy is available shifting the bifurcation point further to higher values of the albedo.

Fig. 2.21 – and the study of the other six 3-D diagrams – indicates that when the parameters  $p_{cs}$  and  $B_{00}$  are known, the overall uncertainty concerning all three other parameters is just  $\approx 0.045$  (cf. Fig. 2.21a), that is less than 10% of the mean value of  $A_s = 0.484$ . But soon as one of the parameters  $p_{cs}$  or  $B_{00}$  is unknown the uncertainty grows to  $\approx 0.09$  (cf. Fig. 2.21b,c). The uncertainty about the range for the bifurcation point that is related to these two most influential parameters reaches  $\approx 0.14$  (cf. Fig. 2.21d), indicating a large uncertainty range. Again it has to be stated that the quantitative uncertainty range depends on the chosen uncertainty ranges for the parameters, although the qualitative conclusions remain the same.

### 2.5.6 Deterministic parameter screening of anthropogenically influenced parameters

We will now analyse the parameter set  $P_{A5}$  of the five most influential parameters as derived from the GSA that are subject to anthropogenic perturbations. This investigation will account for the uncertainty in future projections that could change the monsoon characteristics from a wet to a dry regime. Anthropogenic activities can alter the  $\text{CO}_2$  concentration by the emission of greenhouse gases, which in turn has an effect on the global mean temperature and therefore on the temperature at the ocean boundaries  $T_{oc}$ . The ongoing emission of sulphate aerosols has a “direct” and an “indirect” radiation effect. By

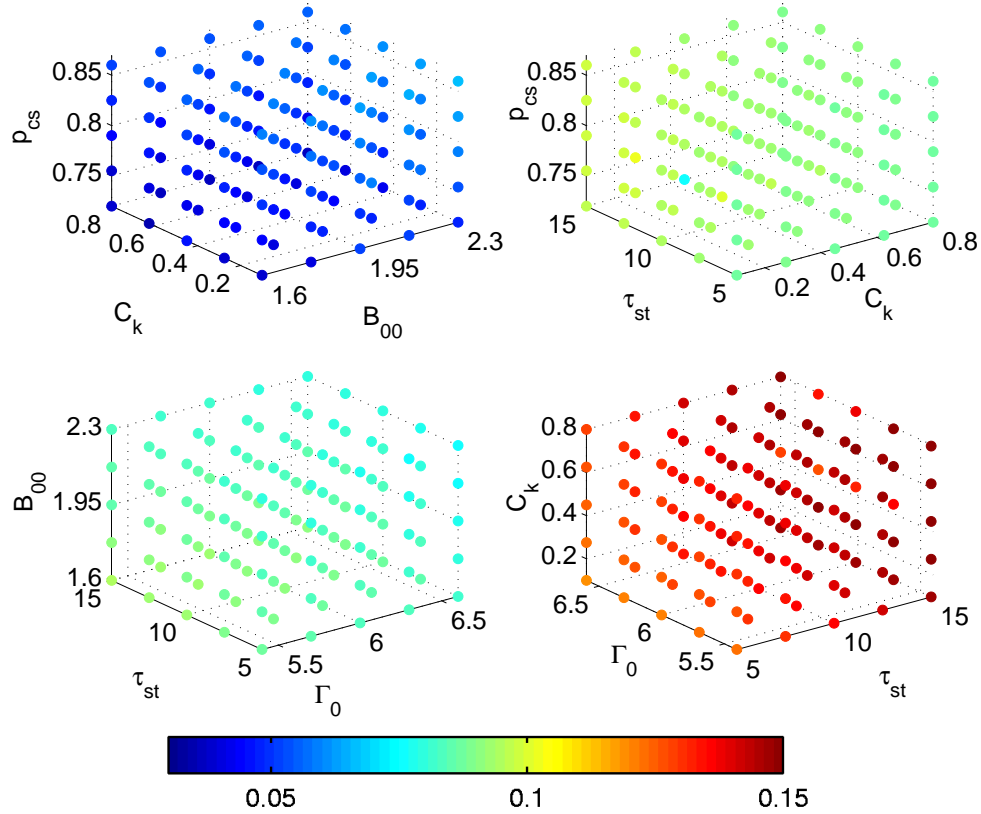


Figure 2.21: Same as Fig. 2.18 but for the uncertainty range (i.e. maximum-minimum) of the saddle-node bifurcation. The distribution is nearly uniform over the parameters. The colour corresponds to the uncertainty that is related to the other two dimensions of  $P_{S5}$  that are not shown in each 3-D diagram. Note that the given value is *not* the uncertainty range of the parameters shown but the resulting range over the other two parameters that are not shown.

the direct effect the scattering aerosols increase the albedo of the clear sky  $b_{cs}$ . The first indirect effect refers to the fact that the aerosols lead to an increase in droplet concentration that alters the optical thickness of the stratus clouds  $\tau_{st}$ . The second indirect refers to the influence of the aerosols on the lifetime of clouds. Land use or land cover change can alter the surface roughness  $z_0$  of India, for instance by decreasing the roughness due to forest conversion. To account for these changes we choose the five most influential parameters each representing one of the above mechanisms, while we include only one of the indirect effects (cf. Table 2.2).

The MCA of the parameter set  $P_{A5}$  with 20,000 runs implementing a Latin hypercube scheme with an equally distributed likelihood over the parameter ranges leads to a distribution of the values for  $A_s$  at the saddle node bifurcation that is shifted to lower values (cf. Fig. 2.22) in comparison to the analysis of the full parameter set  $P_{40}$  in Fig. 2.16 and particularly in relation to the parameter set  $P_{S5}$ .

From Figs. 2.23 and 2.24 it can be seen that the anthropogenic influence on the two parameters  $z_0$  and  $pCO_2$  shifts the bifurcation point further away from today's values. In

Table 2.2: Set of the anthropogenically influenced parameters  $P_{A5}$  of the monsoon model that are chosen for the deterministic parameter screening. Note that the ranges are the same as in Table 2.1. In the last column, an upward pointing arrow ( $\uparrow$ ) denotes an increasing anthropogenic effect on the parameters and a downward pointing arrow ( $\downarrow$ ) a decreasing effect.

	parameter [unit]	range in [unit]	reference value	anthro. infl.
$\tau_{st}$	optical thickness of stratus clouds [1]	5–15	7.5	$\uparrow$
$pCO_2$	volume concentration of CO <sub>2</sub> [ppm]	300–440	360	$\uparrow$
$T_{oc}$	temperature at the ocean boundaries [K]	298–303	300	$\uparrow$
$z_0$	surface roughness length for vegetated soil [m]	0.01–0.8	0.1	$\downarrow$
$b_{cs}$	clear-sky albedo at $\xi = 0$ [1]	0.02–0.07	0.05	$\uparrow$

case of the CO<sub>2</sub> concentration we have discussed this relation earlier, in case of the surface roughness  $z_0$  it can be shown that a lower value for  $z_0$  – caused e.g. by forest conversion – decreases the monsoon circulation  $u_{m,i}$  resulting in higher values for the temperature over India. This sustains a high amount of available heat and shifts the bifurcation point to higher values for the surface albedo.

On the other hand, the increasing values of  $\tau_{st}$ ,  $b_{cs}$ , and  $T_{oc}$  due to human activity lead to a decrease of the value for  $A_s$  at the bifurcation point. The stabilising effect of increasing the parameters  $\tau_{st}$  and  $b_{cs}$ , which influence the albedo of the clouds and the clear sky, has been discussed in the previous section and leads to a lower value for  $A_s$  at the bifurcation point. The influence of the ocean temperature  $T_{oc}$  is not continuously increasing or decreasing but shows a turning point at  $T_{oc,TP} \approx 300$  K (cf. Fig. 2.25) that can, however, hardly be seen in Figs. 2.23 and 2.24. This turning point is due to some symmetry effect of the temperature  $T_a$  around  $T_{oc} = 300$  K, as most parameterisations change sign with the sign of the temperature difference ( $T_a - T_{oc}$ ).

From Figs. 2.23 and 2.24 it can be deduced that it strongly depends on the exact value the five parameters will take in the future to decide if anthropogenic action will shift the bifurcation point nearer to today’s values.

## 2.6 Conclusions

We have analysed a reduced form model of the Indian summer monsoon that exhibits a saddle node bifurcation in dependence on those parameters that influence the heat budget of the system. This transition goes along with a change from a wet to a dry monsoon regime and a bistable regime can be detected as well. As bifurcation parameters we investigated the planetary and the surface albedo, the CO<sub>2</sub> concentration and the insolation. The latter two were shown to possibly have triggered an abrupt transition from a wet to a dry monsoon regime (and vice versa) in paleo times and provide an explanation of the abrupt climate changes over India that are reported from paleo data.

The albedo parameters can become important for a potential future change of the mon-

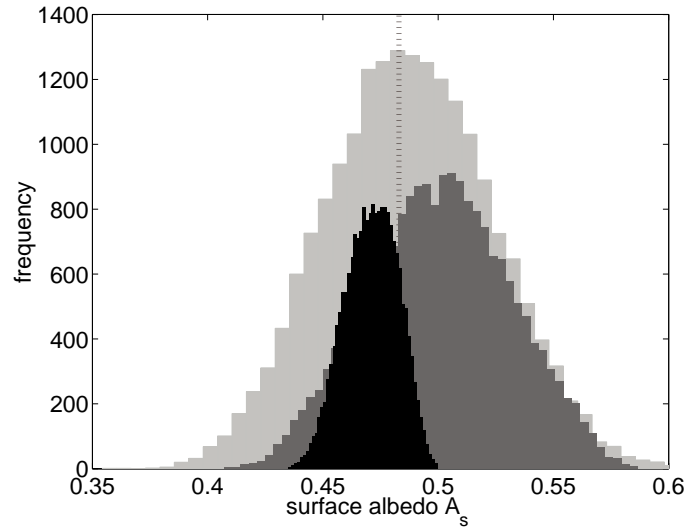


Figure 2.22: Results from the Monte Carlo analysis for the whole parameter set  $P_{40}$  (light grey), for the five most influential parameters  $P_{S5}$  (dark grey), and the five anthropogenically influenced parameters  $P_{A5}$  (black) all sampled with a Latin hypercube scheme. The figure displays the frequency of the value of the surface albedo  $A_s$  at the bifurcation point. The mean value for  $P_{A5}$  is  $A_s = 0.474$ , the median lies at  $A_s = 0.465$  and the standard deviation is  $\sigma = 0.012$ . The vertical dotted line at  $A_s = 0.483$  marks the default value of  $A_s$ , cf. Fig. 2.10.

soon regime, as anthropogenic disturbances can alter the albedo, e.g. by aerosol emissions or forest conversion. As such a regime transitions could have dramatic effects on India's population the main focus of this chapter was to estimate the robustness of the bifurcation point and whether this point could be reached by anthropogenic perturbations. We came up with an appraisal of the model's structure and parameter uncertainty concerning the occurrence of the bifurcation point.

Our results show that the occurrence of the bifurcation point is robust over a wide range of parameter values. The position of the bifurcation in phase space, however, is found to be sensitive on these specific parameter choices. On the other hand, the existence of the bifurcation point is not structurally stable against all considered mechanisms. Nonetheless, the dramatic decrease of precipitation with an increase of the albedo is maintained.

A new method was developed and applied for investigating the robustness of a bifurcation point against parameter uncertainties in the model of the Indian summer monsoon. This approach builds on combining a bifurcation analysis with a common sensitivity and uncertainty analysis in the high dimensional parameter space. The methods that are implemented for global sensitivity and uncertainty studies are based on a large number of model runs with varying parameter settings and are provided by an ensemble simulation tool. Such an in-depth parameter uncertainty analysis of a bifurcation point is a novel approach and a universal method that can be applied to other models of similar complexity where the robustness of a bifurcation point against parameter uncertainties is of interest.

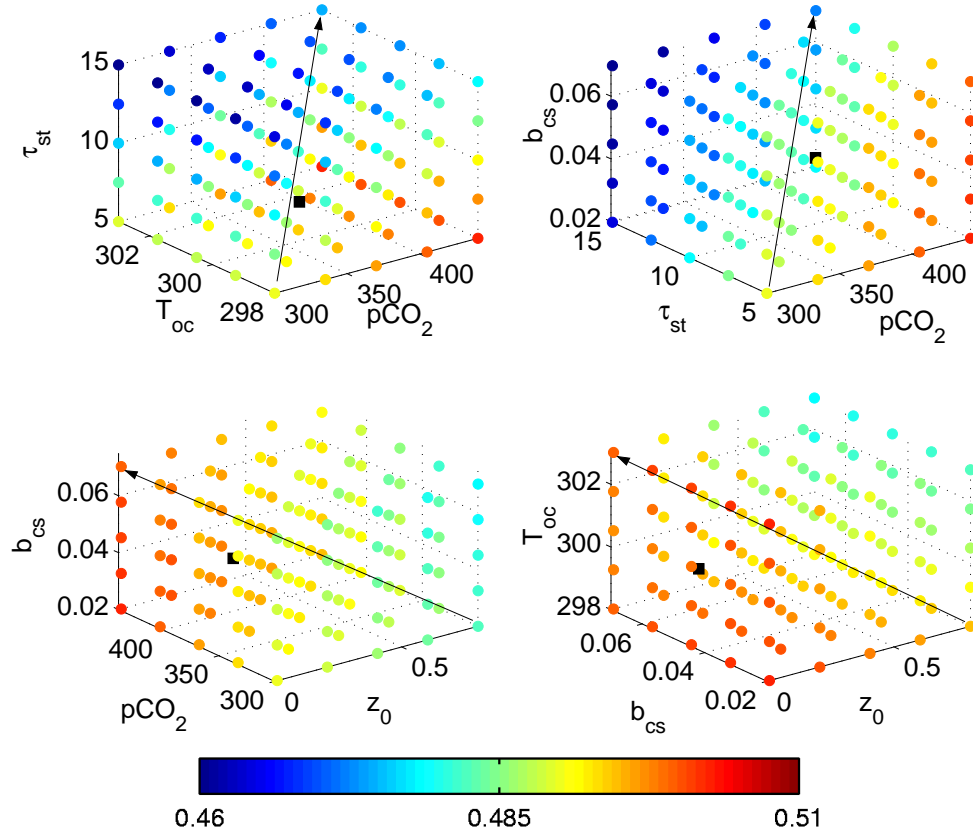


Figure 2.23: Maximum value for the surface albedo  $A_s$  at the saddle node bifurcation in dependence on the parameter set  $P_{A5} = (\tau_{st}, pCO_2, T_{oc}, z_0, b_{cs})$  for four exemplary subspaces. The colour represents the maximum value of the surface albedo  $A_s$  at the bifurcation point over the other two parameters that are not shown. The black square denotes the present day state, the arrows indicate the direction of a “business as usual path” of anthropogenic perturbations. The units for the parameters are given in Tab. 2.2.

The global sensitivity analysis, based on the multi-run method, let us conclude that the parameters differ largely concerning their influence on the location of the bifurcation point. The most influential parameters are related to the planetary albedo, the heat budget through the incoming and outgoing solar radiation, or the lapse rate. The overall multi-parameter uncertainty analysis has impressively shown that the occurrence of the saddle node bifurcation in this model is a very robust feature. In over 96% of all runs for the Monte Carlo analysis and in 93% of all runs for the global sensitivity analysis the model shows the abrupt transition from a wet to a dry monsoon regime. The propagation of the parameter uncertainties, however, leads to a very broad range for the surface albedo  $A_s$  at the bifurcation point indicating a high uncertainty about the actual position of the bifurcation in phase space. Moreover, the influence of anthropogenically affected parameters have opposite effects on the position of the bifurcation point relative to present day. Consequently, a robust estimate concerning the influence of human activity requires model experiments with plausible scenarios of future changes. The interpretation is twofold: on



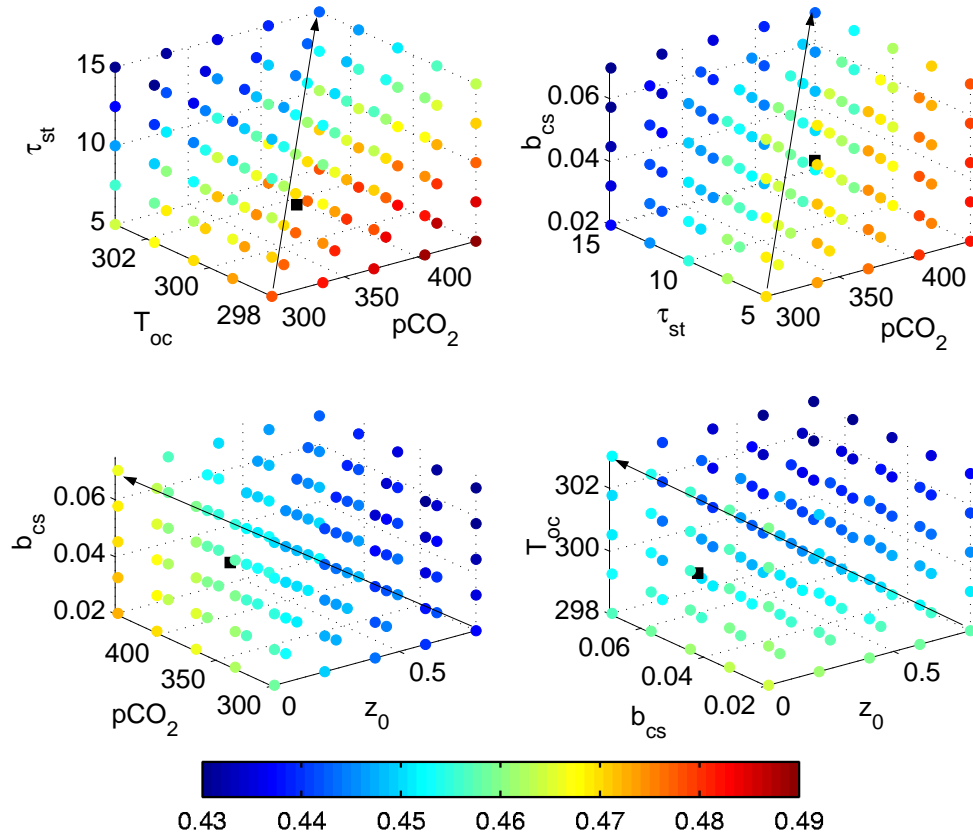


Figure 2.24: Same as Fig. 2.23 but for the minimum values.

the one hand – under the assumption that the model is reliable – the uncertainty analysis shows that the bifurcation point is far away from today’s values and that we can be very certain that we will not reach this point in the near future. On the other hand – under the assumption that the model is just a conceptual one and will not be able to give an estimate of the true value of the surface albedo at the bifurcation point – this analysis shows that we have to deal with a wide uncertainty range, which is in the order of the entire range for all possible values of the surface albedo. Under these uncertainties it is hardly possible to assess the distance between today’s value and the bifurcation point. The proximity of the system to such a threshold could probably be estimated by means of an analysis that builds on a shift in the spectrum of observational data when coming nearer to the bifurcation point (Held and Kleinen 2004).

For the structural model uncertainty analysis we investigated a hierarchy of models where we successively increased the number of processes in each version, starting from the basic formulation introduced in Zickfeld et al. (2005). Some of the included mechanisms lead to the possibility that the bifurcation vanishes: The negative vegetation feedback stabilises the system and lets the bifurcation disappear. The same holds for the influence of the Tibetan Plateau. On the other hand, the large scale circulations, i.e. the Hadley and the trade wind circulation, shift the bifurcation point to higher values of the surface albedo and decrease the steepness of the regime transition, but still maintain the saddle

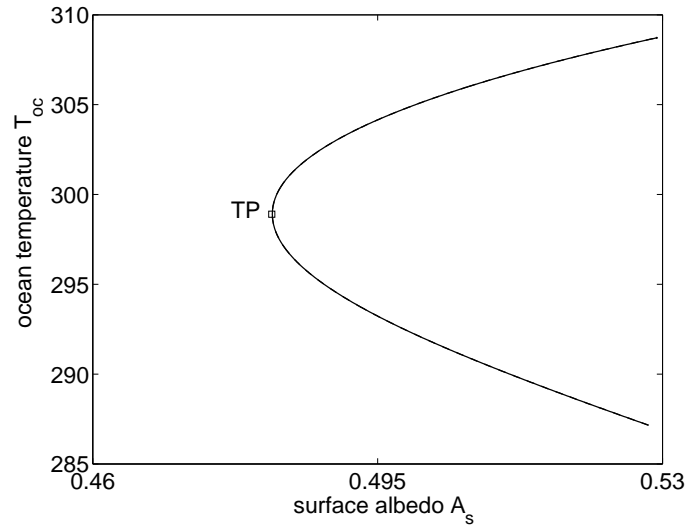


Figure 2.25: Path following of the saddle node bifurcation SN1 in two parameter directions. TP marks the turning point.

node bifurcation. The shift of the bifurcation point to higher albedo values goes along with a decline of the bistable regime, so the bistability seems to be an important feature only in the basic model and is not found in the more elaborated versions.

The fact that the bifurcation is robust under parameter uncertainties and that despite the implementation of all parameterisations we observe a dramatic decline of the precipitation in a certain range of the bifurcation parameter supports earlier findings (Zickfeld et al. 2005). The large uncertainty that we find in this conceptual model requires further investigations with a more complex model, such as a high resolution GCM, to come up with more robust estimates about the actual point of this possible transition.

A further important conclusion of this chapter is the fact that the parameter uncertainty analysis leads to a robust result concerning the occurrence of the bifurcation point, whereas the structural uncertainty analysis does not. As most uncertainty studies in GCMs are restricted to the investigation of parameter uncertainty, this finding emphasises the strong need for the consideration of a structural uncertainty analysis to come up with robust results concerning the overall model uncertainty.

## Chapter 3

# On the physical link between the Indian monsoon and ENSO: past and future

### 3.1 Introduction

In the previous chapter we have seen that the Indian summer monsoon depends on several mechanisms that determine the strength of the monsoon precipitation. Besides the uncertainties in parameters and parameterisations, which we investigated by means of a model of the Indian summer monsoon, uncertainties about other processes and external influences that affect the Indian monsoon are of major importance when analysing future changes in precipitation over India. This issue will be addressed in this chapter and is related to the uncertainty of external forcing as characterised in Eq. (1.2).

The intensity of the Indian summer monsoon rainfall (ISMR) shows a strong intraseasonal, interannual, and interdecadal variability. The monsoon onset on the one hand and the active and break phases of the monsoon rainfall on the other hand are the most crucial phenomena on the intraseasonal scale. The latter two are associated with the position of the Inner Tropical Convergence Zone (ITCZ) (Webster et al. 1998). Palmer (1993) showed that this behaviour can be explained by a chaotic Lorenz type model. The interannual variability has two pronounced modes (Terry 1995). One is the Quasi-biennial Oscillation (QBO), an equatorial stratospheric wind oscillation, at a timescale of about 2-3 years. The other mode on a timescale of 3-7 years is associated with the El Niño / Southern Oscillation (ENSO) phenomenon. The interdecadal variations of the monsoon system are mainly influenced by anomalies in the Hadley circulation (Krishnamurthy and Goswami 2000; Chang et al. 2000).

As mentioned earlier, the monsoon cannot be seen as an isolated feature but is also dependent on changes of other large-scale phenomena. Goswami et al. (2006) reveal a link of the Atlantic Multidecadal Oscillation to the variability of the Indian summer monsoon. The role of the circulation over the North Atlantic was also pronounced by Chang et al. (2001) and Kripalani et al. (1997). Here we will focus on the teleconnection

mechanism between ENSO and the ISMR that is a main driver of monsoon variability on the interannual (3-7 years) timescales (Webster et al. 1998).

The correlation of an El Niño event and weaker monsoon rainfalls was first discovered by Sir Gilbert Walker (Walker 1923). The strong link between the strength of Indian monsoon rainfall and ENSO has been reported from data (Webster and Yang 1992; Kripalani and Kulkarni 1997) as well as from simulations with global climate models (Ju and Slingo 1995; Kitoh et al. 1999; Latif et al. 2001). For the summer months June to September the correlation  $r$  between ENSO indices and the Indian monsoon rainfall attains  $r = -0.63$  for the period from 1871-1990 and the ENSO signal is able to explain about 40% of the variance of the Indian summer monsoon. This implies that the identification of the physical processes responsible for the influence of ENSO on the monsoon is of great importance for predicting the ISMR in order to allow adaptation to impacts of anomalous weak or strong monsoons. Nevertheless the physical link between the two phenomena is still not fully understood and is discussed intensively in the literature (Webster and Yang 1992; Webster et al. 1998; Goswami 1998; Fasullo and Webster 2002). We will contribute to the debate by systematically analysing different physical mechanisms.

Several studies show that the sea surface temperature (SST) in diverse regions of the Pacific and Indian Ocean can influence the monsoon: Li et al. (2001) e.g. state that changes of the Indian Ocean SSTs influence the monsoon on the tropical biennial oscillation time scale (2-3 years). With a model ensemble study Kucharski et al. (2006) suggest that the local Indian Ocean SSTs have a significant influence on the ISMR variability, whereas the eastern Pacific SST anomalies play a less important role. They also emphasise the influence of the SSTs on the local Hadley circulation that in turn modifies the ISMR. Goswami et al. (2006) show a teleconnection mechanism between SSTs in a region as far as the North Atlantic and the Indian summer monsoon by means of a data analysis.

Other studies reveal that the snow depth over the Tibetan Plateau is an important connection between monsoon and ENSO. Blandford (1884) was the first who hypothesised an influence of ENSO on snow depth of the Tibetan Plateau. This would in turn have an influence on monsoon rainfall, as the main driver for precipitation is the land-sea temperature contrast that would be altered by decreasing temperatures over the Tibetan Plateau due to increasing snow depth. The effect of ENSO on snow cover and snow depth over the Tibetan Plateau is discussed controversially in the literature. Shaman and Tziperman (2005) propose that El Niño conditions increase the snow pack over Eurasia; Meehl (1997) states the inverse. Moreover the effect of snow on the Indian monsoon is still a point of ongoing research. Many studies find an inverse relationship of snow pack over Eurasia and subsequent ISMR (Hahn and Shukla 1976) but some also find a significant dependence on the region under investigation: Dash et al. (2005) e.g. discover from data analysis a positive relation of snow cover and ISMR for East Eurasia and a negative for West Eurasia. Bamzai and Shukla (1999) show that the snow cover over the Tibetan Plateau could have an impact on the strength of the Indian monsoon.

The large scale circulations, such as Hadley and Walker circulation also seem to play a major role for the monsoon variability and the mechanism between monsoon and ENSO (Krishnamurthy and Goswami 2000). Webster and Yang (1992) were the first to report

that a strong (weak) monsoon is associated with enhanced (weakened) summer trade winds over the Indian subcontinent that are in turn influenced by ENSO. They propose that the anomalies of the zonal wind shear between the 200 hPa and the 850 hPa level, or even the 200 hPa wind anomalies alone, could serve as a monsoon intensity index. This finding suggests a strong link between ENSO as a coupled ocean-atmosphere system and the Indian summer monsoon.

The interdecadal changes (Torrence and Webster 1999) and the possibly changing relationship of ENSO and the Indian monsoon, that is observed since the 1980s, are a subject of ongoing research. Kumar et al. (1999) propose a weakening relationship between ENSO and the Indian summer monsoon that could either be due to a shift in the Walker circulation or to increased surface temperatures over Eurasia. This weakening may also be attributed to increasing influence of global-scale factors other than ENSO on the Indian monsoon, e.g. increasing greenhouse gas concentrations and/or aerosol loading of the atmosphere (Meehl and Washington 1993; Lal et al. 1995). Other studies suggest that the influence of ENSO on the Indian monsoon has not decreased but that other effects like the local circulation pattern have changed and interfere with each other (Sarkar et al. 2004) or that the weakening relationship could be due to circulation changes in the North Atlantic (Chang et al. 2001). A model study with the coupled general circulation model (GCM) ECHAM4/OPYC (Roeckner et al. 1996) driven with different greenhouse gas scenarios suggest that the intensity of the Indian summer monsoon as well as the interannual variability will be enhanced (Wei 2005). A similar study with this model additionally projects a change of the SSTs in the eastern Pacific towards an El Niño like mean state and a higher variability of ENSO (Ashrit et al. 2001). Nonetheless, after removing the trend in both time series, the ENSO-Indian monsoon inverse relationship is still present in the future in this model. On the other hand, according to the aforementioned study, the influence of El Niño (in contrast to La Niña) events will be decreased under higher greenhouse gas concentrations. Meehl and Arblaster (2003) found an enhanced monsoon precipitation variability in the PCM model (Washington et al. 2000) that will be mainly due to a remote effect of SST warming in the Pacific Ocean.

The weakening relationship between ENSO and monsoon could also originate from a different cause: Webster and Palmer (1997) related the change in the ENSO-Monsoon relationship to the chaotic nature of the Indian monsoon with its irregular alternation between rainy and drought regimes. Similarly reads the hypothesis from Gershunov et al. (2001): the decadal modulation of the correlation between the two phenomena could also be traced back to the effect of coupling two stochastic processes.

Considering the fact that the link between ENSO and the Indian monsoon is still a point of ongoing discussion, the purpose of this study is to understand the physical mechanism linking ENSO and the Indian monsoon for the past and to investigate its future under enhanced greenhouse gas concentrations. For this study, we use the full version of the box model of the Indian monsoon, which was described in chapter 2, section 2.2 and has proven to well reproduce relevant variables, e.g. precipitation averaged over India (cf. Fig. 2.2 and Zickfeld (2004)). Because of its transparency this reduced form model is highly suitable for understanding the interplay between different physical processes and allows separating

different effect to gain a basic understanding of the link between ENSO and the ISMR.

The uncertainty that will be investigated here is – in contrast to the analysis in chapter 2 – not related to a stable equilibrium state of the monsoon but to the transient dynamics that is governed by an external forcing related to ENSO. This analysis refers to the investigation of the uncertainty that is related to external forcings and their linking to the model as captured in Eq. (1.3). The guiding questions are:

- What is the physical mechanism linking the Indian monsoon and ENSO?
- How will this mechanism behave under global warming?

The chapter is organised as follows: The method for testing and comparing the aforementioned three hypotheses is presented in section 3.2. With the identified mechanism we are able to reconstruct the part of the ISMR time series that is determined by ENSO. The future of the ENSO-monsoon relationship is analysed in section 3.2.4 considering scenario runs from two GCMs. The final section 3.3 gives a summary and an outlook.

## 3.2 The physical link between the Indian monsoon and ENSO

As pointed out in the introduction, several hypotheses, based on data analysis and results from GCMs, exist on how ENSO could affect the intensity of the Indian monsoon. Here we will test three possible hypotheses of the influence of ENSO on the ISMR. The following hypotheses are taken into account: the influence of ENSO on the ISMR through

- (i) the sea surface temperatures (SSTs) in the Indian Ocean
- (ii) the snow cover over the Tibetan Plateau and
- (iii) the strength of the zonal trade winds.

With the box model we will implement the aforementioned hypotheses (i)-(iii) with the goal to reproduce the observed time series of the ISMR, which enables us to identify the physical link. We test the three hypotheses by comparing the historical data from 1871-1990 of the ISMR with the simulated model results, where we implement the full version of the monsoon model (M4) as introduced in section 2.2 and section 2.4.3. The only extension concerns the Hadley circulation that is modelled in dependence on the temperature difference between the Tibetan Plateau and the equatorial Indian Ocean that we derived from observational data:

$$v_H = -0.25(T_S - T_{tib}) + 3.3. \quad (3.1)$$

We analyse the deviations from the long-term mean for the summer monsoon rainfall in the period from June to September (JJAS) as this is the most important monsoon characteristic.

The monsoon data we use are monthly mean values from 1871-1990 for the All Indian Rainfall (AIR) (Parthasarathy et al. 1995). For representing ENSO we employ SST

anomalies in the eastern equatorial Pacific from the extended Kaplan NINO3 index (Kaplan et al. 1998), that will be denoted as  $T_{\text{ENSO}}$  in the following. The data that is used for analysing relationships between temperatures or zonal winds and ENSO are taken from the NCEP/NCAR reanalysis (Kalnay et al. 1996) that are available from 1948 on. In our analysis we neglect the latest 15 years because of the proposed weakening ENSO-Indian monsoon relationship (Kumar et al. 1999), which is evident in the data. To analyse how the mechanism will evolve under anthropogenic climate change we use the results obtained with the ECHAM5/MPI-OM model (Jungclaus et al. 2006) forced with the SRES scenario A2 (Nakićenović et al. 2000) and for the control run with the model fixed to preindustrial conditions. Monthly mean values are available for the SRES A2 scenario for the years 2000-2100 and for the control run at the CERA database (CERA 2006). Additionally we analyse similar runs from the HadCM3 model (Gordon et al. 2000).

As the influence of ENSO on the monsoon is much stronger than the other way round we neglect the effect of the Indian monsoon on ENSO that was reported in other studies (Kirtman and Shukla 2000; Wu and Kirtman 2003, e.g.). The assumption of a unidirectional coupling is supported e.g. by studies of Wang and Fang (1996) and Tziperman et al. (1998) who show that the main source of ENSO variability is the atmosphere-ocean dynamics in the Pacific Ocean.

The procedure for identifying the physical mechanism is as follows: from observations we derive the coupling coefficient between ENSO and the specific variable (e.g. the SST in the Indian Ocean) that is hypothesised to communicate the influence of ENSO on the monsoon. We then force the monsoon model with the NINO3 data as an external driver via the suggested mechanism with the deduced coupling coefficient. For estimating the performance of the proposed mechanism, we require the following conditions of simulated and observed values for the ISMR to be fulfilled simultaneously: (a) a high correlation coefficient, (b) the ability of the mechanism to explain large parts of the observed ISMR variance (a high explained variance), (c) the ability to reproduce the observed relationship of weaker (stronger) monsoons during El Niño (La Niña) events, and (d) a similar standard deviation.

Although our model is strongly nonlinear in the prognostic variables  $T_a, q_a, w_1$  and  $w_2$  and also in the boundary conditions such as  $T_S, T_W, T_E$  and  $T_{tib}$ , we find the response of the model to changing boundary conditions to be more or less linear. This is probably due to the parameter setting that does not allow the non-linearities to unfold. Therefore, with the procedure described above for reproducing the ISMR we expect to get a response, which resembles a scaled ENSO signal. Nonetheless, this does not make the use of the box model obsolete. In fact, the latter is needed to derive the qualitative nature of the response (e.g. is it correlated or anti-correlated?). Also, our approach allows us to isolate a single mechanism and investigate its response what is often not possible in a complex GCM. As our model, however, is simple we will focus more on the qualitative criteria (a) and (c) although we are convinced that we can also draw some quantitative estimates from this investigation.

### 3.2.1 Influence of ENSO on the ISMR through the SSTs in the Indian Ocean

The first mechanism to be tested is the influence of ENSO on the ISMR via the SSTs in the Indian Ocean. In our model the SSTs are boundary conditions and affect the temperature gradient between land and sea that acts as the main driver for the monsoon circulation and determines the advection of heat and moisture (cf. Eq. 2.14). From the NCEP/NCAR data we find a positive relationship between the Indian Ocean temperature anomalies and the SST anomalies  $T_{\text{ENSO}}$  in the eastern Pacific:

$$\Delta T_{oc} = \alpha T_{\text{ENSO}}. \quad (3.2)$$

Here  $\Delta T_{oc}$  describes the SST anomalies at the ocean boundaries and  $\alpha = 0.24$  is the coupling parameter, derived from the data with least squares fitting (with a correlation coefficient of 0.38 corresponding to a 99% significance level). Adding this temperature anomaly to the seasonal cycle of the respective boundary in our model, we find that none of the conditions (a)-(d) is fulfilled (Fig. 3.1a). The implemented relationship (3.2) leads to an inverse behaviour of the simulated and observed rainfall anomalies ( $r = -0.21$ ), with El Niño years causing rainfall above normal in the model. Moreover, the simulated variance of 12 mm is far too low compared to the observed one of 84 mm.

The physical mechanism is as follows: during an El Niño event, higher temperatures over the Indian Ocean lead to a decrease in summer advection – regulated in the model by the land-sea temperature gradient – of the relatively warm (cold) air from (to) the Indian subcontinent, and the temperature over India rises. This, in turn, enhances the amount of water vapour, which is transported from the warmer oceans and uplifted. In total all these processes result in an increase in precipitation.

If we neglect the dependence of the Hadley circulation on the temperature in the equatorial Indian Ocean (cf. Eq. (3.1)) and just prescribe it with a seasonal cycle, the resulting signal is still anti-correlated but with an even smaller standard deviation. This yields an influence of the Hadley circulation that is qualitatively consistent with the data. This finding suggests that the significant influence of Indian Ocean SSTs on ISMR variability that is found in some studies (Kucharski et al. 2006, e.g.) occurs mainly through the large scale circulation rather than the local monsoon circulation. Moreover, our result supports the conclusions from a GCM study by Wu and Kirtman (2004) who emphasise the importance of the coupled air-sea interaction in the Indian Ocean for the ENSO-Indian monsoon inverse relationship. Nonetheless, from the qualitative discrepancy that we found in Fig. 3.1a we conclude that the air-sea interaction changes due to ENSO described by mechanism (i) cannot explain the observed relationship, but goes into the opposite direction.

### 3.2.2 Influence of ENSO on the ISMR through the snow depth over Tibet

Hypothesis (ii) proposes an impact of ENSO on the snow cover over Eurasia. In turn, this affects the land surface processes and influences the Indian monsoon. As in our model the snow pack over the Tibetan Plateau is not computed explicitly we use the temperature



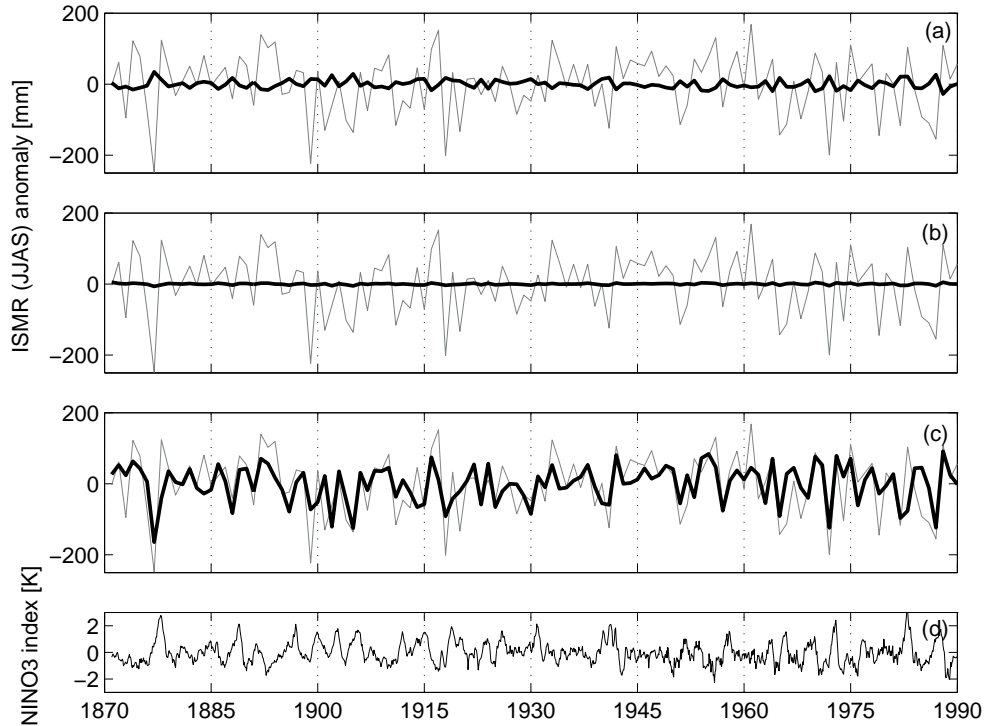


Figure 3.1: Comparison of simulated (thick black) and observed (thin grey) Indian summer monsoon rainfall anomalies for the season June-September (JJAS) for different couplings: (a) influence of ENSO on the temperatures in the Indian Ocean according to Eq. (3.2) with a correlation  $r = -0.21$ , (b) influence of ENSO on temperature over the Tibetan Plateau according to Eq. (3.3) with  $r = 0.52$ , (c) influence of ENSO on the zonal trade winds according to Eq. (3.4) with  $r = 0.64$ , (d) monthly mean values for the NINO3 index used to force the model.

over the Tibetan Plateau  $T_{tib}$  as a proxy for this quantity, similar to the approach taken by Kumar et al. (1999). For physical reasons, we assume a negative relationship between snow depth and the temperature  $T_{tib}$ : because of the higher albedo of snow less solar radiation can heat the land and more solar energy is consumed to melt the snow. In return, this increases the wetness of the surface and the relative humidity over Tibet. As our model shows a positive relationship between the temperature  $T_{tib}$  and the ISMR we expect a negative relationship between snow depth and ISMR.

From the data we analyse the correlation between the NINO3 index and temperature anomalies over Tibet, averaged over  $30^{\circ}\text{N}$ - $40^{\circ}\text{N}$  and  $70^{\circ}\text{E}$ - $100^{\circ}\text{E}$ . We find a negative correlation above the 95% significance level for the summer months June-September. The effect of ENSO on the temperature anomalies over Tibet  $\Delta T_{tib}$  by means of the snow depth is therefore modelled by a least squares linear fit as

$$\Delta T_{tib} = -\beta T_{\text{ENSO}}. \quad (3.3)$$

with  $\beta = 0.27$  for JJAS. This negative correlation implies a positive influence of ENSO

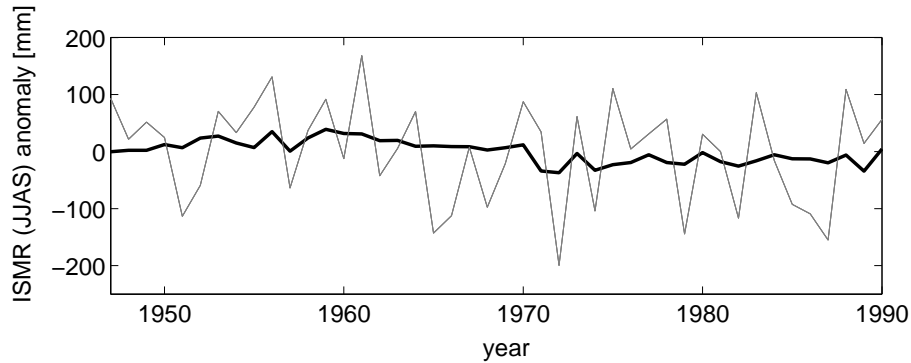


Figure 3.2: Indian summer monsoon rainfall anomalies for the summer months June–September for the model forced with observed temperature anomalies over the Tibetan Plateau from the NCEP/NCAR reanalysis data according to hypothesis (ii) (thick black line). The thin grey line represents the observed ISMR anomalies for JJAS.

on the snow cover. For the relative humidity we do not find any significant correlation in the data. As in our model the temperature difference between Tibet and the equatorial Indian Ocean regulates the Hadley circulation, a change in the temperature  $T_{tib}$  has also an influence on the large-scale circulation. The implemented relationship of Eq. (3.3) leads to a poor simulation of ISMR variability (Fig. 3.1b). The El Niño-ISMR below normal relationship (condition (c)) is captured to some extent but the distribution of the anomalies has a negligible standard deviation, so condition (d) is not met. Summing up, we find a negative influence of ENSO on the temperature over Tibet – implicitly stating a positive effect of ENSO on the snow depth over the Tibetan Plateau – but, in the framework of our model setup, hypothesis (ii) is not able to explain the observed interannual variability of the ISMR induced by ENSO. Although our model is simple and cannot be expected to be able to derive the exact magnitude of the ISMR, the deduced signal is far too small to explain the variance of the ISMR. Even if we choose the coupling coefficient  $\beta$  in Eq. (3.3) in such a way that all observed variability in  $T_{tib}$  is attributed to ENSO, we get a very small signal. Moreover, if we neglect the influence of the Tibetan Plateau on the Hadley circulation (cf. Eq. (3.1)), we obtain an anti-correlation between simulated and observed monsoon variability (not shown here), which again points towards a possible influence of ENSO on the ISMR through the Hadley circulation.

As the influence of snow depth on  $T_{tib}$  is possibly not captured satisfactorily, we also drive the model with the observed temperature and humidity anomalies over the Tibetan Plateau, leading to a low correlation of  $r = 0.23$  (Fig. 3.2). All these investigations lead to the conclusion that, no matter whether the temperature over Tibet is influenced by ENSO, the observed temperature variability over the Tibetan Plateau is not able to explain the observed interannual variability of the ISMR.

It has to be emphasised here that for the influence of ENSO through the SSTs in the Indian Ocean as well as through the temperatures over the Tibetan Plateau, we only include the thermodynamical influences and – except the temperature dependence of the

Hadley circulation – not the dynamical ones, which temperature changes would certainly have.

### 3.2.3 Influence of ENSO on the ISMR through the zonal trade winds

Hypothesis (iii) builds on the picture that ENSO modulates the easterly trade winds in the equatorial Pacific (Peixoto and Oort 1992): under El Niño (La Niña) conditions the easterlies are weakened (strengthened) compared to the normal situation. The trade winds contribute to the advection of heat and moisture according to Eq. (2.16). Analysing the NCAR/NCEP data, we find a positive correlation between the tropospheric zonal wind anomalies<sup>1</sup>  $\Delta u_{tr}$  averaged over India and the Indian Ocean (10-20°N, 60-90°E) and the NINO3 index (cf. Fig. 3.3). The coupling coefficient  $\gamma(z)$  between the trade winds and the NINO3 index has the same height dependence as the trade wind velocity, so that we can write

$$\Delta u_{tr}(z) = \gamma(z) T_{\text{ENSO}} = \gamma \frac{z - h_{tr}}{H_t - h_{tr}} T_{\text{ENSO}} \quad (3.4)$$

with  $(z - h_{tr})/(H_t - h_{tr})$  describing the height dependence and  $\gamma = 1.6 \text{ ms}^{-1}\text{K}^{-1}$  the coupling coefficient derived from Fig. 3.3 with a correlation coefficient of 0.58 corresponding to a 99.9% significance level.

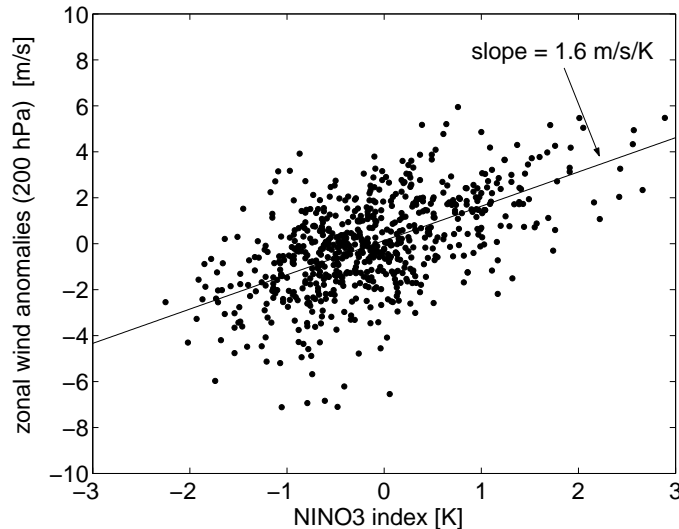


Figure 3.3: Correlation between the NINO3 index and the zonal trade wind anomalies at 200 hPa averaged over 10-20°N and 60-90°E with a five months running mean. The correlation coefficient is 0.58 (99.9% significance level).

Implementing the above relation for the zonal wind anomalies  $\Delta u_{tr}$  in the model, we are able to reproduce the observed monsoon rainfall to a great extent (Fig. 3.1c).

<sup>1</sup>The data for the zonally averaged winds include the trade winds, the Walker circulation and the Tibetan anticyclone. These winds are influenced by a number of other influences that are difficult to separate, e.g. the effect of snow cover over the Tibetan Plateau on the wind stress over the Indian Ocean (Barnett et al. 1989). Implicitly, all these influences are included in this analysis.

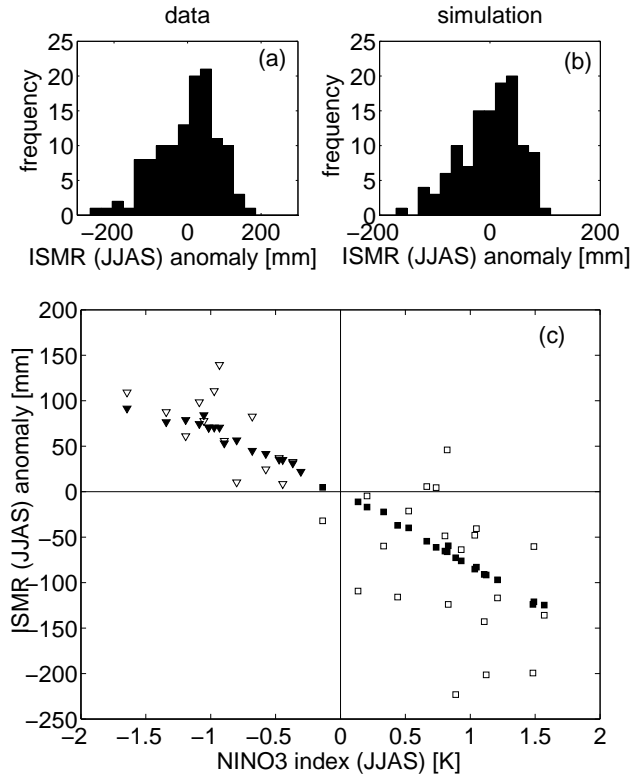


Figure 3.4: Testing hypothesis (iii) that ENSO influences the ISMR through the trade winds (cf. Eq. (3.4)). Comparison of the distributions of the ISMR (JJAS) for (a) the observed and (b) the simulated monsoon rainfall. The standard deviation is (a) 84 mm for the observed and (b) 53 mm in the simulation. (c) Comparison of simulated and observed values for El Niño (square) and La Niña (triangle) years. The unfilled symbols are the observed values, the filled ones stem from the simulation shown in Fig. 3.1c.

The correlation coefficient between simulation and observation is 0.64 and the explained variance reaches 41%. Also, the relationship between El Niño conditions and rainfall below normal is reproduced quite well (cf. Fig. 3.4c). The ISMR standard deviation of 53 mm is too low compared to the 84 mm observed, but the shape of the distribution is captured properly (cf. Fig. 3.4a,b). So all conditions (a)-(d) are accomplished satisfactorily with this mechanism.

Empirical evidence demonstrates that the NINO3 index for June–September is able to explain about 40% of the observed ISMR (JJAS) variance so we can conclude that the influence of ENSO on the Indian summer monsoon occurs to a great extent through the zonal winds as was also pointed out by Webster and Yang (1992). Additionally to the analysis in Webster and Yang (1992) we use a much longer data record to estimate the correlation and show that the correlation is high not only for winter but also for summer. We go one step beyond their data analysis and show that we can reproduce the observed ISMR variability with our model if we include the link through the zonal trade winds.

The results from testing the different hypothesis (i)-(iii) show that only the link through

the trade winds can reproduce the part of the variability of the Indian summer monsoon that is related to ENSO.

### 3.2.4 The influence of ENSO on the ISMR under climate change

Having identified an important physical mechanism between ENSO and the ISMR and being able to reproduce the ENSO induced variability of the monsoon rainfall for the past, we proceed with an investigation of how the monsoon will evolve in the future under climate change. To test whether the identified link between ENSO and the Indian monsoon through the trade winds will persist, the output from the ECHAM5/MPI-OM model forced with the A2 SRES scenario for the years 2000–2100 and a 50-year period of the pre-industrial control run<sup>2</sup> is analysed.

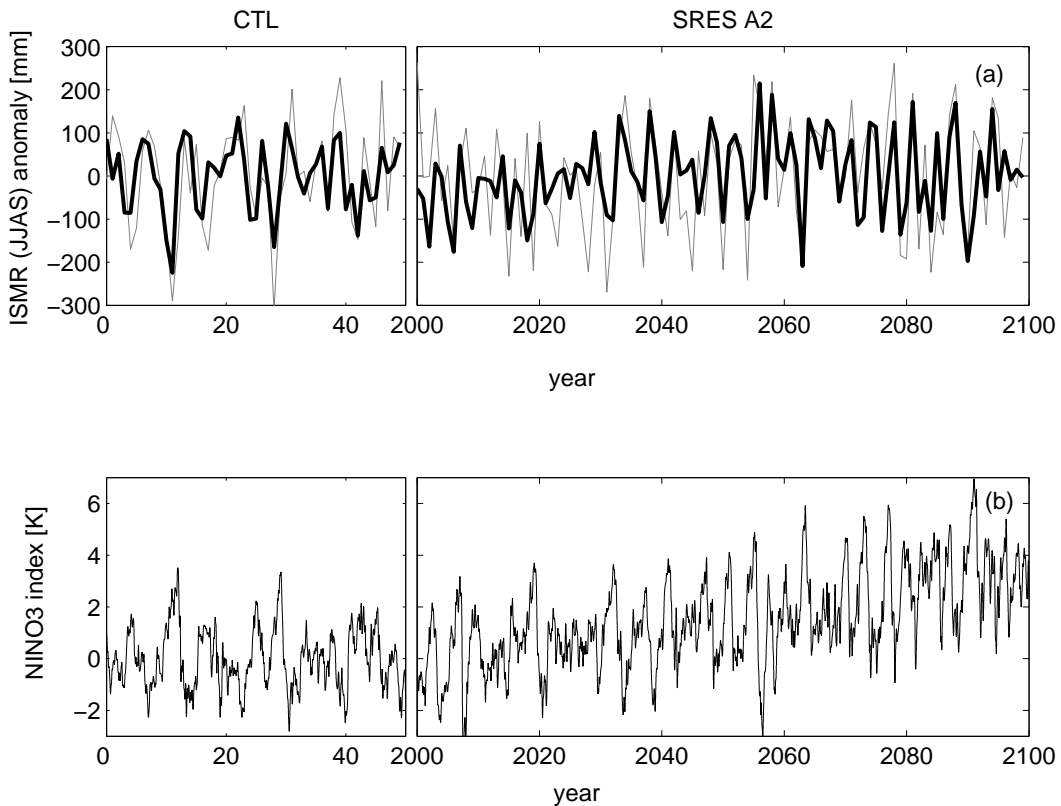


Figure 3.5: (a) Comparison of simulated data for the Indian summer monsoon rainfall anomalies (ISMR) resulting from the box model (thick black line) and from the ECHAM5 runs (thin grey line). On the left is the result for a 50 year control run (CTL), on the right is the result for the SRES A2 scenario. The correlation between the two ISMR time series is 0.63 for the control and 0.59 for the SRES A2 run, (b) monthly mean values for the NINO3 index derived from the ECHAM5 model used to force the box model.

We derive the temperature anomaly  $T_{\text{ENSO}}$  by averaging the SSTs over the NINO3 region from  $5^{\circ}\text{N}$ – $5^{\circ}\text{S}$  and  $150^{\circ}\text{W}$ – $90^{\circ}\text{W}$ . For the Indian rainfall index the precipitation is

<sup>2</sup>Experiment name: IPCC-AR4 MPI-ECHAM5\_T63L31 MPI-OM\_GR1.5L40 P1ctrl(pre-industrial control experiment) and IPCC-AR4 MPI-ECHAM5\_T63L31 MPI-OM\_GR1.5L40 SRESA2 run no.1

averaged over the grid boxes over the Indian subcontinent. We use the time series for  $T_{\text{ENSO}}$  derived from the control and the scenario run to force our box model through the influence of ENSO on the trade winds (Eq. (3.4)). For the coupling coefficient  $\gamma$  we find the same relationship between ENSO and the trade wind anomalies that we have found in the observational data both for the control and the scenario run with ECHAM5, with  $\gamma$  differing only little from the observation-based value (cf. Fig. 3.6). The control run shows a coupling coefficient of  $\gamma_{\text{CTL}} = 1.77 \text{ ms}^{-1}\text{K}^{-1}$ . Under climate change conditions simulated with the A2 SRES scenario this coupling coefficient is slightly decreased to  $\gamma_{\text{A2}} = 1.52 \text{ ms}^{-1}\text{K}^{-1}$ . To test for the significance we apply a z-test (Sachs 1992), with the result that the null hypothesis that the correlations are equal cannot be rejected on the 5% significance level. Therefore, we use the value derived from the observational data (with  $\gamma_{\text{obs}} = 1.6 \text{ ms}^{-1}\text{K}^{-1}$ , cf. Fig. 3.3) for both runs. Implementing the derived values for  $\gamma_{\text{CTL}}$  and  $\gamma_{\text{A2}}$  changes the result only marginally.

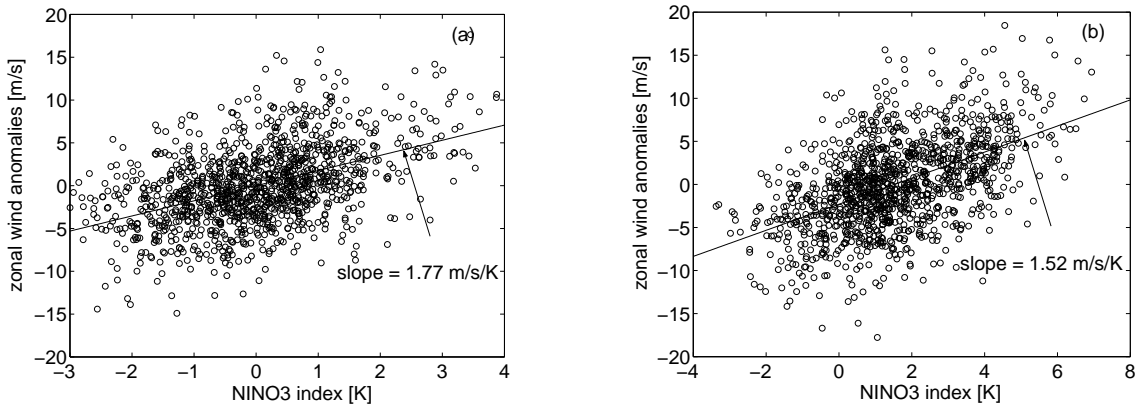


Figure 3.6: Correlation between the NINO3 index and the zonal trade wind anomalies at 200 hPa averaged over  $0^{\circ}\text{N}$ - $20^{\circ}\text{N}$  and  $60^{\circ}\text{E}$ - $90^{\circ}\text{E}$ . (a)  $\gamma_{\text{CTL}}$  for the ECHAM/MPI-OM control run. The correlation coefficient is 0.47. (b)  $\gamma_{\text{A2}}$  for the ECHAM/MPI-OM SRES A2 scenario run. The correlation coefficient is 0.51. Both correlations are significant above the 99.9% level. Compare with Fig. 3.3 for the observational data.

As the boundary conditions will be altered under enhanced  $\text{CO}_2$  emissions we also implement the simulated trend for  $\text{CO}_2$  with additional 500 ppm in 100 years, the ocean temperatures  $T_E, T_W, T_S$  with 3.5 K in 100 years, and the temperature  $T_{\text{tib}}$  with 6 K in 100 years, as derived from the ECHAM5 simulation.

With this setting we can reproduce the simulated ECHAM5 control run as well as the scenario run quite well (cf. Fig. 3.5). For both runs we attain a high correlation of 0.63 and 0.59, respectively, between the summer monsoon rainfall in the ECHAM5 model and the ISMR reproduced by the box model. This result indicates that the physical mechanism linking ENSO and the ISMR remains the same under enhanced greenhouse gas concentrations. One may ask why the trend towards a perpetual El Niño, evident in Fig. 3.5b, goes along with an increase of the ISMR of about 40 mm in 100 years. This can be traced back to the effect that the reduction in monsoon precipitation associated with the trend towards a perpetual El Niño is moderated by the warming over the Tibetan

Plateau and the increasing temperatures in the Indian Ocean.

With the HadCM3 run<sup>3</sup> for the SRES A2 scenario we proceed exactly in the same way and can support the above findings and conclusions. In the HadCM3 SRES scenario run a strong trend towards higher monsoon rainfalls is visible (about 140 mm in 100 years). The trend in the NINO3 index (3.4 K in 100 years) is comparable to the ECHAM results. So are the warming trends over the Tibetan Plateau (6 K in 100 years) and in the Indian Ocean (3.5 K in 100 years). Despite the increase of the NINO3 Index we can reproduce the trend towards higher monsoon rainfall anomalies in the A2 SRES scenario quite well (but reach only an increase in ISMR of 60 mm in 100 years), whereas the variance is largely underestimated (cf. Fig. 3.7). As no data for the trade winds were available for this model run, we took the same coupling coefficient  $\gamma$  as before. The assumption is that the coupling coefficient  $\gamma$  will be larger in HadCM3, but even with a much higher coupling coefficient of e.g.  $\gamma = 5$  the observed variance of HadCM3 cannot be achieved.

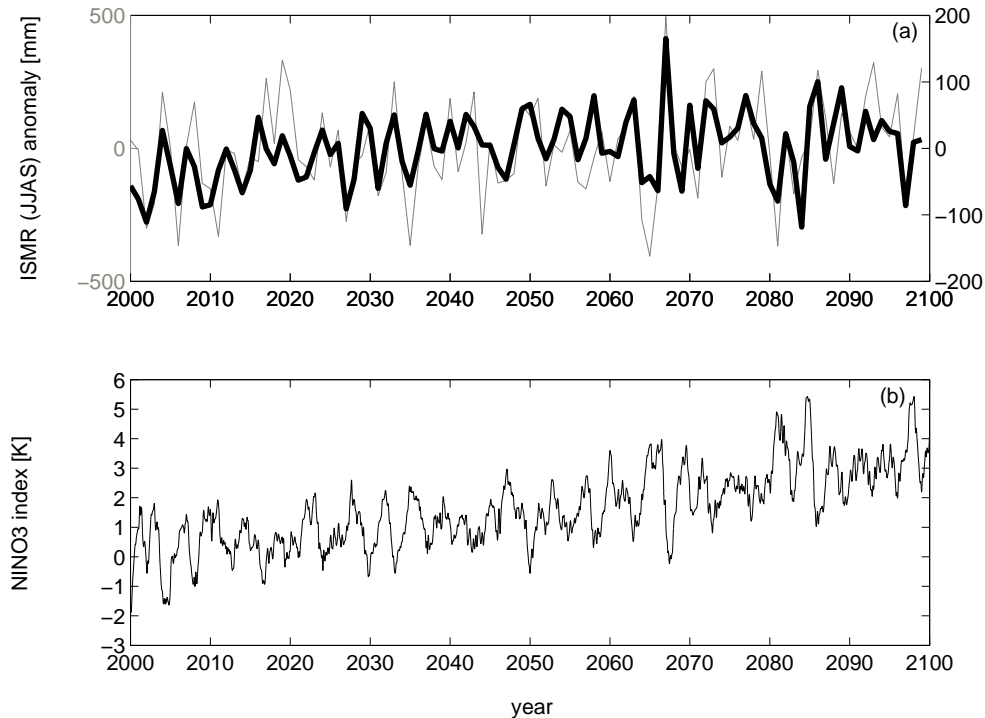


Figure 3.7: (a) Comparison of simulated data for the Indian summer monsoon rainfall anomalies resulting from the box model (thick black line, right axis) and from the HadCM3 SRES A2 run (thin grey line, left axis). The correlation between the two ISMR time series is 0.66, (b) monthly mean values for the NINO3 index derived from the HadCM3 A2 SRES run used to force model. As no data for the trade winds were available, we apply the same coupling coefficient  $\gamma$  as for the observational data.

<sup>3</sup>Experiment name: IPCC-DDC\_HADCM3\_SRES\_A2. As no control run was available we took the years 1950–2000 as a control period.

### 3.3 Conclusions

We have investigated the physical link between El Niño/Southern Oscillation (ENSO) and the Indian summer monsoon rainfall (ISMR) for the past and the future. For the past, we have tested three different physical mechanisms of how ENSO affects the monsoon rainfall. These hypotheses are evaluated by combining observations and results from a box model of the Indian monsoon. We have identified one physical process that may be key in linking the two phenomena: implementing the influence of ENSO on the zonal trade winds enables us to reproduce the historical record of the ISMR with our box model of the Indian monsoon. This mechanism does not seem to be altered in the future under global warming as an analysis of scenario runs with ECHAM5/MPI-OM and HadCM3 suggest. On the other hand, implementing the hypothesis that the Indian monsoon is driven by the influence of ENSO on the snow depth over the Tibetan Plateau is shown to have only a minor influence in our model. The hypothesis that ENSO affects the ISMR via the SSTs in the Indian Ocean yields a negative correlation of the ISMR with the data and can therefore not explain the observations. A major caveat of our approach is that the model is geographically confined, so we cannot investigate the influence of the above mentioned processes on the large scale circulation (with the exception of the Hadley circulation which is parameterised to some extent) and are constrained, e.g., to analyse the thermodynamical and only the local dynamical aspects of the SST changes. Furthermore, as the snow depth is not modelled explicitly, it is possible that we miss an important physical process that may provide a link between ENSO and the Indian monsoon.

Despite these deficiencies, we believe that we are able to capture the ENSO induced variability of the Indian monsoon rainfall to a great extent. Our finding that the key physical link between the two phenomena is provided by the zonal circulation is corroborated by the ability of our model to reproduce both the control as well as the SRES A2 scenario run of ECHAM5 and HadCM3. Furthermore, the physical transparency of the box model and the ability to isolate a certain physical mechanism allowed us to understand the competing processes that determine the future evolution of the ISMR in two GCMs. The fact that we can reproduce the time series of the monsoon rainfall in ECHAM5 and HadCM3 quite well leads to the conclusion that most of the variability on the interannual time scale of the ISMR in these models is induced by ENSO.

Nevertheless, as some part of the variance of the ISMR cannot be reproduced, there is the need for further developments in understanding the mechanisms that determine the variability of the Indian monsoon. This could be the inclusion of other factors than ENSO, such as the Quasi-biennial Oscillation, as suggested by Lau and Yang (1996) or Meehl (1997).

Moreover, as this study just investigates the one-way coupling of ENSO on the ISMR, a next important step is to implement a joint ENSO-monsoon model with a bi-directional coupling, as some studies suggest an influence of the Indian monsoon on ENSO (Ju and Slingo 1995; Wu and Kirtman 2003, e.g.). This issue will again be addressed in the following chapter when the difference between bi-directional and one-way coupling (forcing) is analysed.



## Chapter 4

# Coupled versus forced Models in view of predictability

### 4.1 Motivation and Introduction

The Earth System, including the climate system as well as the anthroposphere, consists of many subsystems (e.g. ocean, atmosphere and vegetation) that strongly interact and are mutually influenced by feedbacks. In this chapter we will draw the attention to uncertainties that originate from the model design incorporating these subsystems and from the interpretation of this design process in terms of predictability.

Parameter uncertainties are of interest in most studies on uncertainty (e.g. Knutti et al. (2002); Forest et al. (2002); Schneider von Deimling et al. (2006)) but their conclusions are often limited to the model under investigation, as we have seen in chapter 2 by investigating the internal uncertainties related to parameters and parameterisations in a model of the Indian summer monsoon. In chapter 3, as a further step we included the structural uncertainty with respect to the mechanism of coupling this specific model with an external forcing due to ENSO. As forcing is a particular type of coupling, we will now go one step beyond and investigate the inherent differences of forcing for example the model of the Indian monsoon with ENSO data instead of considering a fully coupled ENSO-monsoon model. In this chapter we will try to come up with some general conclusions about structural uncertainties concerning the interaction between sub-modules as introduced in Eq. 1.4 and will therefore refrain from analysing this particular monsoon model. This analysis refers to those kinds of uncertainty that are inherent in the modelling process and do not result from a lack of knowledge about the incorporated processes, but from the way of how this knowledge is implemented in the model. We will later show that these uncertainties are indeed intrinsic, i.e. unavoidable and irreducible, within a forced model paradigm. As the aim is to get reliable predictions of future climate evolution, limitations concerning these intrinsic uncertainties of structural differences in the model design and in the process of forcing (instead of coupling) have to be considered carefully and incorporated in the prediction.

In the climate modelling community it is a common practice to establish a modular

structure, consisting of vegetation, ocean, atmosphere, and many more modules that build up an Earth System model (cf. the Climate System Model project CSM (Boville and Gent 1998)). Some of these components are also substituted by an external forcing, prescribed from observed data (Kumar et al. 1996; Bengtsson et al. 1996; Brankovic and Palmer 1997; Quan et al. 2004, e.g.). One very prominent example is the ocean component that is prescribed by observed sea surface temperatures (SSTs). This approach is implemented against the background that the ocean has a strong predictable component. Whereas it is widely accepted that the atmosphere has chaotic elements, which make it impossible to predict the behaviour beyond a few days (Lorenz 1963; Lorenz 1993; Palmer 1993, e.g.), there is a good chance of predicting the ocean dynamics when the two systems are compared on the same time scale. Examples of ocean predictability are the attempts to forecast El Niño (Cane et al. 1986; Behringer et al. 1998; Ji et al. 1998, e.g.) or the SSTs in the North Atlantic that exhibit predictability on decadal to multidecadal timescales (Griffies and Bryan 1997; Collins 2002; Pohlmann et al. 2004, e.g.). Despite the chaotic nature of the atmosphere, seasonal to decadal atmospheric forecasts are possible because of the influence of atmospheric boundary forcings (e.g. the SST). These external driving factors enable the prediction of a mean state of the coupled system. It is therefore the aim of many studies using a general circulation model (GCM) to investigate the seasonal and the regional dependence of the ocean forcing that influences the atmospheric variability and that determines the predictability.

An example, where the substitution of modules with observational data is applied as a standard approach, is the Atmospheric Model Intercomparison Project AMIP (Gates et al. 1992) and AMIP II (AMIP II 2006), where atmospheric GCMs (AGCMs) are constrained by realistic sea surface temperatures and sea ice and the output is used for diagnostics, validation and intercomparison. Although this experiment is not meant to be used for climate change predictions, diagnostic subprojects, e.g. about different kinds of variability or radiative fluxes, have been established, though it is not quite clear to what extent the forced AGCM output is comparable to the system with complex ocean-atmosphere feedbacks. These coupled systems are investigated e.g. in the Coupled Model Intercomparison Project CMIP (Meehl et al. 2000; Covey et al. 2003) where fully coupled atmosphere-ocean GCMs (AOGCMs) adjust to prescribed atmospheric concentrations of CO<sub>2</sub>. The comparison of AOGCMs with simulations using prescribed sea surface temperatures and sea ice shows that there are indeed some important differences concerning e.g. temperatures near the pole and tropical precipitation (Covey et al. 2004). Other studies mention a strong effect of the coupling on the midlatitude variability of the ocean-atmosphere system (Barsugli and Battisti 1998) or on the decadal variability of oceanic variables in the North Pacific (Pierce et al. 2001). Moreover, neglecting the feedbacks from the atmosphere to the ocean can lead to opposite results. This is shown in a study concerning the oceanic pycnocline depth (Levermann and Griesel 2004) by analysing an ocean-only approach with fixed atmospheric conditions by Gnanadesikan (1999).

For predictability purposes ensembles of forced AGCM runs are analysed. This is built on the assumption that the oceanic component is a main driver of the atmosphere and that the chaotic internal variability of the atmosphere can be captured by results from an

ensemble of simulations with different initial conditions. Another reason for analysing the forced instead of the fully coupled run – in addition to the requirement of large computational resources – is that the fully coupled run is not available, e.g. when the AGCM is forced with observational SST data. The forced ensemble mean is then analysed as a proxy of the fully coupled system (Rowell 1998; Kumar et al. 2005, e.g.) implicitly revealing that the true solution will lie within the range of the forced ensemble. Moreover this approach assumes that in an infinite ensemble the errors in the initial atmospheric conditions will cancel out and the ensemble mean will reproduce reality. Bretherton and Battisti (2000) show with a conceptual coupled ocean-atmosphere model that this assumption has to be checked carefully as the variability of the fully coupled system cannot be simulated by an ensemble of SST-forced runs. As conclusions concerning climate variables and physical processes such as precipitation or cloud feedback processes and climate statistics such as climate variability are drawn from forced GCM runs, the crucial question is, to what extent the forced system can serve as a proxy for the fully coupled system and what the limitations of the forced approach are.

Besides the investigation of forced ensemble runs, many attempts have been made to estimate the predictability potentials of GCMs from fully coupled runs. For the prediction on decadal time scales ensemble runs of a coupled AOGCM with the same initial ocean but slightly perturbed initial conditions for the atmosphere are often applied (Grötzner et al. 1999; Pohlmann et al. 2004). The argument put forward in these studies is that a perfect initialisation of the ocean is possible implying that the GCM as well as the observation are perfect<sup>1</sup>

In this chapter we will concentrate on limitations of predictability of forced single or ensemble runs and intrinsic differences concerning the approach of forced versus coupled systems. The focus of this comparison is the analysis of the effect of prescribing a module through data instead of implementing the dynamical model and to deduce the consequences in terms of predictability. The aim is to derive general features and potential constraints preventing the consistency of forcing and coupling. We will present results from forced and coupled GCM ensemble runs and apply different measures of predictability that are widely used in other studies. These measures are compared for the forced and the coupled runs and crucial differences between these two ensembles are pointed out. The phenomena that are found only in the forced as opposed to the fully coupled ensemble are interpreted in terms of similar findings in a conceptual model. For the interpretation we extend the analysis of a conceptual atmosphere-ocean model introduced by Wittenberg and Anderson (1998), which, compared to more sophisticated climate models like GCMs, has the advantage that the model itself as well as the output can be analysed along the lines of dynamical systems theory. The physical transparency of this model makes it feasible to realise path continuation, i.e. the following of solutions in parameter space. The results presented in this chapter reveal the underlying mechanisms for certain artificial phenomena that we found in forced systems (Knopf et al. 2005). From the knowledge of the mechanisms we then conclude that those shortfalls of forced models are generic. Therefore we do not so

---

<sup>1</sup>*Perfect* refers to a situation, where the model can exactly picture reality and where reality can be measured by data without any error.

much suggest to perform path continuation for GCMs as well – although it has successfully been implemented by Dijkstra (2005) –, but the following sections are a motivation to cross-validate a certain class of forced GCM results by alternative coupling designs in quite a classical manner.

In section 4.2 we will present the results from investigating a forced versus a fully coupled GCM ensemble and point out their differences in terms of predictability. We find empirical evidence that forcing instead of coupling yields to fundamentally different conclusions. By virtue of their complexity, GCMs are not suitable to investigate the inherent mechanism behind the discovered phenomenon. Therefore, we introduce a conceptual atmosphere-ocean model in section 4.3 to identify the underlying mechanism and highlight some intrinsic differences of forced and coupled setup. We analyse these differences in terms of dynamical systems theory (cf. section 4.4) and apply standard measures and methods used for the investigation of coupled systems (cf. section 4.5). We will come up with some general conclusions about the interpretation of predictability in forced systems in section 4.6.

## 4.2 Predictability in forced versus coupled GCMs

Several different measures of predictability are used in various GCM studies. One is the model’s *potential predictability* (Zwiers 1987) that is related to the atmospheric component under the assumption that the oceanic forcing can be predicted. Rowell (1998) mentions different approaches to measure this potential predictability, where one widely implemented technique is based on a coupled GCM or an GCM ensemble forced by prescribed SSTs and sea-ice boundaries as described in the introduction. Predictability is then estimated by an analysis of variance (ANOVA) that allows attributing the variability in an ensemble e.g. to the fraction of long term variability such as changing boundary conditions compared to the fraction of internal “natural” variability (Rowell et al. 1995, e.g.). Besides the ANOVA we will introduce here a measure that is related to the *prognostic potential predictability* (Pohlmann et al. 2004).

### 4.2.1 Analysis of variance (ANOVA)

The basic idea behind the analysis of variance (ANOVA) is the examination of differences between the means among group members and within group members of corresponding ensembles. This analysis relates these qualitative differences to the factors that classify the ensemble members. The philosophy for predictability studies is that the variability due to the different initial conditions can be used to quantify the internal variability, whereas the differences between the ensemble members are a measure of the potentially predictable component of variance (Rowell 1998).

As a statistical tool, the ANOVA builds on an F-test and allows separating the total variance of a time series into at least two components (Zwiers 1996): a 1-way ANOVA is often used to analyse the interannual variability (e.g. changing boundary conditions due to SST or sea-ice changes) against the variability induced by weather noise in an observed time series. The 2-way ANOVA is applied for an ensemble of simulations and separates the

variability that is common in all years into two independent factors: into the variability that is due to the deterministic *simulation effect* (Zwiers 1996) that originates e.g. from the simulation on a different computer or from the different model setup of forced and coupled run, and secondly, into the variability that is due to chaotic effects resulting from different initial conditions between the ensemble members.

A detailed derivation of the concept of the ANOVA is given by Zwiers (1996) and von Storch and Zwiers (1999), e.g., here we will only briefly introduce the main ideas and notations and keep close to the notation introduced by Zwiers (1996). The above-mentioned different variances are measured as a ratio in relation to the total variance on a scale of 0%–100%. The idea is to separate the total sum of squares  $TSS$  or total variance into statistically independent components of the variance due to the simulation effect  $SSS$ , the variance due to the boundary effect  $SSB$  and the effect of the natural internal variability  $SSI$ . The simulation effect  $SSS$  can be further subdivided into a component  $SSS_{S\gamma}$  that is related to the different initial conditions in an ensemble of runs and to another one that is related to the configuration effect  $SSS_{Sa}$ , originating e.g. from a forced versus a coupled model set-up:

$$TSS = SSS_{S\gamma} + SSS_{Sa} + SSB + SSI. \quad (4.1)$$

The underlying statistical model of a 2-way ANOVA describes a variable  $X_{sy}$  of the simulation  $s$  at a certain year or time  $y$  and is given by

$$X_{sy} = \mu + \alpha_s + \beta_y + \epsilon_{sy} \quad (4.2)$$

with  $s = 1, \dots, N$  and  $y = 1, \dots, Y$ . In this equation  $\mu$  describes the overall mean and  $\alpha_s$  the effect that is common in all years associated with the simulation  $s$ . This simulation effect  $\alpha_s$  can be divided into a deterministic and a chaotic component. The deterministic component accounts for the simulation on a different computer or for a different model setup as e.g. forced versus coupled configuration and will be denoted as the configuration effect  $a_s$ . The chaotic component of  $\alpha_s$  contains the effect of different initial conditions  $\gamma_s$ . The simulation effect  $\alpha_s$  is the sum of both effects:

$$\alpha_s = a_s + \gamma_s. \quad (4.3)$$

The interannual variation  $\beta_y$  is common for all simulations in year  $y$ . It describes the boundary effect as the SST and sea-ice anomalies constitute this source of variability.  $\epsilon_{sy}$  describes the interannual variations and the weather noise that is supposed to be normally distributed.

Statistical tests can then be implemented to test the significance of hypotheses of the different effects (cf. appendix C). The proportion of the total variance that results e.g. from the boundary forcing effect is given by

$$P_B = \left( SSB - \frac{SSI}{N-1} \right) / TSS, \quad (4.4)$$

for an ensemble of  $N$  simulations. The proportion of the simulation effect due to the initial condition  $P_{S\gamma}$  and due to the configuration  $P_{Sa}$ , respectively, is calculated similarly:

$$P_{S\gamma} = \left( SSS_{S\gamma} - \frac{SSI}{Y-1} \right) / TSS, \quad (4.5)$$

$$P_{Sa} = \left( SSS_{Sa} - \frac{SSI}{Y-1} \right) / TSS. \quad (4.6)$$

A short list of the notations is given in appendix C.

### 4.2.2 Potential predictability and definition of locking

Another measure besides the ANOVA, that is sometimes also referred to as the *diagnostic potential predictability*, is the *prognostic potential predictability* (PPP) that was introduced by Pohlmann et al. (2004), e.g., for the investigation of a fully coupled ensemble. It measures the deviation of a certain variable  $X_i$  of a (forced or coupled)  $N$ -member ensemble of time-length  $n$  from the reference run  $X_{ref}$  that can be the ensemble mean or a fully coupled run:

$$PPP = 1 - \frac{\frac{1}{n} \sum_{t=1}^n \sqrt{\frac{1}{N} \sum_i^N (X_i(t) - X_{ref}(t))^2}}{\sigma(X_{ref})}, \quad (4.7)$$

where  $\sigma(X_{ref})$  is the standard deviation of the reference run. A value close to  $PPP = 1$  refers to perfect predictability where the ensemble runs are very close to the reference run. A value for  $PPP$  near zero means that the ensemble spread is equal to the variance in the reference run.

We will introduce a slightly modified measure that is defined following the concept of  $PPP$ . This measure is motivated by the finding that in an ensemble time series there are episodes when the trajectories are very close together and others where they make up a wide spread. When an ensemble of runs seems to be tied to one single trajectory we will call it *locking*, describing a situation when individual behaviour shifts to a collective behaviour (Briggs and Peat 1989). As an objective measure for locking between  $N$  ensemble members  $X_i$  with  $i = 1 \dots N$  and the reference run  $X_{ref}$  at a time  $t$  we will introduce the *mean locking time*  $\langle \tau \rangle$ . Locking at a time  $t$  is defined when the spread of the ensemble, expressed by  $S_{lock}$ , normalised by the standard deviation of the reference run  $\sigma(X_{ref})$  is smaller than a certain threshold  $\epsilon$ :

$$S_{lock}(t) = \frac{\sqrt{\frac{1}{N} \sum_i^N (X_i(t) - X_{ref}(t))^2}}{\sigma(X_{ref})} < \epsilon. \quad (4.8)$$

Note that in contrast to the formulation of  $PPP$  this is not averaged over the whole time series. The choice of  $\epsilon$  in Eq. 4.8 is somewhat arbitrary but does not alter the interpretation. The mean locking time  $\langle \tau \rangle$  is the sum of all times  $t_{lock}$  when  $S_{lock}(t) < \epsilon$ , normalised by

the length  $T$  of the time series<sup>2</sup>:

$$\langle \tau \rangle = \frac{1}{T} \sum t_{lock}. \quad (4.9)$$

In other words, the mean locking time  $\langle \tau \rangle$  gives the fraction of locking for a time series and is a measure, how close the ensemble members and the reference run are. This measure has the advantage of being able to additionally identify short time intervals when the trajectories are close together, which would average out using the formulation of *PPP*.

Both measures of predictability, the ANOVA and the mean locking time  $\langle \tau \rangle$ , are applied to analyse the results from a GCM experiment. First we will use the phenomenological measure of the mean locking time and later relate the results to the quantitative analysis of variance.

### 4.2.3 GCM experiments: model setup

The question to be addressed in this section is whether a forced AGCM ensemble differs qualitatively from its fully coupled counterpart in terms of predictability. For our study we investigate an ensemble of one coupled and four forced simulations of the ECHAM3/LSG model. The ECHAM3/LSG model is a fully coupled ocean-atmosphere GCM with ECHAM3 as the atmospheric component (Roeckner et al. 1992) and the Large Scale Geostrophic (LSG) (Maier-Reimer et al. 1993) model as the oceanic component.

One fully coupled ECHAM3/LSG run with a length of 100 years – extracted from an 800-year control run – serves as the reference run. Furthermore, four atmosphere-only simulations with the ECHAM3 model are available<sup>3</sup> where the SSTs and the sea-ice are prescribed from the coupled reference run. These four runs differ only in their initial atmospheric conditions. With this setting the experiment is comparable to studies that implement observational data for diagnostic purposes. We will investigate the monthly mean values here, so 1200 records are available for each run, which we analyse in the deseasonalised form by removing the mean seasonal cycle. For the analysis of the forced runs the 2-meter temperature  $T_{2m}$  and the 500 hPa geopotential height  $\Phi_{500}$  are evaluated. The detailed experimental setup can be inferred from Friederichs and Hense (1999).

A second forced ensemble from the Hadley Centre model HadCM3 (Gordon et al. 2000) is available with a similar experimental setting as before with one fully coupled and three forced runs. Here we analyse the temperature  $T_{2m}$  and the 850 hPa temperature  $T_{850}$ .

For the comparison of forced and coupled dynamics a fully coupled ensemble is analysed. The ensemble consists of five coupled ECHAM5/MPI-OM (Roeckner et al. 2003) runs, with monthly mean values for a length of 20 years. Every run starts with the same oceanic conditions and differs only in the atmospheric initial conditions. This setup is therefore comparable to the forced ensemble, despite the fact that the ocean evolves in a coupled manner with a feedback from the atmosphere. The variable to be analysed is the 2-meter temperature  $T_{2m}$ .

<sup>2</sup>We will only declare it a locking period when the series of locking times  $S_{lock}(t)$  lasts for at least three time units to avoid random equality.

<sup>3</sup>These runs were carried out by Petra Friederichs from the Meteorological Institute Bonn.

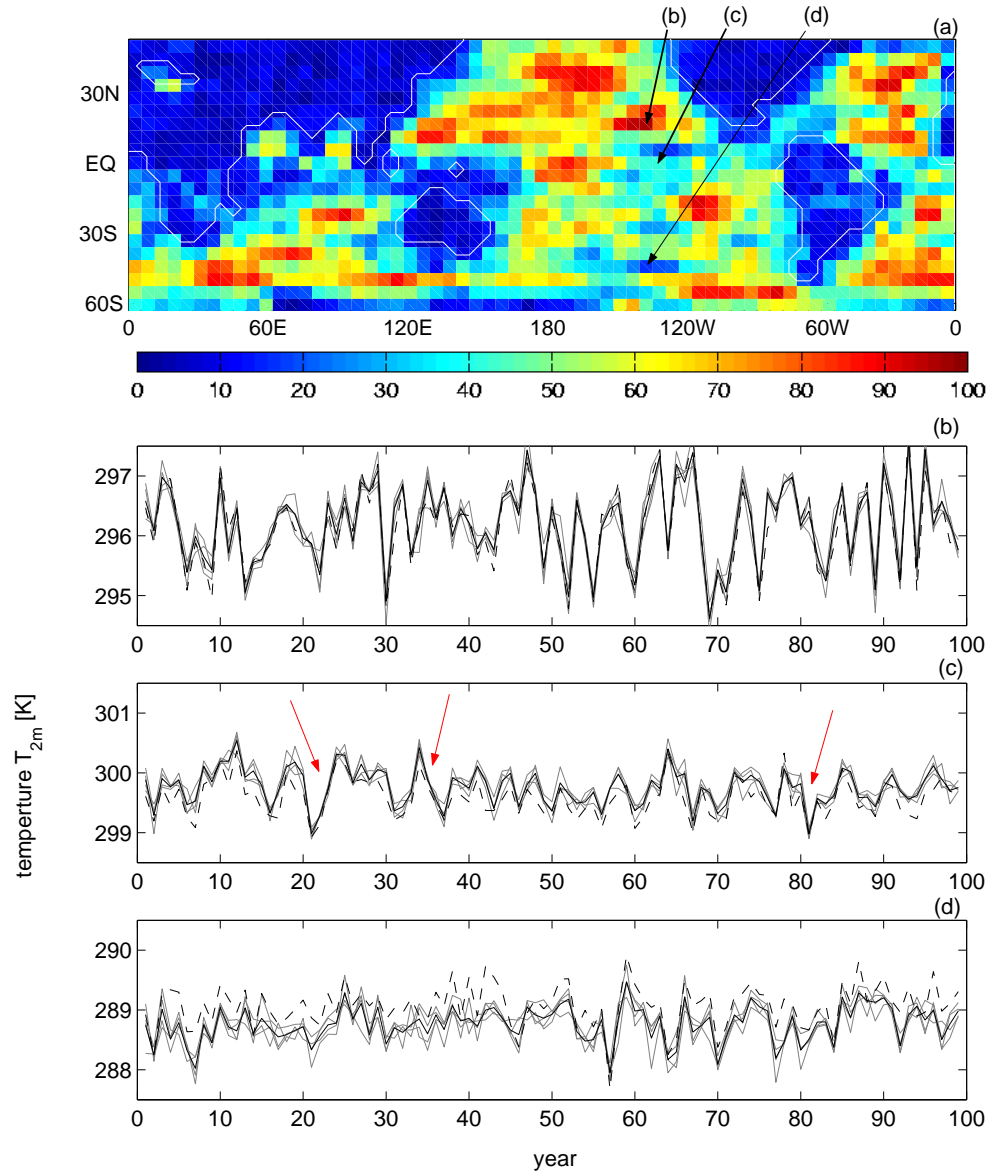


Figure 4.1: (a) Percentage of mean locking time  $\langle \tau \rangle$  for the temperature  $T_{2m}$  for the season DJF between the fully coupled reference run and the forced ensemble. (b), (c), and (d) are examples of time series for DJF of the temperature  $T_{2m}$  for the three regions that are marked with arrows in (a). The dashed black line is the reference coupled run, the straight black line is the forced ensemble mean and the grey lines are the four forced ensemble members. (b) Example of locking, (c) example of intermittent locking (red arrows), and (d) example of the absence of locking.



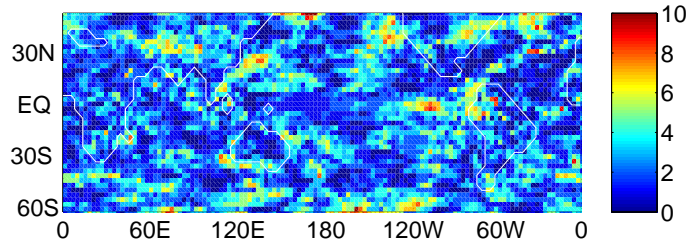


Figure 4.2: Percentage of mean locking time  $\langle \tau \rangle$  for the fully coupled ECHAM5 ensemble for the temperature  $T_{2m}$  for DJF.

#### 4.2.4 GCM results: mean locking time

We will first concentrate on the forced ECHAM3 ensemble and calculate the mean locking time  $\langle \tau \rangle$ , as defined in Eq. 4.9, for the winter season (December-February, DJF) in Fig. 4.1a, where we take the fully coupled run as reference in Eq. (4.8). We choose  $\epsilon$  in such a way that the differences between locking and no locking can be captured adequately<sup>4</sup>. One would expect that the locking between the forced runs and the fully coupled run is longer over the ocean than over land due to the SST forcing. Indeed, this is the case, but an interesting observation is that this correlation, expressed through the mean locking time  $\langle \tau \rangle$ , is not distributed equally, but is much stronger in some regions over the ocean. For the Northern Hemispheric winter locking regions can be identified, e.g. in the North Atlantic ( $45^\circ\text{N}$ ,  $20^\circ\text{W}$ ), in the North-eastern Pacific ( $20^\circ\text{N}$ ,  $140^\circ\text{W}$ ) in the subtropical Pacific near Peru ( $20^\circ\text{S}$ ,  $120^\circ\text{W}$ ) or in the Northern Pacific ( $40^\circ\text{N}$ ,  $160^\circ\text{W}$ ). On the other hand there are also regions where  $\langle \tau \rangle$  is quite small, e.g. at ( $5^\circ\text{N}$ ,  $130^\circ\text{W}$ ) or at ( $45^\circ\text{S}$ ,  $140^\circ\text{W}$ ), implying that the trajectories do not show any locking. To get an impression of the corresponding time series we plot the trajectories exemplarily for three different regions (cf. Fig. 4.1b-d). In the locking regions the forced runs, the ensemble mean, and the fully coupled run are more or less on one trajectory (cf. Fig. 4.1b). In other regions the coupled and the forced runs differ qualitatively and only intermittent locking or nearly no similarity between the ensemble runs and the fully coupled reference run is observed (cf. Fig. 4.1c,d). In the latter case the fully coupled run and the forced ensemble display different trajectories and subsequent results from the conceptual model will let us assume that the trajectories reside on different manifolds in state space. Intermittent locking, as observed in Fig. 4.1c, is also reported in other studies: Schlosser and Kirtman (2005) show that some – but not all – of these locking periods, which they identify as predictable, are associated with El Niño / La Niña events.

To test whether this locking can also be seen in a coupled ensemble, we analyse the fully coupled ECHAM5 ensemble that only differs in the atmospheric initial conditions. Fig. 4.2 shows the mean locking time  $\langle \tau \rangle$  for the five fully coupled ECHAM5 runs. Comparing this plot with Fig. 4.1a it can clearly be seen that the locking time is much shorter and

<sup>4</sup>The result presented does not depend on the choice of the threshold  $\epsilon$ , provided that  $\epsilon$  is not too small. Here we choose  $\epsilon = 0.6$

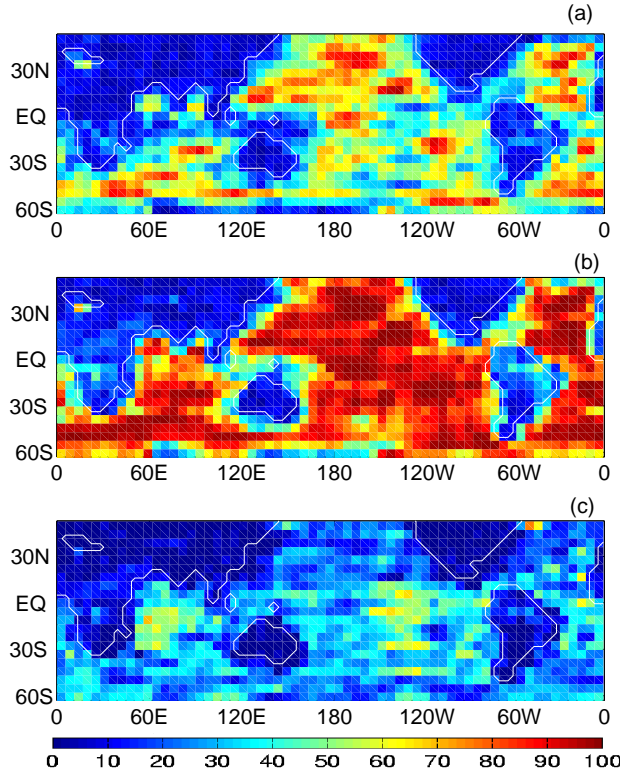


Figure 4.3: Percentage of mean locking time  $\langle \tau \rangle$  for the temperature  $T_{2m}$  for DJF (a) with the fully coupled run as the reference in Eq. 4.8, (same as Fig. 4.1a), (b) with the forced ensemble mean as the reference in Eq. 4.8, (c) the difference plot of (b)-(a).

achieves maximal 10%. Moreover, no regional structure with a longer locking time over the oceans can be identified. Although ECHAM3 and ECHAM5 have to be regarded as different models, it can be concluded that forced and coupled setup show some fundamental differences that will be further investigated in the following.

When taking the forced ensemble mean from the ECHAM3 runs as the reference in Eq. (4.8), we get a much higher value for the locking time (cf. Fig. 4.3b) than with the coupled run as the reference (cf. Fig. 4.3a). Two conclusions can be drawn from the comparison of Fig. 4.3a with Fig. 4.3b: In the regions, where no locking can be observed it is not mandatory that all trajectories differ from each other. On the contrary, in these regions all forced trajectories are bound together and lock on the same trajectory over long times whereas they are not consistent with the fully coupled run. This provides further evidence for the assumption that in these regions forced and coupled runs are not on the same manifold. Secondly, the difference plot of both approaches in Fig. 4.3c shows that predictability is overestimated when using the ensemble mean as a reference. Those parts where the difference is large indicate that on the one hand the ensemble spread is small but that on the other hand the forced ensemble mean and the “true” coupled run do not bear much similarity. Moreover, we can conclude that the spread of a forced ensemble

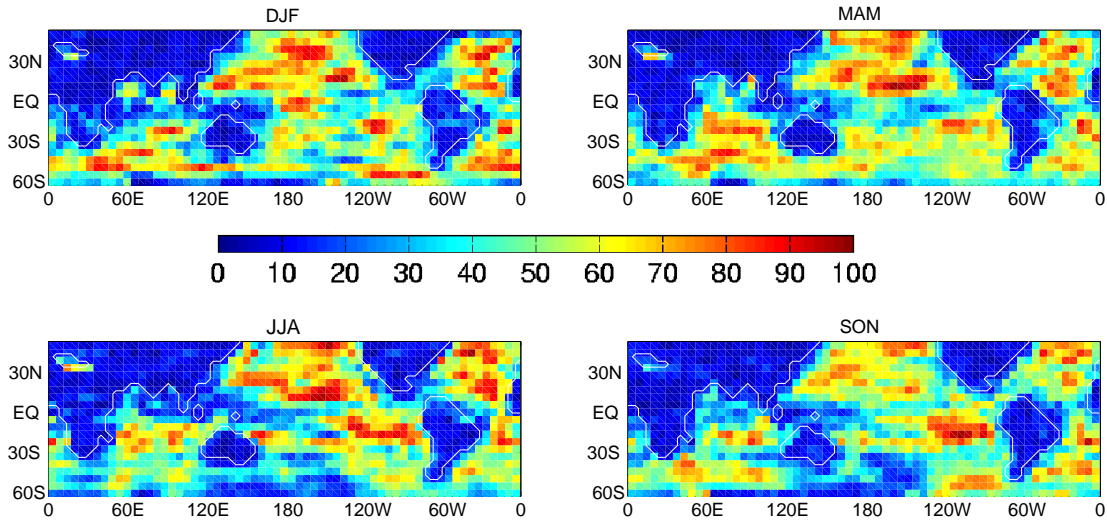


Figure 4.4: Seasonal variation of the mean locking time  $\langle \tau \rangle$  for the temperature  $T_{2m}$ . Percentage of locking time for the seasons DJF, MAM, JJA and SON.

– measured by the locking time  $\langle \tau \rangle$  with the ensemble mean as the reference – is not always an appropriate indicator for predictability, although this approach is often applied (Rowell 1998; Rodwell et al. 1999; Mehta et al. 2000, e.g.).

The locking regions show a strong seasonal dependence as can be seen from Fig. 4.4 where  $\langle \tau \rangle$  is plotted for the seasons DJF, March-May (MAM), June-August (JJA) and September-November (SON). The ENSO region in the equatorial eastern Pacific at the coast of Peru and the North Atlantic is pronounced in nearly every season but the dispersal of the region differs. It is important to note that there are also regions, differing from season to season, where the locking time is very short, indicating a non-similarity between coupled and forced runs. The seasonal dependence of the locking could possibly be explained by the influence of low stratiform clouds, as the comparison of Fig. 4.5 with Fig. 2 in Klein and Hartmann (1993) suggests.

From this preliminary analysis we have seen that there are indeed differences between a fully coupled and a forced model setup and that the forced ensemble mean is not always an appropriate proxy for the fully coupled run. The question remains which mechanism prevents the similarity between these two approaches. As a further step we implement an analysis of variance to separate the different causes of variability in this experiment.

#### 4.2.5 GCM results: analysis of variance

We perform a 2-way ANOVA, similarly to the analysis carried out by Friederichs (2000) for the same runs, but we will focus more on the configuration effect than on the boundary effect. Again we analyse the seasonal values for DJF for the temperature  $T_{2m}$ . The variability  $P_B$  (cf. Eq. 4.4 and appendix C) that can be explained through the changing

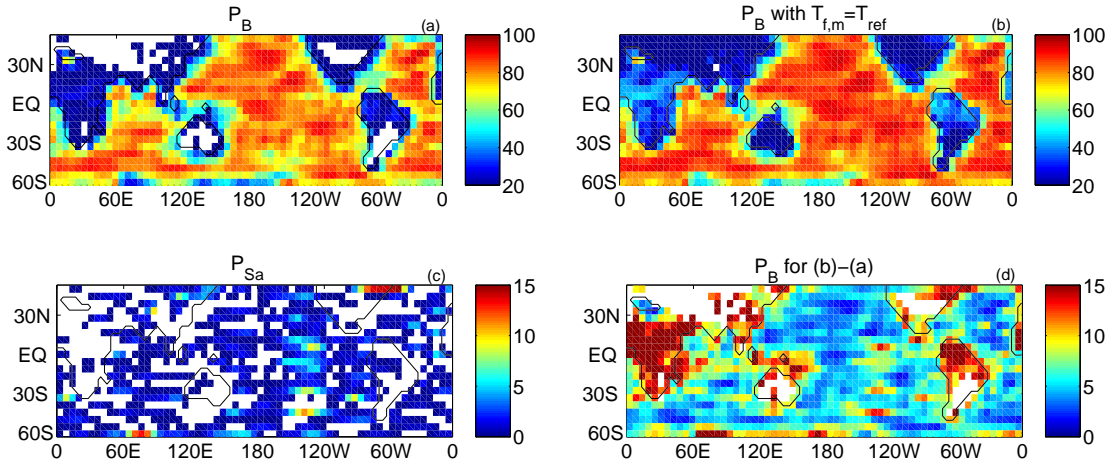


Figure 4.5: ANOVA of the temperature  $T_{2m}$  for DJF. The colours represent the percentage of the total variance. (a) Percentage variance  $P_B$  due to changing boundary conditions (i.e. SST and sea-ice boundaries) with the coupled run as reference on a 99 % significance level, (b) the same for the forced ensemble mean as the reference run, (c) percentage variance  $P_{Sa}$  due to the configuration effect of forced versus coupled setup on a 95 % significance level and (d) difference plot of (b)-(a) for  $P_B$ .

boundaries (here SST and sea-ice anomalies) is plotted in Fig. 4.5a and shows that the SST induced variance is large over the whole ocean. Regions that are more pronounced and show a higher SST induced variance coincide well with the regions where the locking time is large (compare with Fig. 4.4a). On the other hand, the mechanism generating regions where the mean locking time  $\langle \tau \rangle$  is short (e.g.  $5^\circ\text{N}$ ,  $130^\circ\text{W}$ , cf. Fig. 4.4a), can be attributed to the effect of the different setup of forced and coupled runs  $P_{Sa}$  (cf. Eq. 4.6), as Fig. 4.5c suggests. The influence of the different initial conditions of the forced runs are negligible against it as the explained variance  $P_{S\gamma}$  (cf. Eq. 4.5) reaches a highest value of only 3% (not shown here). When analysing the variability  $P_B$  with the ensemble mean as a reference, we attain a similar pattern (cf. Fig. 4.5b), but again it can be concluded that the predictability is overestimated by up to 20 % in some regions as the difference plot in Fig. 4.5d suggests. Note that these are just those regions that show a high degree of explained variance due to the configuration effect (compare Fig. 4.5c and Fig. 4.5d).

The region where the configuration effect  $P_{Sa}$  plays a major role does not show a strong seasonal dependence (cf. Fig. 4.6). Although the locking regions have a different seasonal pattern (cf. Fig. 4.4) the discrepancy between forced and coupled approach seems to be very pronounced in the region ( $30^\circ\text{S}$ - $60^\circ\text{S}$ ,  $140^\circ\text{W}$ - $120^\circ\text{W}$ ). This could be a hint that regions, where the configuration effect has a remarkable influence, are more or less universal and not seasonally dependent. Of course, these regions will be specific for every variable and every model.

The same correlation as described above between locking and explained variance through

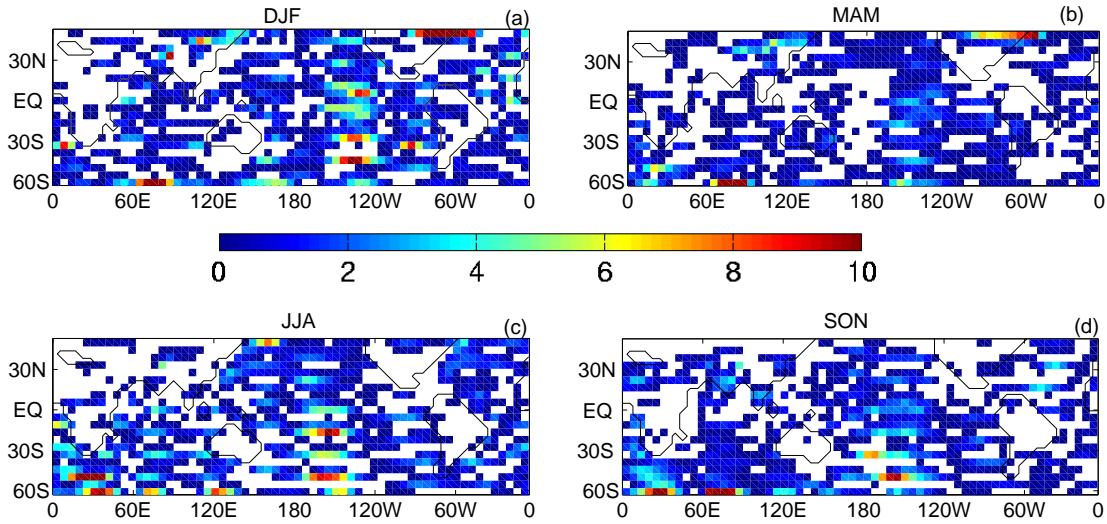


Figure 4.6: ANOVA of the 2m-temperature: seasonal dependence of the explained variance  $P_{Sa}$  due to the configuration effect on a 95% significance level for the seasons DJF, MAM, JJA, and SON. The colours represent the percentage of the total variance.

SST anomalies on the one hand and no locking (or divergence between the trajectories) and explained variance through the different configurations (forced versus coupled set-up) on the other hand is found for several variables. An illustrating example is the 500 hPa geopotential height as shown exemplarily for two regions in Fig. 4.7. In the equatorial region we find a strong locking that is most pronounced in the central Pacific (cf. Fig. 4.7a). For the region over Indonesia and the Bay of Bengal the locking time is very short and in the time series in Fig. 4.7c the forced ensemble shows not only an offset, but the variability is also not consistent with the fully coupled run. This underlines the shortcomings of forced runs, as they are not always able to capture the behaviour of the fully coupled system. The discrepancy between coupled and forced runs can again be attributed to the configuration effect, as the ANOVA shows (cf. Fig. 4.8). Over 60% of the variance in the region over the Bay of Bengal can be attributed to this effect. The Bay of Bengal and the region over Indonesia are known to be most influential for the world's climate. The fact that – at least in this model and in this experiment – the forced setup is not able to picture this region correctly should be kept in mind when interpreting forced model results. The effect of the initial conditions, however, is again very small and not plotted here. As before, taking the ensemble mean as the reference would overestimate the predictability by up to 30%.

Results from a similar setup with the Hadley Centre model HadCM3 confirm the above findings. Here we will only show the results for the 850 hPa temperature  $T_{850}$ , as the effect of the forcing can hardly be identified for the temperature  $T_{2m}$ . Fig. 4.9 shows that again there are pronounced regions where the configuration effect plays a role. However, in this case the percentage of explained variance through the configuration effect  $P_{Sa}$  is

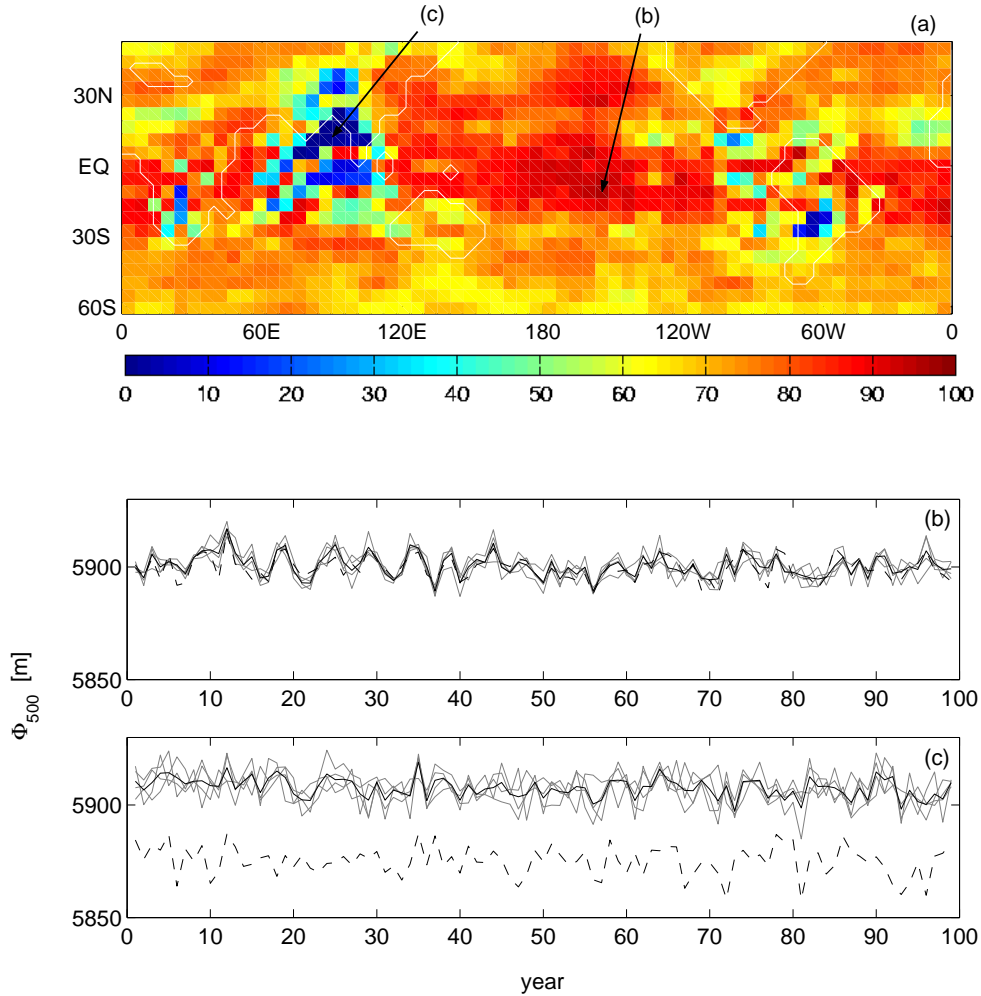


Figure 4.7: (a) Percentage of mean locking time  $\langle \tau \rangle$  for the 500 hPa geopotential  $\Phi_{500}$  for DJF. (b) and (c) are examples of the time series for the regions that are marked above. The dashed black line is the reference coupled run, the straight black line is the forced ensemble mean and the grey lines are the four forced ensemble members. (b) Example of locking and (c) example of the absence of locking.

much smaller. The higher value in the ECHAM3 runs could be due to the particular experimental setting, where the deep ocean is calculated only once a month, whereas the upper two layers of the LSG model have a time step of one day and the atmospheric component a time step of 20 minutes.

The above results show that there can exist periods in time as well as fractions in space where a fully coupled atmosphere-ocean GCM and an atmosphere-only GCM forced by SSTs and sea-ice from a fully coupled reference run bear some important differences: (i) the forced runs do not always evolve according to the fully coupled run, forced and coupled run are intermittently distinct, (ii) predictability is overestimated when only analysing the forced ensemble, and (iii) the forced ensemble mean is not an adequate proxy for the fully coupled system. Nevertheless, in most cases the forced ensemble is a conformable

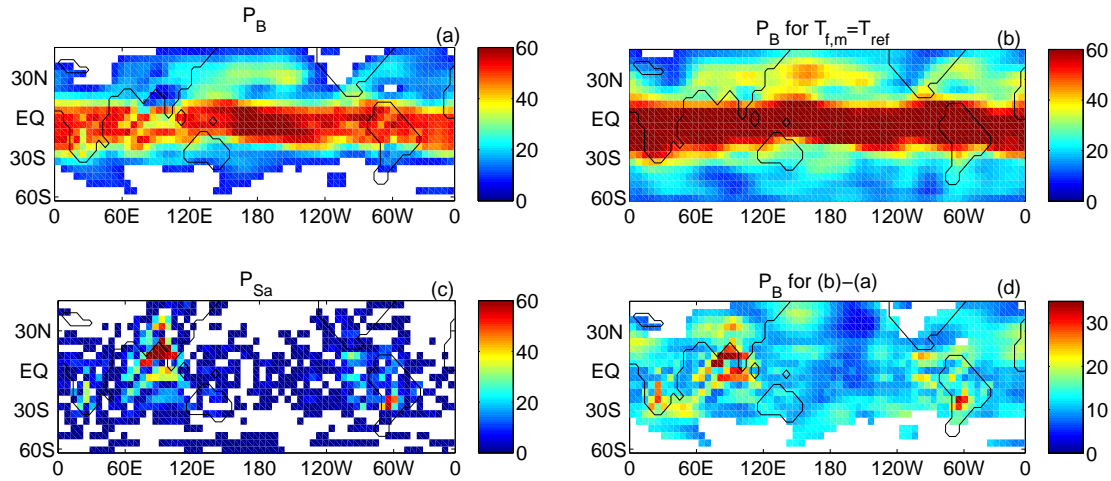


Figure 4.8: ANOVA of the 500 hPa geopotential for DJF. The colours represent the percentage of the total variance. (a) Percentage variance  $P_B$  due to changing boundary conditions (i.e. SST and sea-ice boundaries) with the coupled run as reference on a 99 % significance level, (b) the same for the forced ensemble mean as the reference run, (c) percentage variance  $P_{Sa}$  due to the configuration effect of forced versus coupled setup on a 95 % significance level and (d) difference plot of (b)-(a) for  $P_B$ .

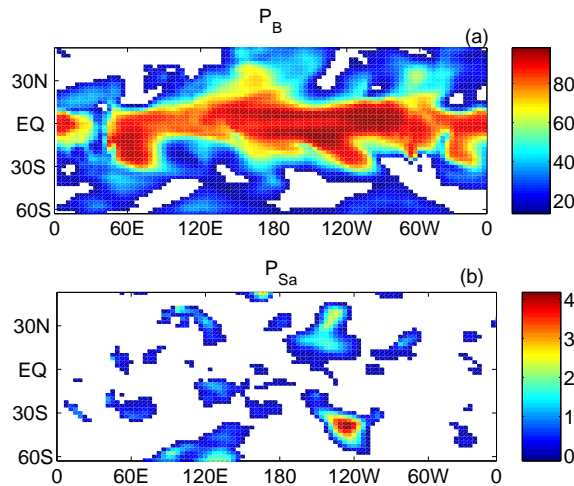


Figure 4.9: ANOVA for the 850 hPa temperature  $T_{850}$  for the HadCM3 model for DJF. (a) Percentage variance  $P_B$  due to changing boundary conditions (i.e. SST and sea-ice boundaries) with the coupled run as reference on a 99 % significance level, (b) percentage variance  $P_{Sa}$  due to the configuration effect of forced versus coupled setup on a 95 % significance level.

reproduction of the fully coupled system. The question to be followed in the next section is what prevents the similarity of forced and coupled setup and what is the inherent mechanism behind it? To analyse this phenomenon we will investigate a conceptual model in order to be able to utilise methods from dynamical systems theory to identify the underlying mechanism.



## 4.3 Predictability in a forced versus a coupled conceptual model

### 4.3.1 Model setup

In the last section we have found empirical evidence that forcing a GCM with prescribed data instead of analysing the fully coupled system yields to some fundamental differences in terms of predictability. GCMs are highly complex models with a large amount of degrees of freedom and are therefore not suitable for the application of most methods from dynamical systems theory, such as path following of stable states or the analysis of long runs with several ensemble members. Hence, in this section we will introduce a conceptual model and will refer to results that we presented in Knopf et al. (2005).

We investigate the difference between a forced and a fully coupled set-up, considering a conceptual coupled atmosphere-ocean system as an instructive example:

$$\dot{x} = -y^2 - z^2 - ax + a(F + \sin(2\pi\gamma t)) \quad (4.10)$$

$$\dot{y} = xy - cy - bxz + G + \alpha p \quad (4.11)$$

$$\dot{z} = xz - cz + bxy + \alpha q \quad (4.12)$$

$$\dot{p} = -\omega q - \beta y \quad (4.13)$$

$$\dot{q} = \omega p - \beta z \quad (4.14)$$

This model is taken from Wittenberg and Anderson (1998) and has also been investigated by Roebber (1995). The atmosphere system model (Eqs. (4.10)–(4.12)) is a potentially chaotic Lorenz system (Lorenz 1984), that describes the midlatitude quasi-geostrophic flow. While  $t$  represents the time, the variable  $x$  represents the intensity of the westerly wind current or the meridional temperature gradient. The variables  $y$  and  $z$  are the amplitudes of the sine and cosine components of a large travelling wave, which transports heat poleward.  $F$  and  $G$  are forcing terms based on the average north-south temperature contrast and the land-sea temperature contrast, where the seasonal variation of  $F$  is expressed through the sine. The ocean system is a simple harmonic oscillator, with an oscillation frequency  $\omega$  of four years, where  $p$  and  $q$  represent zonal asymmetries in sea surface temperature. The coupling between ocean and atmosphere proceeds through the interaction of these asymmetries with the model atmosphere’s eddy field ( $y$  and  $z$ ). The parameters have the following values:  $a=0.125$ ,  $F=3.5$ ,  $c=0.5$ ,  $b=4$ ,  $\alpha=\beta=0.1$ ,  $G=0.25$ ,  $\gamma=10/365.25$ ,  $\omega=2\pi\gamma/4$ , where  $\gamma$  is a scaling factor with one unit of system’s time referring to 10 days.

Wittenberg and Anderson (1998) carried out two different sets of simulations. One set of simulations represents the outcome of the fully coupled system with little variation in the initial state vectors of the atmosphere. In the other set the output of the ocean from one special run (the reference or “true” run) is used to force the atmosphere. Again this is done for slightly perturbed initial conditions. In doing so, this set-up is comparable to the GCM experiments that we have analysed in section 4.2: we have one ensemble from a fully coupled system and one from a forced system that excludes the feedback from the

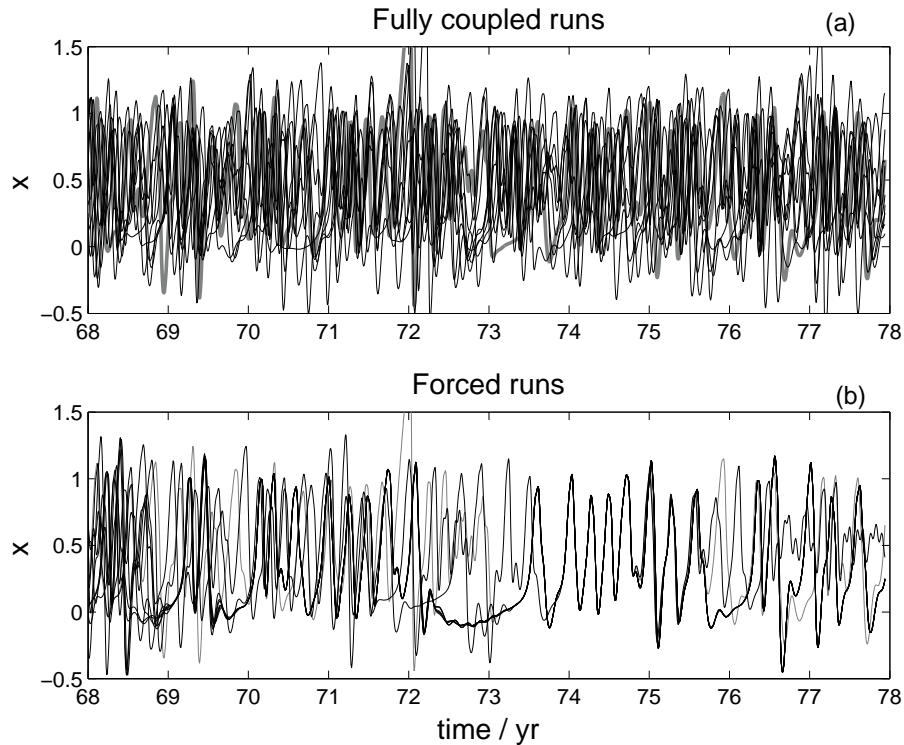


Figure 4.10: Comparison of the fully coupled system (top) and the forced system (bottom) according to Eq. (4.10)–(4.14). (a) Fully coupled ensemble with varying initial conditions in atmospheric coordinates. (b) Forced ensemble, where one run from the above figure (a) is taken as a reference run. The trajectories are forced by the ocean from the reference trajectory where they again vary in their initial atmospheric conditions. In this figure, we have reproduced a major finding by Wittenberg and Anderson (1998) as a starting point.

atmosphere to the ocean.

As can be seen from Fig. 4.10, which, as a starting point, reproduces a major finding by Wittenberg and Anderson (1998), the forced ensemble is more compact, but does not mirror the true solution. A forced set-up is normally implemented with the aim that either the ensemble mean displays the fully coupled system or that the forced ensemble mirrors the “true” variability. We see from Fig. 4.10b that the first challenge is not fulfilled. Furthermore, Wittenberg and Anderson (1998) show that the statistics of the forced variability, like spatial and temporal distributions, are significantly different from those of coupled variability. For modelling issues this means that a prescribed forcing (e.g. prescribing the SST) does not emulate the fully coupled system in several characteristics. The interesting effect of the forcing is that all trajectories sometimes lock on the true solution for a short time and then separate again, so intermittent locking or partial synchronization can be observed similarly or even more pronounced as we have seen for the forced GCM ensemble in Fig. 4.1c. One can conclude from this on the one hand that fully coupled and forced systems do not show the same behaviour but on the other hand that in truly forced systems there may exist a region in phase space, where predictability is very high. The

question to be followed is what mechanism is responsible for the locking phenomenon and whether this is due to a certain type of coupling.

### 4.3.2 Mathematical framework

In order to explain the phenomenon of locking, a stability analysis of the system appears the most natural approach. In the tradition of Wittenberg and Anderson (1998) and Smith et al. (1999), one would expect that the local linear stability properties govern the observed phenomenon. Empirically, however, we find that the explanation for locking given in Wittenberg and Anderson (1998) does not hold. We find that locking shows no correlation to the trajectory's residence in the "locking region" identified in Wittenberg and Anderson (1998) and, in particular, that locking persists an order of magnitude longer than the trajectory resides in the locking region<sup>5</sup>. Contrary to a local linear stability analysis, we will relate the locking period to extended invariant manifolds, emerging from the nonlinear dynamics of the system. This will allow us to introduce meaningful time-averaged characteristics. To frame a discussion of potential nonlinear causes of locking, we follow the concepts of Pecora and Carroll (1990) and Pecora et al. (1997). Different from Fig. 4.10, where we looked at a set of several forced trajectories, we investigate here just the fully coupled run and one forced run. The forced system can be written as a so-called replica system (Pikovsky et al. 2001), where a replica of one or more equations is made. Together with Eqs. (4.10)–(4.14) we have a replica system of the following form:

$$\dot{x}' = -y'^2 - z'^2 - ax' + a(F + \sin(2\pi\gamma t)) \quad (4.15)$$

$$\dot{y}' = x'y' - cy' - bx'z' + G + \alpha p \quad (4.16)$$

$$\dot{z}' = x'z' - cz' + bx'y' + \alpha q \quad (4.17)$$

$$\dot{p}' = -\omega q' - \beta y' \quad (4.18)$$

$$\dot{q}' = \omega p' - \beta z', \quad (4.19)$$

where the primed system  $\mathbf{x}'=(x', y', z', p', q')^T$  is identical to the original fully coupled system  $\mathbf{x}=(x, y, z, p, q)^T$  except for slightly different initial conditions and the substituted variables  $p$  and  $q$  instead of  $p'$  and  $q'$ , that emulate the forcing through prescribed data. In this system  $p'$  and  $q'$  have no influence on the dynamics of the other primed variables and are only introduced to allow for a closed mathematical form. With this formalization we apply a perfect model scenario as the "data" originate from the same model. The influence of model errors will be the focus of section 4.4.5.

In Fig. 4.11 the norm of the error vector  $\delta\mathbf{x}=|\mathbf{x}-\mathbf{x}'|$  is plotted. Sometimes the two systems synchronize but then suddenly the system shows long-lasting bursts, where the two trajectories seem to evolve independently. Generally, this type of coupling between

---

<sup>5</sup>Here a locking region refers to a period in the time domain and not as in section 4.2 in the space domain on the model grid.

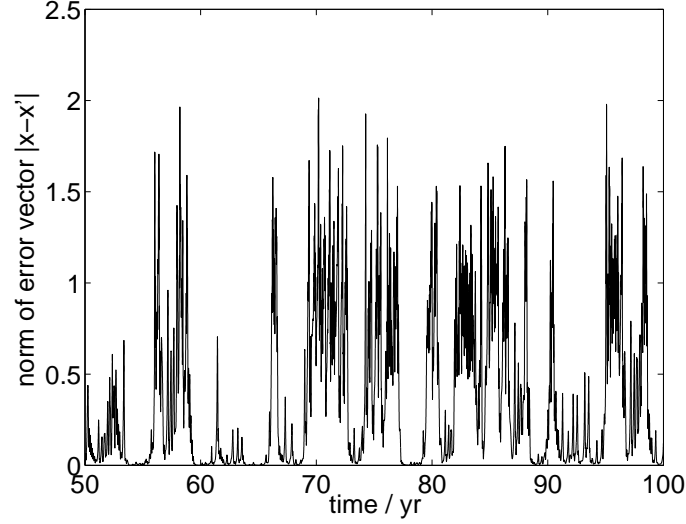


Figure 4.11: Norm of the error vector  $\delta\mathbf{x}=|\mathbf{x}-\mathbf{x}'|$  between the fully coupled and the forced run; ( $a=0.09$ ).

two identical systems can be written as

$$\begin{aligned}\dot{\mathbf{x}} &= \mathbf{F}(\mathbf{x}) \\ \dot{\mathbf{x}}' &= \mathbf{F}(\mathbf{x}') + \mathbf{K}(\mathbf{x} - \mathbf{x}'),\end{aligned}\tag{4.20}$$

where  $\mathbf{K}$  is the coupling function.

By transforming Eq. (4.20) to the transversal coordinates  $\mathbf{x}_\perp = \mathbf{x} - \mathbf{x}'$  and considering only small perturbations, so that  $\mathbf{x} \approx \mathbf{x}'$  and  $\mathbf{F}(\mathbf{x}') \approx \mathbf{F}(\mathbf{x}) + \mathbf{J}(\mathbf{x})(\mathbf{x}' - \mathbf{x})$  the equation can be approximated by

$$\dot{\mathbf{x}}_\perp = \mathbf{F}(\mathbf{x}) - \mathbf{F}(\mathbf{x}') - \mathbf{K}(\mathbf{x}_\perp) \approx \mathbf{J}(\mathbf{x})\mathbf{x}_\perp - \mathbf{K}(\mathbf{x}_\perp),\tag{4.21}$$

where  $\mathbf{J}(\mathbf{x})$  is the Jacobian matrix of  $\mathbf{F}$  evaluated on the synchronization manifold. A linearisation of the function  $\mathbf{K}(\mathbf{x})$  around zero, where we assume that  $\mathbf{K}(\mathbf{0}) = \mathbf{0}$  and neglect higher order terms of  $\mathbf{x}_\perp$ , leads to

$$\dot{\mathbf{x}}_\perp \approx (\mathbf{J}(\mathbf{x}) - \tilde{\mathbf{K}})\mathbf{x}_\perp,\tag{4.22}$$

with

$$\tilde{\mathbf{K}} = \left. \frac{d\mathbf{K}}{d\mathbf{x}} \right|_{\mathbf{x}=\mathbf{0}}.\tag{4.23}$$

In our case, where we have linear coupling, the matrix  $\tilde{\mathbf{K}}$  is

$$\tilde{\mathbf{K}} = \begin{pmatrix} 0 & 0 & 0 & 0 & 0 \\ 0 & 0 & 0 & \alpha & 0 \\ 0 & 0 & 0 & 0 & \alpha \\ 0 & 0 & 0 & 0 & 0 \\ 0 & 0 & 0 & 0 & 0 \end{pmatrix}. \quad (4.24)$$

To achieve complete synchronization, it is required that  $\mathbf{x}_\perp$  goes to zero for  $t \rightarrow \infty$ . From the linearised Eq. (4.22) one would expect that the two systems will synchronize if the transverse Lyapunov exponents, that are the Lyapunov exponents associated with Eq. (4.22), are all negative. This criterion was first proposed by Fujisaka and Yamada (1983), but in contrast to this, e.g. Gauthier and Bienfang (1996) observe only incomplete synchronization in their model instead of the proposed full synchronization, when the largest transverse Lyapunov exponent is smaller than zero. Several criteria for synchronization were developed (Blakely et al. 2000), but it was also shown there that for their model none of these criteria exactly predicts the range of the control parameter, where full synchronization can be observed.

In our case the largest transverse Lyapunov exponent is positive with  $\lambda_\perp \approx 0.084$  but we also observe partial synchronization. The time  $t^*$  after which all information is lost and the two trajectories are totally independent, reads

$$t^* \approx \frac{1}{\lambda} \ln \frac{L}{\delta x(0)}, \quad (4.25)$$

where  $\lambda$  is the Lyapunov exponent,  $L$  denotes the characteristic length of the attractor and  $\delta x(0)$  the error that cannot be dissolved by a given accuracy (Argyris et al. 1995). Here  $t^*$  is found to be about 1.3 years. Nevertheless locking can be observed over much longer timescales, as can be deduced from Fig. 4.11. This demonstrates that in the period of locking, a non-average, non-standard situation is present. Below we will link it to phase-space structures of low measure, yet of a noticeable domain of attraction.

#### 4.4 Analysis of forced versus coupled setup

In this section we systematically compare the coupled system to the forced one with respect to time series properties as well as phase space topology. As a necessary condition for the forced system to emulate the coupled one in the time-domain we require that the forced system shows locking if and only if its coupled counterpart does. As a first step we will analyse again the mean locking time  $\langle \tau \rangle$  where locking is defined as in Eq. 4.9, when

$$S_{lock} = \frac{|\mathbf{x} - \mathbf{x}'|}{\sigma(\mathbf{x})} < \epsilon, \quad (4.26)$$

where in this case locking is required in all three atmospheric variables  $(x, y, z)$ . For a proper choice of the threshold  $\epsilon$  see below, here we took  $\epsilon = 0.01$ .

#### 4.4.1 System without seasonal cycle

An important structural difference between coupled and forced systems will be discussed in this section. In order to separate the two forcing effects in this model, namely the ocean forcing through the variables  $p$  and  $q$  and the seasonal forcing, the model is at first investigated without the seasonal cycle. We analyse the dependence of the mean locking time  $\langle \tau \rangle$  on the coupling strength  $\alpha$  (cf. Fig. 4.12a).

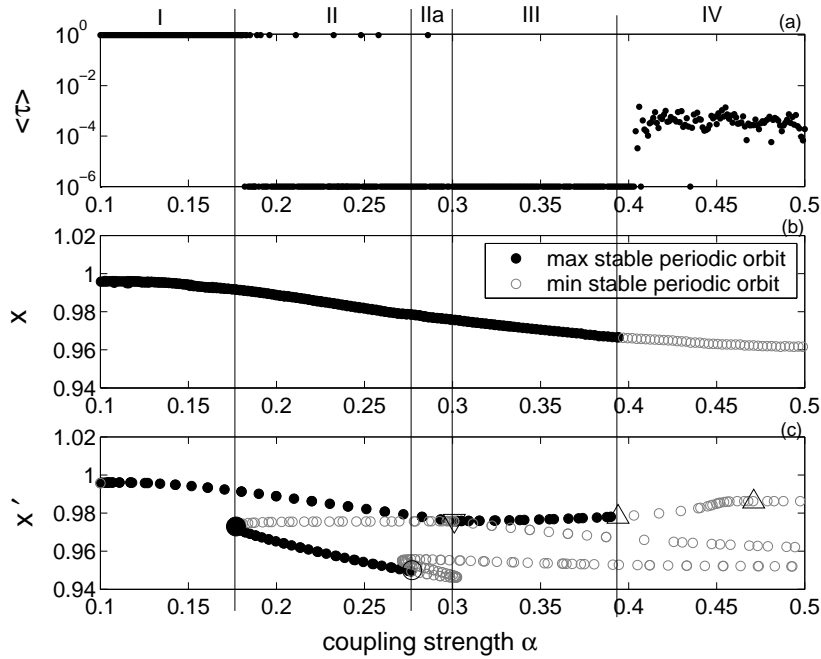


Figure 4.12: Mean locking time in relation to the most dominant invariant sets (periodic orbits) for the system without seasonal cycle (with  $a=0.12$ ). (a) Mean locking time  $\langle \tau \rangle$  in dependence on the coupling strength  $\alpha$ . A mean locking time of  $\langle \tau \rangle = 1$  refers to locking over the whole run (=100%). As a mean length of zero cannot be depicted in a logarithmic plot, we added an offset of  $10^{-6}$ . For every point in this figure the initial conditions for  $\mathbf{x}$  were chosen randomly and the trajectories were integrated over 500 years, according to 730,500 time steps, after they settled down on an attractor. The forced trajectory was started on the attractor with slightly perturbed initial conditions, chosen from a Gaussian distribution with a standard deviation of 0.01. For every value of the coupling strength  $\alpha$  the integration was performed several times; (b) Bifurcation diagram for the variable  $x$  of the five dimensional (5-D) driving system; for the periodic orbits, just one point referring to the maximum of the orbit is plotted; (c) Bifurcation diagram for the variable  $x'$  of the 8-D combined drive and response system. A filled circle symbol represents a saddle node bifurcation, an unfilled circle stands for a torus bifurcation, an upward-pointing triangle denotes a period doubling bifurcation and a downward-pointing triangle symbolizes a branch point. The different parameter regions I, II, IIa, III, and IV mark a qualitative different behaviour that is explained in the text.

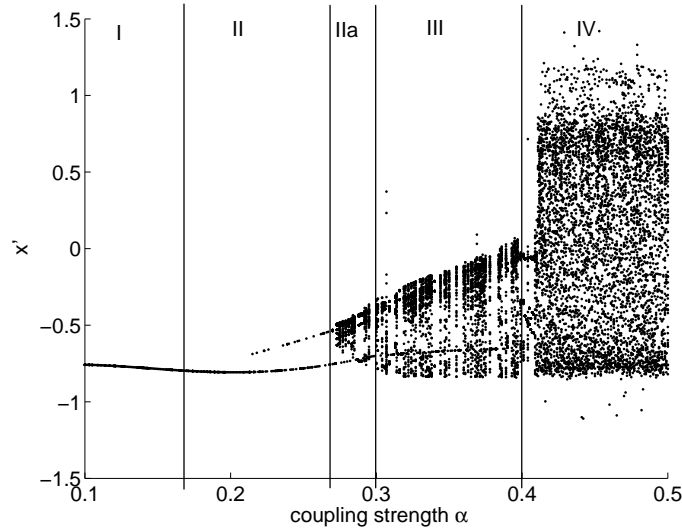


Figure 4.13: Bifurcation diagram for  $x'$  in dependence of the coupling strength  $\alpha$  in the system without seasonal cycle and  $a=0.12$ . The different parameter regions I, II, IIa, III, and IV mark a qualitative different behaviour that is explained in the text.

A significant difference can be observed in the mean locking time  $\langle \tau \rangle$  between a fully coupled run and a forced run. The fully coupled system consists of two totally independent systems  $x$  and  $x'$ , where the coupling matrix  $\tilde{\mathbf{K}}$  of Eq. (4.24) is zero. The forced system is the 8-D combined drive and response system, consisting of Eqs. (4.10)–(4.14) and (4.15)–(4.17), the Eqs. (4.18) and (4.19) are neglected in this case as they have no influence on the system's dynamics. Whereas the mean locking time  $\langle \tau \rangle$ , as a function of  $\alpha$ , is always zero in the fully coupled system (not plotted in the diagram), there are small parameter ranges in the forced system, where the trajectories always show locking (parameter region I in Fig. 4.12), or where locking never appears, e.g. in region III. Additionally, there are also regions in the forced system, where we observe intermittent synchronization (region IV) as shown in Fig. 4.11 – like in the original system which includes a seasonal cycle. This suggests that the seasonal forcing is not the main cause of the observed intermittent behaviour.

The result presented does not depend on the choice of the threshold  $\epsilon$ , provided that  $\epsilon$  is not too small. The relative mean locking time  $\langle \tau \rangle$  grows only slowly with  $\epsilon$ , so there would be only a slight shift for the value of  $\langle \tau \rangle$  in Fig. 4.12a. On the other hand it is important to choose a threshold  $\epsilon$  that is not too small (Lai 1996), because it then takes a long time until the trajectory falls below the threshold and therefore one would need very long runs to calculate a reliable value for the mean locking time  $\langle \tau \rangle$ .

In the remaining part of this section, we empirically correlate time series properties and phase-space topology in order to explain the locking phenomenon of the forced system. To get an impression of the phase space topology of the system in dependence on the parameter  $\alpha$ , a bifurcation analysis is performed with the bifurcation analysis program AUTO (Doedel 1981), that was already introduced in section 2.3.1. In Fig. 4.12b the bifurcation diagram for the variable  $x$  of the fully coupled system – which simultaneously

Table 4.1: Overview over the different regions in parameter space. SPO stands for stable periodic orbit, UPO for unstable periodic orbit.

parameter region in Fig. 4.12	coupling strength $\alpha \in$	$x$	$x'$	locking?
I	[0.1, 0.177]	SPO	SPO	locking
II	[0.177, 0.277]	SPO	two SPOs	locking, when $x$ and $x'$ are on the same PO; else no locking
IIa	[0.277, 0.3]	SPO	same SPO and torus	locking, when $x'$ is on the PO; no locking, when $x'$ is on the torus
III	[0.3, 0.4]	SPO	(differing) SPO and torus	no locking
IV	[0.4, 0.5]	UPO	UPOs	intermittent locking (on-off synchronization)

plays the role of the forced system's master trajectory – is plotted, in Fig. 4.12c the same is done for the variable  $x'$  of the 8-D combined drive and response system. Remember that for locking to occur,  $x$  and  $x'$  must coincide in the time series. In region I (for  $\alpha < 0.177$ ) both diagrams display the identical bifurcation diagram that simply consists of one stable periodic orbit. We propose that locking occurs in the forced system if both the master and the perturbed trajectory end up on the same periodic orbit.

For  $\alpha > 0.177$ , the difference of the bifurcation diagrams is amazing: while for any  $\alpha < 0.4$  a stable periodic orbit exists in both the coupled (Fig. 4.12b) and the forced system (Fig. 4.12c), this orbit either lives on a different branch (region III) or another stable periodic orbit coexists (region II), born in a saddle node bifurcation at  $\alpha = 0.177$ . In the latter situation, full synchronization can be observed if the perturbed trajectory starts in the domain of attraction of that periodic orbit which mimics the orbit of the master system (upper branch); otherwise the perturbed trajectory gets trapped by the concurring periodic orbit (lower branch) and locking never occurs. In the former case (region III), the attracting orbits differ, hence synchronization should be impossible. This is in fact consistent with the mean locking time observed in Fig. 4.12a.

In Fig. 4.13 another bifurcation diagram for  $x'$  is obtained by numerical integration to capture the movement on a torus, that cannot be depicted in the other diagram. In fact, the torus bifurcation is found in the upper Fig. 4.12c for  $\alpha = 0.277$ , but the torus cannot be followed with this method. For each parameter value  $\alpha$  we let the system settle down to an attractor and then plot the forced variable  $x'$ , when the trajectory crosses the  $y'$  axis at 0.5. We can again identify the five qualitatively different parameter regions. From left to right we first observe the stable periodic orbit and at  $\alpha = 0.177$  the generation of a second orbit. From these stable periodic orbits a quasi-periodic motion on a torus emerges at  $\alpha = 0.277$ . The dynamics on the torus is sometimes interrupted by the stable



periodic orbit that can be found in Fig. 4.12c, region IIa. The torus disappears at  $\alpha=0.4$  through a period doubling bifurcation and passes into chaotic motion. For the driving system  $\mathbf{x}$  no quasi-periodic dynamics are found, so that for  $\alpha$  in region IIa, before the branch point at  $\alpha=0.3$  emerges, the system shows locking when  $\mathbf{x}'$  is on the stable limit cycle or shows no locking when  $\mathbf{x}'$  is on the torus. Which state will be adopted depends on the initial conditions. For  $\alpha$  larger than the bifurcation value  $\alpha=0.3$ , there is scarcely any locking because the forced system is on the torus and the fully coupled system on the stable periodic orbit. An overview of the different classifications in dependence on the parameter space is given in Table 4.1.

So far we can conclude that if the system is on the same stable periodic orbit for  $\mathbf{x}$  and  $\mathbf{x}'$ , we get full synchronization. On the other hand, when  $\mathbf{x}$  runs on a periodic orbit not concurring to the replicate of  $\mathbf{x}'$ 's periodic orbit, locking cannot be observed. That means there can be intrinsic obstacles for a forced system not to perform as the fully coupled system. For modelling issues this is a crucial outcome, as the calculation of the state space of the forced and the coupled model is very costly for more sophisticated models so there is hardly any way to decide if forcing is suitable, above all because the fully coupled model is usually not known. For users of forced models it is therefore of central importance to note that synchronization effects might be artefacts of the forced set-up.

In order to obtain a full understanding of the fundamental discrepancies between the forced and fully coupled system, we will focus on intermittent synchronization in the following. This phenomenon arises for  $\alpha>0.4$ , where no stable periodic orbit is detected.

#### 4.4.2 The role of (un)stable periodic orbits

From the observations in the previous section we can conclude that if the system is in a region, where it is on a stable periodic orbit, the forced system shows locking all the time, provided that we are in a region in parameter space where  $\mathbf{x}$  and  $\mathbf{x}'$  show the same bifurcation diagram. The argument is as follows: as the orbit of the 8-D system is stable, the trajectories of the driving system and the driven system end up on the same periodic orbit, but they could still have a phase shift. If there were a phase shift, then this shift would also be seen in the ocean coordinates. But this is excluded through the replica approach, where only the atmosphere coordinates are varied. Contrary to this, for the coupled system the ocean coordinates are also subject to the perturbation, hence no synchronizing drive is present and no locking will occur.

This emphasizes that full synchronization can in this case be explained by a stable periodic orbit (or a stable equilibrium point) that drives the forced system to the same dynamic behaviour.

After the stability has been lost in a bifurcation point, the unstable periodic orbit embedded into the attractor influences the system so that intermittently locking occurs even in a region, where the transversal Lyapunov exponent is positive and – naively, “on average” – no synchronization is expected. Therefore the concept of (unstable) periodic orbits seems to be crucial for the locking phenomenon and the loss of synchronization can be traced back to the transition from stable to unstable periodic orbits. Ott and Sommerer (1994) call this a “nonhysteretic” blowout bifurcation, where for  $a < a_c$  the system is on an

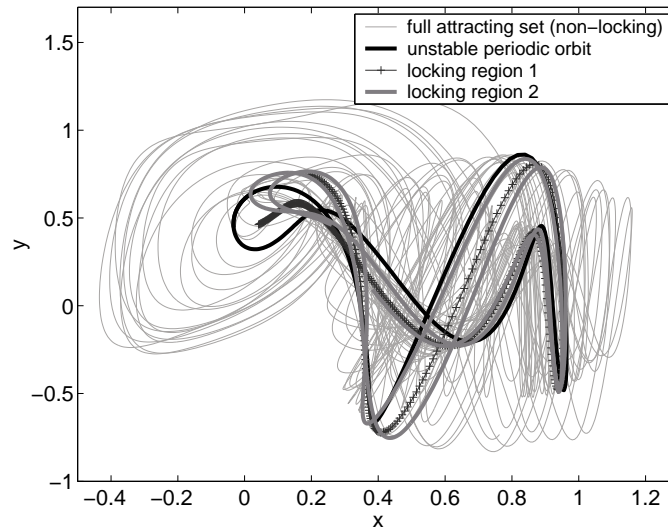


Figure 4.14: Phase space of the full attracting set (non-locking region) and of two exemplary locking regions (1 and 2), whereas here region refers to a period in time. For comparison the unstable periodic orbit for this parameter constellation is plotted.

attractor and for  $a > a_c$  on-off intermittency can be detected. The role of unstable periodic orbits (UPOs) for synchronization is also pointed out by Pazó et al. (2003) and by Pikovsky et al. (1997).

The interpretation with regard to UPOs can be stressed through Fig. 4.14, where we analysed the phase space of the locking regions in comparison to the full attracting set. It can clearly be seen that the locking region is in good coincidence with the unstable periodic orbit, whereas the non-locking region covers a much larger part of the whole phase space.

Just beyond a bifurcation point, where a periodic orbit has become unstable, the Monodromy matrix of the related mapping will display a long timescale on the unstable manifold, and generically shorter time-scales for the remaining stable manifold. Therefore, the unstable periodic orbit still has the opportunity to attract on the stable manifold and synchronize the trajectory. This will reveal itself as locking. After a while, the long timescale on the unstable manifold manifests itself, and the trajectory becomes repelled, reminiscent of intermittency. Hence, we suggest that intermittent locking can be traced back to a co-existence of two identical unstable periodic orbits, one in the fully coupled, and one in the combined 8D fully coupled and replica system.

In summary, there are two major differences in the coupled and the forced system's dynamics: first, the forced system displays a richer bifurcation diagram including coexisting stable invariant manifolds, where the coupled system would not ("artificial bistability"), and even if both the master and the perturbed trajectory would end up on the same periodic orbit, the coupled system lacks a synchronizer, hence cannot display locking.

One potential practical consequence could emerge within weather forecasting: if locking occurred already at the beginning of the dynamics, in the "forecast period", the ensemble error along the trajectory could be vastly underestimated in forced ensembles. This could imply e.g. that a hurricane could affect a region on its way much earlier than anticipated.

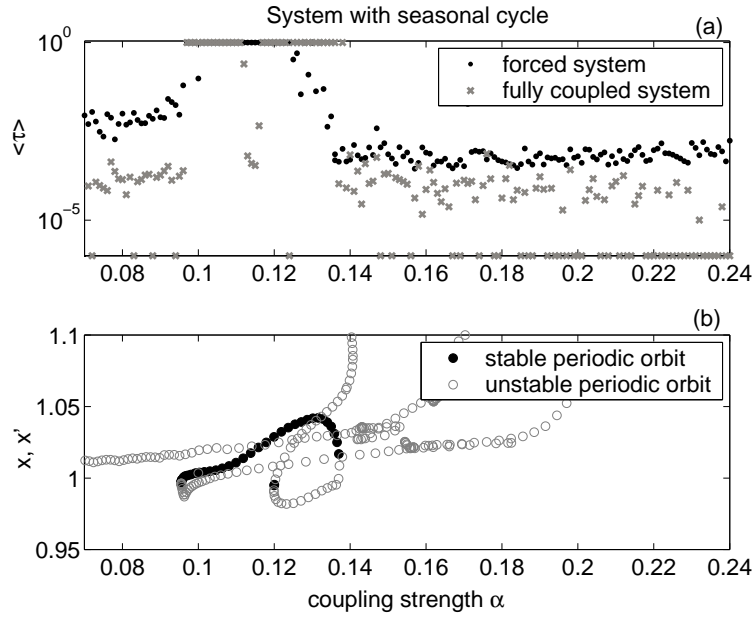


Figure 4.15: Variation of the coupling strength  $\alpha$  in the system with seasonal cycle with  $a=0.27$ . (a) Mean locking time  $\langle \tau \rangle$  in dependence on the coupling strength  $\alpha$ . Again we added an offset of  $10^{-6}$  to depict a mean length of zero; (b) Bifurcation diagram of the system. As for this parameter constellation  $x$  and  $x'$  show the same bifurcation diagram, just one bifurcation diagram is plotted.

Furthermore, artificial bistability could bring about that climate policy becomes overly conservative as society tries to prevent crossing a threshold which is just an artefact from the forced model set-up.

#### 4.4.3 System with seasonal cycle

The assertion of the role of stable and unstable periodic orbits can also be endorsed by Fig. 4.15, where the system with seasonal cycle in dependence on the coupling strength  $\alpha$  is analysed. As before, the bifurcation diagram and the mean locking time are plotted. Again we can detect intermittent synchronization and it can be seen that there is a transition from locking to intermittent locking.

Figure 4.15 makes it clear that the presumption that the two systems will synchronize with stronger coupling, is not valid in this case. The system needs a stable manifold to become fully synchronized. For modelling issues, this means that it does not depend on the strength of coupling but on the current position in phase space whether forcing can substitute coupling.

A significant difference to the situation without seasonal forcing is that here the fully coupled system shows locking when the system is on a stable limit cycle, see Fig. 4.15a, where the mean locking time is 1 in the locking regions, which means the system locks permanently. Intermittent synchronization can also be observed sometimes but less often than in the forced system (Fig. 4.15a). This is due to the seasonal forcing, that determines

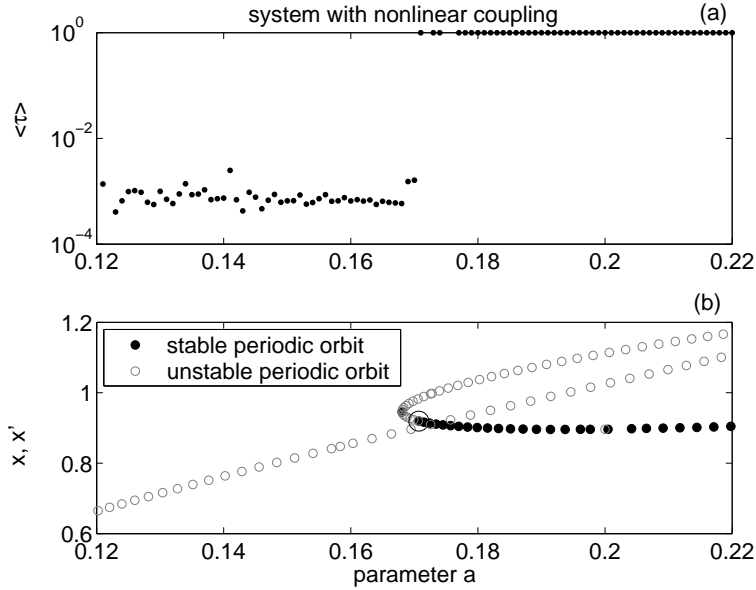


Figure 4.16: Influence of the parameter  $a$  in the system without seasonal cycle and with nonlinear coupling as described through Eqs. (4.27) and (4.28). (a) Mean locking time  $\langle \tau \rangle$  in dependence on the parameter  $a$ ; (b) Bifurcation diagram of the 5-D and the 8-D system. Here  $x$  and  $x'$  show the same bifurcation diagram. The unfilled cycle stands for a torus bifurcation.

the frequency of the periodic orbit. Therefore, this locking bears on an external forcing and not on the intrinsic phenomenon of locking through prescribed forcing by variables. But as the seasonal cycle is a kind of forcing as well, the probability of locking through an additional “synchronizer” increases.

#### 4.4.4 Influence of the type of coupling

The system analysed so far is a system with linear coupling. As this is a very special case of coupling that is not very common in truly coupled models, we analyse a system without a seasonal cycle and with a nonlinear coupling to determine the influence of the type of coupling. The coupling has the following form:

$$\dot{y} = xy - cy - bxz + G + \alpha p^3 x \quad (4.27)$$

$$\dot{z} = xz - cz + bxy + \alpha q^3 x, \quad (4.28)$$

instead of Eqs. (4.11) and (4.12). As  $p$  and  $q$  vary between -1 and 1 approximately, the introduced term bears strong nonlinearity.

Instead of analysing the influence of the coupling strength  $\alpha$ , we focus on the effect of varying the parameter  $a$  here. Again we have full locking when the system is on the same stable limit cycle for  $x$  and  $x'$ , and transitions to intermittent locking when an UPO is reached, see Fig. 4.16. By varying the coupling strength  $\alpha$  in a range from 0.0 to 0.65 we discover a region of artificial bistability for  $x'$  (not shown here) as we have seen before in

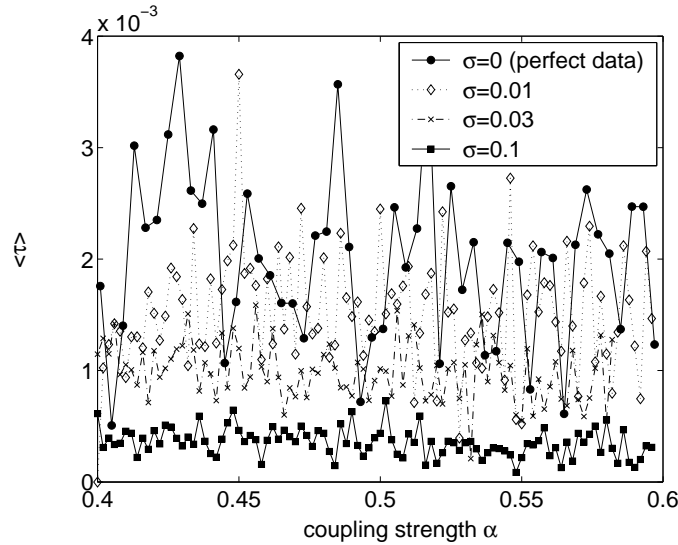


Figure 4.17: Influence of noise: mean locking time  $\langle \tau \rangle$  for the system without seasonal cycle (with  $a = 0.12$ ). Comparison of perfect data and noisy ocean data with different values for the standard deviation  $\sigma$  ( $\sigma = 0.01; 0.03; 0.1$ ) of the white noise  $\xi$  that is added to the ocean data. The corresponding bifurcation diagram for  $\sigma = 0$  is plotted in Fig. 4.12c. A mean locking time of  $\langle \tau \rangle = 1$  refers to locking over the whole run.

the system with linear coupling (Fig. 4.12).

We can conclude that all features found in the linear coupled system can also be discovered in the system with nonlinear coupling. This demonstrates that the type of coupling (linear or nonlinear) has no decisive influence on the locking phenomenon. Quite the contrary, as periodic orbits appear frequently in nonlinear systems, locking may occur generically in forced systems and is much less likely in their fully coupled counterparts. This stresses that for the locking phenomenon a linear stability analysis is not sufficient.

#### 4.4.5 Influence of noise and model uncertainties

In the above examination a “perfect data” scenario is adopted, implicitly stating that the ocean data is known exactly and can be used as input for studying atmospheric dynamics. The same holds for the atmosphere model itself, here the knowledge of a “perfect model” is assumed. To investigate the influence of erroneous data, a noisy term is added to the input forcing data. Instead of the ocean components  $p$  and  $q$ , the terms  $p + \xi$  and  $q + \xi$  are applied with different standard deviations  $\sigma$  for the white noise  $\xi$ , ranging from  $\sigma = 0.01$  to  $\sigma = 0.1$ , whereas the ocean components  $p$  and  $q$  are in the order of magnitude of 1. For this setting the length of the locking time  $\langle \tau \rangle$  is plotted in Fig. 4.17, together with the values for the “perfect data” from Fig. 4.12a.

As expected, the derived values for the mean length of the locking time are monotonously decreasing with amplitude of the noisy data. This effect can be attributed to the imperfect ocean data that brings about a marginal disturbance of the unstable periodic orbit in the forced system so that the accordance of both orbits falls off. Enhancing the noise up to

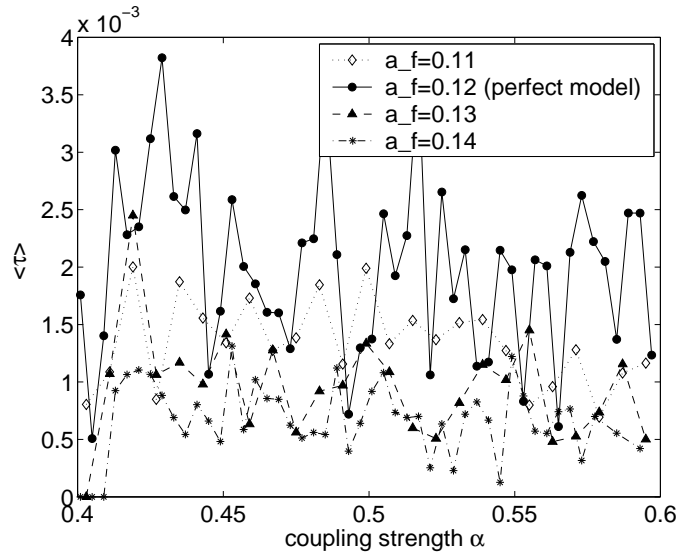


Figure 4.18: Influence of model errors: mean locking time  $\langle \tau \rangle$  for the system without seasonal cycle (with  $a_{\text{coupled}} = 0.12$  in Eq. (4.10)) in dependence on the coupling strength  $\alpha$  in relation to the detuning between perfect and imperfect model. Mean locking time for the “perfect data” scenario with  $a_{\text{forced}} = 0.12$  in Eq. 4.10 and for  $a_{\text{forced}} = 0.11, 0.13,$  and  $0.14$  in Eq. 4.15. A mean locking time of  $\langle \tau \rangle = 1$  refers to locking over the whole run.

a standard deviation  $\sigma = 0.1$  leads to much shorter locking times. On the other hand, a standard deviation  $\sigma = 0.01$  has only a marginal influence on the mean length of locking. Hence, it can be stated that locking is in certain ranges stable against the influence of noise and therefore a robust phenomenon.

The same holds for the implementation of model structure uncertainty instead of using a perfect model. For this setting, the parameter  $a$  was set to a slightly different value in the forced model, i.e.  $a_{\text{coupled}} = 0.12$  in Eq. (4.10) for the generation of the data and a perturbed parameter  $a_{\text{forced}} = 0.11, 0.13,$  and  $0.14,$  respectively, in Eq. (4.15) for the forced run<sup>6</sup>. The setting is comparable to the AMIP experiments (Gates et al. 1992; AMIP II 2006), where the “true” atmosphere cannot exactly be modelled, but is approximated by an unavoidably deficient model. In Fig. 4.18a the mean locking times for the perfect and the imperfect model are shown. When the forced and the coupled model disagree the values for  $\langle \tau \rangle$  decrease in comparison with the values for the “perfect model” scenario.

The consequences for GCM-modelling using observed SST data to force the atmospheric component are evident: if the real world system resides on an (un)stable manifold and if the atmosphere model is well designed – this means that the model does not differ too much from the real world – then the possibility is given that intermittent locking occurs. Moreover, the fact that locking is robust against uncertainty in data as well as against model uncertainty emphasises the above findings from the investigation of the GCM ensembles: the results will qualitatively not differ when we apply observational data to force the model instead of the “perfect data, perfect model” scenario.

<sup>6</sup>The value of  $a$  was only changed in front of  $x$ , but not in the forcing term  $F$ .

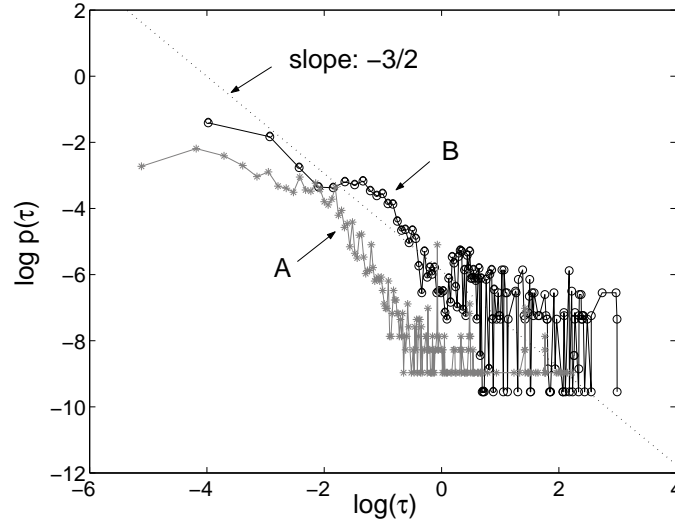


Figure 4.19: Probability distribution of the length of the locking region for more than 14,000 locking phases. Curve A is for a parameter setting as given following Eq. 4.14 with  $a = 0.125$ , for curve B the parameter  $a$  is changed to 0.075, being closer to the bifurcation. The dotted curve indicates a  $-3/2$  power-law for comparison.

## 4.5 On-off synchronization

The alternation between regions, where the error between the forced and coupled trajectory is nearly zero, and between regions with large bursts as shown in Fig. 4.11, resemble those of on-off intermittency. On-off intermittency, as introduced by Platt et al. (1993), refers to a situation where the variables of a chaotic dynamical system exhibit two distinct states where at the “off” state the system is nearly constant on an invariant manifold, and at the “on” state large bursts from these laminar phases occur. The frequency of bursts is controlled by a characteristic parameter  $p$  of the system and approaches zero, when the blowout bifurcation (Ott and Sommerer 1994) is reached as  $p$  attains a critical value  $p_c$ . To assign the phenomenon of on-off intermittency to our object of interest, intermittency is not seen as laminar phases interrupted by turbulent bursts but as locking of the fully coupled and the forced trajectories (off-state) interrupted by non-locking (on-state), which we will call *on-off synchronization* as a special case of on-off intermittency. The transfer from on-off intermittency to on-off synchronization becomes clearer when the difference between  $\mathbf{x}$  and  $\mathbf{x}'$  is understood as a new variable.

Systems that generate on-off intermittency show characteristic scaling laws for the intermittent phases (Heagy et al. 1994; Lai 1996), the distribution of the amplitudes of the bursts and for the power spectrum of the trajectories (see references cited by John et al. (2002)). Heagy et al. (1994) investigate a certain class of driven systems that consists of a discrete map and a random driving variable with a smooth density. They show that for the probability distribution of the length of the laminar phases  $p(T)$  a power law holds with  $p(T) \sim T^{-\gamma}$ , where  $T$  is the length of the laminar phases and  $\gamma$  the scaling exponent that attains a universal value of  $3/2$  in the vicinity of the threshold for on-off

intermittency.

This scaling law with the same exponent can also be approved for our case of on-off synchronization. The probability distribution  $p(\tau)$  for the length of the locking region  $\tau$  for the parameter settings given in Fig. 4.10 (with  $a = 0.125$ ) is plotted as curve A in Fig. 4.19. As the  $-3/2$  power-law distribution is deduced theoretically exactly only for the critical point  $a_c$ , we additionally plotted the probability distribution for  $a = 0.075$  in curve B. This choice of the parameter is very close to the bifurcation point from a stable to an unstable periodic orbit at  $a_c = 0.073$ , that was determined via bifurcation analysis.

As both curves indicate, the probability distribution obeys the predicted scaling law when the parameter  $a$  is close to the bifurcation point and differs from the exact relation when the parameter is further away from the critical value. For very short locking phases both curves deviate from the predicted dependence, because one approaches the time scale of the simulation time step. For long locking phases the distribution for curve A falls off exponentially, whereas the two regions are connected by a shoulder, which is also seen in other systems displaying on-off intermittency (Platt et al. 1993). We assume that these imperfections from the exact scaling law is due to the distance of the parameter  $a$  from the bifurcation point in our case.

In this section we have shown that the scaling law for the duration of the laminar phases in systems with on-off intermittency also holds for a system with on-off synchronization and could be extended to continuous systems with a driving system that is not random but chaotic. This implies that the power law scaling is more universal than proposed when it was introduced. It can also be interpreted in this respect, that the underlying mechanisms of on-off intermittency and on-off synchronization are analogous. Intermittency is often traced back to the “almost existence” of a stable periodic orbit, and in a similar way we discovered stable and unstable periodic orbits as potential causes for locking.

The knowledge of the above power law does not only stress the underlying nature of locking but will also help in applications to estimate the relative importance of the locking phenomenon.

## 4.6 Conclusions

In this chapter we have considered the effect of module coupling on the overall dynamical uncertainty to understand the inherent differences between a coupled and a forced set-up and which mechanism prevents their similarity. These associated uncertainties of this approach are found to be indeed intrinsic, i.e. irreducible and unavoidable, within the forced modelling paradigm. We have investigated the uncertainties by analysing an atmospheric GCM ensemble forced with SST data where we could show that the effect of forcing instead of coupling is not negligible and sometimes leads to an overestimation of predictability. Moreover, the ensemble spread, which is often used as a proxy for the predictability of the true coupled run, is shown to substantially disagree with the fully coupled reference run in some cases. Motivated by this empirical finding, we investigated a similar set-up for a paradigmatic non-linear atmosphere-ocean system that we can – in contrast to GCMs – investigate along the lines of dynamical systems theory.



On the one hand, in accordance with the underlying assumption of this approach, forced and coupled model version of this conceptual model coincide in various main features in most cases, in particular in terms of average predictive skill and the existence of the same dominant periodic orbit. On the other hand, we identified phase space features as well as time series features with respect to which a forced model set-up differs qualitatively from its fully coupled counterpart, for systematic reasons: the phase space of the fully coupled model is dominated by a single stable periodic orbit, while the forced set-up allows for the existence of an additional stable periodic orbit. Since this kind of bistability is not found in the fully coupled model, which the forced set-up is supposed to emulate, we call it “artificial bistability”. These findings seem to contradict conventional wisdom in the Earth System modelling community stating that a fully coupled model is a more complicated entity than a forced derivative, hence the coupled version is expected to display more complicated features. However, in terms of replica systems – a point of view we put forward in this chapter – we argue that in fact the forced set-up is the more complex one: its dynamics are generated in an eight-dimensional (ocean-dimension plus two times the atmosphere-dimension) state space, while that of the coupled version resides in a five-dimensional space.

Furthermore, the systematic discrepancies of the two approaches in modelling extend into the time-domain. At least intermittently the forced set-up displays artificial predictive skill. This is a direct consequence of the replica-nature of the forced set-up: we have perturbed the coordinates of the replica atmosphere in order to determine the predictive skill. As the perturbation cannot propagate to the five-dimensional sub-system driving the replica atmosphere, this five-dimensional sub-system potentially serves as a synchronizer. In case the replica atmosphere (“slave”) and the synchronizer (“master”) run in the vicinity of an identical periodic orbit which possesses a stable manifold, the ensemble will tend to collapse onto the master trajectory. Hence, we identified the observed locking phenomenon in the conceptual model as an almost-collapse to a periodic orbit. If the orbit is stable, locking will continue forever. If the orbit is unstable, the time-scale of locking is set by the competition of the stable and the unstable manifold of the periodic orbit, giving rise to intermittent locking. We have observed a power law for the distribution of locking duration, which allows estimating the probability of locking to occur. Due to the phenomenological analogy to on-off intermittency, we call intermittent locking “on-off synchronization”. In any case, locking implies artificial predictive skill, which we explain by the existence of a partially attracting invariant set. For weather forecasting this could imply that the ensemble error on the particular time, when a – potentially extreme – weather pattern such as a hurricane will hit a certain region, can become extremely underestimated with a forced set-up; hence an endangered region may prepare too late.

All analysed features can be observed in the conceptual model for the original system with seasonal forcing and linear coupling, in the system without seasonal forcing, and in the system with nonlinear coupling. Furthermore the phenomenon of locking is robust against errors in data or in models, provided that the aberration from the “perfect” setting is not too large. Moreover, we found empirically the different phenomena of locking, intermittent locking, and absence of locking in the forced GCM ensemble as well. This emphasises that

predictability studies with purely forced models have to be regarded with care.

As the phase space topology for such high dimensional models can hardly be deduced we can only suspect that the underlying mechanism is the same as in the conceptual model. On the other hand, as we are able to explain these empirical findings with a universal theoretical pattern the ingredients of which just draw on the nonlinearity of the system, we suggest that on-off synchronization and artificial bistability are a general characteristic of forced systems rather than being restricted to this particular model set-up. While we expect that bifurcation analysis will be too demanding as a standard procedure for GCMs over the next years – although there had been quite a progress (Dijkstra 2005) –, nevertheless we advise that at least it is checked carefully with alternative model versions whether intermittent predictability and also bistability could not be the result of a forced – instead of the full-fledged coupled – set-up.

## 4.7 Synergy

In chapter 3 we have analysed the influence of ENSO on the Indian monsoon and have drawn conclusions from forcing the monsoon model with ENSO data. By contrast, in this chapter the concept of forcing instead of coupling was questioned and fundamental differences of both approaches were pointed out. Hence, this finding raises the question, whether the forced set-up concerning the ENSO-monsoon relationship leads to equivocal results. In fact, in this case the effect of forcing instead of coupling has no influence on the predictability, as we will argue in the following.

We will analyse the situation by considering the qualitative different regimes depicted in Fig. 4.12 that illustrate a general characteristic of forced systems. In accordance to the analysis of the forced atmosphere-ocean system, we apply different initial conditions for the monsoon model under ENSO forcing and can reproduce the simulated time series of Fig. 3.1c exactly. Thus we have a situation where all forced trajectories lock on one single trajectory and we can exclude that intermittent locking is existent, as is on hand in region IV of Fig. 4.12. Moreover, from Fig. 3.1c it is obvious that artificial bistability or an artificial stable state (cf. region II and III of Fig. 4.12) is not present as in this situation we would not see a coincidence of the observed and the simulated monsoon rainfall time series at all. This leads to the conclusion, that the forced monsoon model resides in region I (cf. Fig. 4.12), where forced and coupled (or truly forced) system coincide. The fact that the two trajectories are not in total agreement is due to model errors in the monsoon model.

Two further conclusions can be drawn: we *cannot* infer from this analysis, whether the ENSO-monsoon system constitutes a fully coupled one or whether the monsoon system is truly forced by ENSO. On the other hand, the results of the investigation accomplished to identify the link how ENSO influences the monsoon system hold for a potentially coupled as well as for a forced system. Although a fully coupled model is not needed to identify the link, such a model is desired to gain a better understanding of the physical processes, as some studies provide evidence that the Indian monsoon is indeed influencing ENSO (Ju and Slingo 1995; Wu and Kirtman 2003, e.g.).

## Chapter 5

# Summary and Conclusions

In this thesis we have explored four types of uncertainty, which are all fundamental in Earth System modelling, ranging from uncertainty in parameters and parameterisations over uncertainty about external forcings to uncertainty about the coupling between sub-modules. We have derived qualitatively new insights with regard to methods, identified intrinsic uncertainties and adopted this knowledge to the Indian monsoon system as a trendsetting field of climate research. The monsoon system constitutes an interdisciplinary challenge and a high relevance at the interface of non-linear dynamics, climate research, and policy advice.

The main achievements can be summarised on two levels: specific conclusions about uncertainties in a model of the Indian monsoon and general conclusions about uncertainties in Earth System modelling that are applicable to many other models.

- The model-specific results are:
  - ◇ The bifurcation in a box model of the Indian summer monsoon, which entails a regime shift from a wet to a dry monsoon regime, is robust against parameter uncertainties but not structurally stable against all considered uncertainties in the parameterisation of physical processes.
  - ◇ The combination of a conceptual model of the Indian monsoon with an observed time series of ENSO leads to the identification of one physical process that may be key in linking ENSO and the Indian monsoon and that allows reproducing the observed monsoon rainfall time series.
- The general results are:
  - ◇ A novel method is developed for testing the robustness of a bifurcation point by incorporating model parameter uncertainty, which is based on combining two standard approaches, i.e. bifurcation analysis and multi-parameter ensemble simulations.
  - ◇ Intrinsic (i.e. irreducible and unavoidable) constraints are identified that prevent the consistency of a forced model with its fully coupled counterpart. The discovered phenomenon of artificial predictability and bistability in a forced versus a fully coupled system seems to be a general characteristic of forced systems.

## 5.1 Uncertainty in parameters and parameterisations in a model of the Indian monsoon

The investigation of uncertainties in a model of the Indian summer monsoon was motivated by our finding of a saddle node bifurcation in this model (Zickfeld et al. 2005). This bifurcation brings about a regime shift from a wet to a dry monsoon that possibly has triggered abrupt changes in the past and could be of great concern to India's population under global environmental change. The uncertainty analysis of this bifurcation point is twofold with respect to the subject of investigation. On the one hand, those uncertainties are considered that are purely related to parameters, on the other hand, the uncertainties concerning the implemented processes and their parameterisations in the model are investigated.

The parameter uncertainties are investigated with the ensemble simulation method described below. The uncertainties in the model structure are analysed in a systematic procedure, where parameters are replaced step-by-step by functional relationships (parameterisations) leading to a number of model versions with a hierarchy in complexity. The result of this cumulative uncertainty analysis is that the model is robust against parameter uncertainty, but not structurally stable against all considered processes.

Although the bifurcation point is preserved in more than 94% of all considered parameter settings, the propagation of parameter uncertainties through the model leads to a broad uncertainty range for the position of the bifurcation point. This makes it difficult to estimate the relevance of this bifurcation for the current climate. On the other hand, the uncertainty that is related to the incorporated processes leads to a vanishing of the bifurcation in the model, giving rise to the conclusion that – at least in this model – structural uncertainties seem to be more influential than parametric ones. If this is a general characteristic, a conclusion that has to be tested more carefully, this will imply a strong need for the investigation of uncertainties in parameterisations in general circulation models (GCMs), going beyond those related to parameters.

## 5.2 Uncertainty of external forcing in a model of the Indian monsoon

With the box model of the Indian monsoon we have identified one key mechanism linking the Indian monsoon and ENSO. The conceptual model appeared to be highly suitable for such a study as it allows separating the different physical mechanisms of how ENSO and monsoon could interact. By coupling these two key climate constituents through the zonal trade winds we could reproduce large parts of the observed time series of the Indian summer monsoon rainfall. As we can also satisfactorily simulate the monsoon rainfall as inferred from the ECHAM5 and the HadCM3 model, we suggest that this link is the dominant physical mechanism in these two GCMs as well. Moreover, this shows that our monsoon model could serve as an emulator for these two GCMs in terms of the influence of ENSO on the monsoon. The analysis of the GCM results under climate change gives rise to the conclusion that the mechanism between ENSO and the Indian monsoon is not

changing, but that other influences, like the warming over the oceans or over the Tibetan Plateau, will alter the ENSO-monsoon relationship in the future.

### 5.3 Multi-parameter uncertainty analysis of a bifurcation point

For the uncertainty analysis of a bifurcation point we presented a novel method by combining a bifurcation analysis with a common sensitivity and uncertainty analysis in the high dimensional parameter space. This approach builds on an ensemble simulation environment, which provides the possibility to sample the whole parameter space according to deterministic or Monte Carlo methods, depending on the goal of the sensitivity experiment. The combination of a multi-run tool with common bifurcation analysis software allows testing the robustness of a bifurcation point against parameter uncertainties. Whereas in our case the bifurcation point is known and the robustness of this point against parameter uncertainties is tested, this method can also be applied to scan the entire parameter space to detect critical thresholds in Earth System models.

To the best of our knowledge such a systematic analysis of a bifurcation point has not been performed before. As this method is model-independent, it can be applied to the variety of models of similar complexity. A prominent example could be the thermohaline circulation (THC), where many models indicate a possible regime shift from an “on-state” to an “off-state”, but differ greatly in the exact position of this bifurcation in relation to the present day value (Rahmstorf et al. 2005).

### 5.4 Intrinsic uncertainty of model coupling

Since the currently preferred strategy for simulating the climate system, or more generally the Earth System, is the coupling of sub-system modules (representing, e.g., atmosphere, oceans, global vegetation), we performed an in-depth analysis of the bias and indeterminacies generated by the coupling procedure. The focus was on a comparison of forced dynamics, where one of the modules is replaced by prescribed data, as opposed to fully coupled dynamics in a conceptual atmosphere-ocean model as well as in a state-of-the-art GCM.

The study shows that the forced model cannot always emulate the fully coupled equivalent. While the coupled and the forced version of the conceptual model display identical features for most parameter settings, such as the existence of the same stable manifolds, there is also a considerable fraction of parameter- and state space, where qualitative discrepancies between the two modelling approaches are evident. For the forced version, the bifurcation diagram reveals artificial bistability and the time series display artificial predictive skill, which can solely be observed in the forced and not in the fully coupled “true” system. An intermittent version of this phenomenon is observed, which is denoted as on-off synchronisation – following the concept of on-off intermittency –, and that is traced back to the appearance of unstable periodic orbits. A scaling law governs this phenomenon, which allows the estimation of the probability of artificial predictive skill.

The discovered phenomenon of artificial predictability and bistability seems to be a general characteristic of forced systems and is not restricted to the analysed system. Our explanation pattern suggests that the unrealistic features appear generically in non-linear forced set-ups, as the key constituents for this mechanism are just based upon the non-linearity of the system. The fact that most properties can be observed in a forced versus a coupled set-up of a GCM as well supports the hypothesis of a generalisation of this finding. Moreover this is a crucial point when interpreting the results of forced GCM runs, which are often realised by forcing an atmospheric GCM with observational sea surface temperature data. The consequence of such a set-up is that predictability can be largely overestimated. On the other hand, in truly forced systems, there may exist a region in phase space where predictability is very high.

Concerning modelling issues, it is a fundamental finding that one must carefully check whether forcing instead of coupling is a tolerable simplification for the model under investigation. The results suggest that bistability and intermittent predictability, when found in a forced model set-up, should always be cross-validated with alternative coupling designs before being taken for granted.

## 5.5 Outlook and final remarks

The results of this thesis highlight the importance of considering qualitatively different types of uncertainty in the modelling process. Although we have to deal with an overwhelming number of uncertainties in Earth System modelling, some general characteristics and methods of how to deal with these uncertainties could be presented in this thesis. As a highly relevant example of climate research we have investigated uncertainties in a model of the Indian monsoon.

We have demonstrated that besides large uncertainties in the monsoon model, the application of a new method provides an informative basis for concluding that the bifurcation point with its regime transition in the model of the Indian monsoon is indeed relevant for today's climate regime. In particular, this is underlined by the robust occurrence of the bifurcation point and the wide uncertainty range for the position of the regime transition. For the application in terms of the integrated assessment some additional steps have to be performed: although our model includes most of the relevant physical processes, the embedding of some global scale factors is not taken into account, e.g the lateral and the transversal monsoon<sup>1</sup>. Moreover, the inclusion of the synoptic scale processes have to be considered. For including global and regional factors resulting in a better estimate for the present day climate and the distance from the bifurcation point, another potential step could be to analyse the monsoon system in a GCM or a model of intermediate complexity (EMIC). As our studies about structural uncertainties suggest, GCMs will most probably not show the bifurcation, but at least a dramatic decline of precipitation will be visible. Therefore it is important to check to what extent the determining processes are represented in GCMs. The combination of GCM results giving a more accurate estimate of

---

<sup>1</sup>The lateral monsoon refers to a cross-equatorial circulation of the monsoon, the transverse to longitudinal temperature gradients and their associated circulations.

the position of the bifurcation point in consideration of today's value with the in-depth parameter uncertainty study in the conceptual model could provide further evidence for the relevance of this bifurcation. These improvements have to be achieved resulting in more reliable conclusions for policy advice and the integrated assessment of the Indian monsoon.

In addition, it is indispensable to extend the model to be able to analyse not only the uni-directional influence of the external factors like ENSO on the monsoon but to include the full feedback chain of the coupled ENSO-monsoon system. This suggests the need to incorporate the internal monsoon dynamics and to embrace other factors than ENSO, such as the Quasi-Biennial Oscillation (QBO).

The conclusion that uncertainties in the parameterisations of the considered processes – as opposed to parametric uncertainties – seem to play a major role, should be investigated further. A support of this hypothesis could imply the strong need to investigate process or structural uncertainties, e.g. in studies concerning the *climate sensitivity* of models. Nonetheless, general statements concerning this issue will hardly be possible.

To underline the intrinsic differences of forced and coupled set-up and to achieve the possibility of estimating the quality of GCM predictions within a forced modelling approach, the method of path-following a coupled versus a forced set-up should be applied for a GCM as well. The goal is to reproduce the close relationship between time series properties and phase space topology for the forced version similarly as derived for the conceptual atmosphere-ocean model. Numerical techniques for path following are available (Dijkstra 2005) and could be applied for this kind of analysis.

All in this, this thesis has contributed to the fundamental issue of dealing with uncertainties the climate modelling community is confronted with. A novel method for systematically approaching uncertainties in parameters and parameterisations was presented. We have highlighted the whole chain of uncertainties ranging from parameter uncertainties to structural uncertainties demonstrated for a model of the Indian monsoon. Although some uncertainties allow for including them in the interpretation of the model results, intrinsic uncertainties were identified, which are inevitable within a certain modelling paradigm and are provoked by the specific modelling approach. We suggest that our findings should significantly contribute to a scheme for best-practice of dealing with structural uncertainty.





# Appendix A

## Variables and parameters of the monsoon model

### A.1 Variables

Table A.1: Prognostic and diagnostic variables of the monsoon model (Eq. 2.1-2.4).

name	description	unit
<i>prognostic variables</i>		
$q_a$	near-surface specific humidity	$\text{kg m}^{-3} \text{s}^{-1}$
$T_a$	near-surface air temperature	K
$w_1$	soil moisture of upper soil layer	1
$w_2$	soil moisture of lower soil layer	1
<i>diagnostic variables</i>		
$Ad_T$	advection of heat	$\text{W m}^{-2}$
$Ad_v$	advection of moisture	$\text{kg m}^{-2} \text{s}^{-1}$
$A_{sys}$	planetary albedo at the top of the atmosphere	1
$C$	condensation rate	$\text{kg m}^{-2} \text{s}^{-1}$
$c_s$	specific heat capacity of water per unit volume	$\text{J m}^{-3} \text{K}^{-1}$
$E$	evapotranspiration	$\text{kg m}^{-2} \text{s}^{-1}$
$F_{\uparrow}^{LW,TA}$	outgoing longwave radiation at the top of the atmosphere	$\text{W m}^{-2}$
$F_{\downarrow}^{SL,TA}$	incident solar radiation at the top of the atmosphere	$\text{W m}^{-2}$
$\theta$	potential temperature	K
$P$	precipitation	$\text{kg m}^{-2} \text{s}^{-1}$
$R$	runoff	$\text{kg m}^{-2} \text{s}^{-1}$

## A.2 Parameters

	Parameter	Value	Unit
	<i>physical constants</i>		
$c_p$	specific heat of air at constant pressure	1000	$\text{J kg}^{-1} \text{K}^{-1}$
$g$	gravity constant	9.81	$\text{m s}^{-2}$
$I_0$	solar constant	1365	$\text{W m}^{-2}$
$\mathcal{L}$	latent heat of evaporation	$2.5 \cdot 10^6$	$\text{J kg}^{-1}$
	<i>other parameters</i>		
$A_{00}$	parameter of Budyko formula	231	$\text{W m}^{-2}$
$a_1$	stratus cloudiness parameter	0.8	1
$a_2$	stratus cloudiness parameter	0.1	1
$a_3$	stratus cloudiness parameter	$1 \cdot 10^{-3}$	$\text{m s}^{-1}$
$a_q$	lapse rate coefficient	$1 \cdot 10^3$	$\text{kg}^2 \text{kg}^{-2}$
$a_v$	coefficient for determination of $V$	$9 \cdot 10^9$	$\text{s}^2 \text{m}^4 \text{kg}^{-2}$
$B_{00}$	parameter of Budyko formula	2.1	$\text{W m}^{-2} \text{K}^{-1}$
$b_1$	cumulus cloudiness parameter	$1.5 \cdot 10^{-3}$	$\text{m s}^{-1}$
$b_2$	cumulus cloudiness parameter	$30 \cdot 10^{-3}$	$\text{kg kg}^{-1}$
$b_{cl}$	albedo of the semi-infinite cloud at $\xi = 0$	0.0475	1
$b_{cs}$	clear-sky albedo at $\xi = 0$	0.05	1
$C_k^1$	constant for determination of $K$ for $w > 0$	5	1
$C_k^2$	constant for determination of $K$ for $w < 0$	1.5	1
$C_h^1$	constant for determination of $h$ for $w > 0$	4	1
$C_h^2$	constant for determination of $h$ for $w < 0$	0.4	1
$C_{00}$	parameter of Budyko formula	59	$\text{W m}^{-2}$
$D_{00}$	parameter of Budyko formula	0.65	$\text{W m}^{-2} \text{K}^{-1}$
$\eta$	$\text{CO}_2$ sensitivity parameter	0.04	1
$f_1$	field capacity of upper soil layer	24	$\text{kg m}^{-2}$
$f_2$	field capacity of lower soil layer	120	$\text{kg m}^{-2}$
$\Gamma_0$	lapse rate coefficient	$6 \cdot 10^{-3}$	$\text{K m}^{-1}$
$\Gamma_1$	lapse rate coefficient	$5.5 \cdot 10^{-5}$	$\text{m}^{-1}$
$\Gamma_2$	lapse rate coefficient	$1 \cdot 10^{-3}$	$\text{K m}^{-1}$
$\Gamma_a$	dry adiabatic lapse rate	$9.8 \cdot 10^{-3}$	$\text{K m}^{-1}$
$g$	gravity constant	9.81	$\text{m s}^{-2}$
$H_a$	height of the atmosphere	$30 \cdot 10^3$	m
$H_e$	specific humidity scale height	$2 \cdot 10^3$	m
$H_t$	height of the troposphere	$14 \cdot 10^3$	m
$h_s$	damping depth of thermal wave in soil layer	4	m
$K_r$	runoff parameter	0.4	1
$k_\tau$	cloud albedo parameter	2/3	1
$L$	box width	$1.5 \cdot 10^6$	m
$m_{cl}$	cloud albedo parameter	0.82	1
$m_{cs}$	clear-sky albedo parameter	1	1
	Parameter (continued)	Value	Unit
$N_{cu}^0$	reference cumulus cloud amount	0.7	1
$p\text{CO}_2^0$	reference $\text{CO}_2$ concentration	325	ppm

$pCO_2$	present-day volume concentration of $CO_2$	360	ppm
$P_{cr}$	critical precipitation for determination of $V$	$3.5 \cdot 10^3$	$kg\ m^{-2}\ s^{-1}$
$p_{cl}$	integral transmission function in cloudy atmosphere	0.97	1
$p_{cs}$	integral transmission function in clear-sky atmosphere	0.8	1
$\rho_0$	reference air density	1.29	$kg\ m^{-3}$
$\tau_0$	characteristic precipitation time	$5 \cdot 10^5$	s
$\tau$	soil moisture diffusion specific time	$17.28 \cdot 10^4$	s
$\tau_{st}$	optical thickness of stratus clouds	7.5	1
$\tau_{cu}$	optical thickness of cumulus clouds	25	1
$u_{mean}$	mean zonal wind velocity at $h$	2.4	$m\ s^{-1}$
$\phi_0$	mean latitude of India	20	$^{\circ}N$
$z_s$	surface layer height	20	m
$z_0$	roughness length of vegetated soil	0.1	m
<i>boundary conditions (for summer)</i>			
$f_{oc}$	relative humidity over the ocean	0.85	1
$T_{oc}$	ocean temperature	300	K
$N_{oc}$	cloud cover over the ocean	0.8	1

Table A.2: Physical constants and parameters of the monsoon model, reference values for the multi-parameter analysis in section 2.5, and boundary conditions for the model investigated in chapter 3.

## Appendix B

### Constants for the normal form

$$C_{AdT} = -c_p \frac{1}{L} \rho_0 H_0 C_{um0} \left( \exp\left(-\frac{h}{H_0}\right) - 1 \right) \quad (\text{B.1})$$

$$C_{Adv} = -\frac{1}{L} \rho_0 H_e C_{um0} (q_{oc} c_{f,2} - q_{a,const} c_{f,1}) \quad (\text{B.2})$$

$$C_\gamma = -(\Gamma_0 - \Gamma_a) z_{eff,1} + (\Gamma_0 - \Gamma_a) z_{eff,2} \quad (\text{B.3})$$

$$C_{um0} = \frac{\sin(\alpha_0) g p_0 H_t}{\rho_0 f R T_0^2 L_m} \quad (\text{B.4})$$

$$z_{eff,1} = H_0 + \frac{h \exp\left(-\frac{h}{H_{00}}\right)}{\left(\exp\left(-\frac{h}{H_{00}}\right) - 1\right)} \quad (\text{B.5})$$

$$z_{eff,2} = H_0 + \frac{H_t \exp\left(-\frac{H_t}{H_{00}}\right) - h \exp\left(-\frac{h}{H_{00}}\right)}{\exp\left(-\frac{H_t}{H_{00}}\right) - \exp\left(-\frac{h}{H_{00}}\right)} \quad (\text{B.6})$$

$$c_{f,1} = \frac{\exp\left(-\frac{h}{H_{00}}\right) - 1}{\exp\left(-\frac{H_t}{H_{00}}\right) - \exp\left(-\frac{h}{H_{00}}\right)} \left( \exp\left(-\frac{H_t}{H_e}\right) - \exp\left(-\frac{h}{H_e}\right) \right) \quad (\text{B.7})$$

$$c_{f,2} = \left( \exp\left(-\frac{h}{H_e}\right) - 1 \right) \quad (\text{B.8})$$

# Appendix C

## Analysis of variance (ANOVA)

### C.1 Notation

name	description
$SSB$	sum of squares: boundary effect
$SSS$	sum of squares: simulation effect
$SSS_{S_a}$	sum of squares: configuration effect
$SSS_{S_\gamma}$	sum of squares: initial condition
$TSS$	total sum of squares
$P_B$	proportion of total variance that results from the boundary forcing effect
$P_{S_a}$	proportion of total variance that results from the configuration
$P_{S_\gamma}$	proportion of total variance that results from the initial conditions

Table C.1: Notations for the analysis of variance on page 67f.

### C.2 Statistical tests

We will tie up to the introduction of the ANOVA given in section 4.2.1 and will exemplarily introduce the statistical test for the boundary effect here. We will keep close to the notation given in Zwiers (1996). The hypothesis to be tested is

$H_B$ : boundary forced effects are not present in the model ensemble

In terms of the model given in Eq. 4.2 this can be assigned as:

$$H_B : \beta_y = 0 \quad \text{for} \quad y = 1 \dots Y \quad (\text{C.1})$$

The test variable  $F_B$  with

$$F_B = \frac{SSB/(Y-1)}{SSI/((S-1)(Y-1))} \quad (\text{C.2})$$

is tested with critical values for the Fisher- $F$  distribution with  $(Y-1)$  and  $(S-1)(Y-1)$  degrees of freedom. The unbiased estimator of the proportion of the total variance that is

determined by the boundary forced effects is then given by

$$P_B = \left( SSB - \frac{SSI}{N-1} \right) / TSS. \quad (\text{C.3})$$

A similar test is applied for the hypothesis that the configuration effect is not significant and for the hypothesis that the initial conditions have no effect on the variance (cf. Appendix B in Zwiers (1996)).

# Bibliography

- Alley, R. B., J. Marotzke, W. D. Nordhaus, J. T. Overpeck, D. M. Peteet, R. A. Pielke Jr., R. T. Pierrehumbert, P. B. Rhines, T. F. Stocker, L. D. Talley, and J. M. Wallace (2003). Abrupt climate change. *Science* 299(5615), 2005 – 2010.
- AMIP II (2006). <http://www-pcmdi.llnl.gov/projects/amip/DIAGSUBS/diagsp.php>.
- Argyris, J. H., G. Faust, and M. Haase (1995). *Die Erforschung des Chaos*. Vieweg, Wiesbaden.
- Ashrit, R., K. Rupakumar, and K. K. Kumar (2001). ENSO-monsoon relationships in a greenhouse warming scenario. *Geophysical Research Letters* 28, 1727–1730.
- Bak, P. (1999). *How Nature Works, The Science of Self Organised Criticality*. Copernicus Books.
- Bamzai, A. S. and J. Shukla (1999). Relation between Eurasian snow cover, snow depth and the Indian summer monsoon: an observational study. *Journal of Climate* 12, 3117–3132.
- Barnett, T., L. Dümenil, U. Schlese, and E. Roeckner (1989). The effect of Eurasian snow cover on regional and global climate variations. *Journal of the Atmospheric Sciences* 46(5), 661–686.
- Barnola, J.-M., D. Raynaud, Y. Korotkevich, and C. Lorius. (1987). Vostok ice core provides 160,000-year record of atmospheric CO<sub>2</sub>. *Nature* 329, 408–414.
- Barsugli, J. J. and D. S. Battisti (1998). The basic effects of atmosphere-ocean thermal coupling on midlatitude variability. *Journal of Atmospheric Sciences* 55, 477–493.
- Behringer, D. W., M. Ji, and A. Leetmaa (1998). An improved coupled model for ENSO prediction and implications for ocean initialization. Part I: The ocean data assimilation system. *Monthly Weather Review* 126(4), 1013–1021.
- Bengtsson, L., K. Arpe, E. Roeckner, and U. Schulzweida (1996). Climate predictability experiments with a general circulation model. *Climate Dynamics* 12(4), 261–278.
- Berger, A. L. (1978). Long-term variations of daily insolation and quaternary climate changes. *Journal of Atmospheric Science* 35, 2362–2367.
- Blakely, J. N., D. Gauthier, G. Johnson, T. Carroll, and L. Pecora (2000). Experimental investigation of high-quality synchronization of coupled oscillators. *Chaos* 10(3), 738–744.
- Blandford, H. F. (1884). On the connection of the Himalaya snowfall with dry winds and seasons of drought in India. *Proc. Roy., Soc.* 37, 3–22.
- Bond, G., B. Kromer, J. Beer, R. Muscheler, M. N. Evans, W. Showers, S. Hoffmann, R. Lottibond, I. Hajdas, and G. Bonani (2001). Persistent solar influence on North Atlantic climate during the Holocene. *Science* 294(5549), 2130–2136.
- Boville, B. A. and P. R. Gent (1998). The NCAR climate system model, version one. *Journal of Climate* 11, 1115–1130.
- Brankovic, C. and T. Palmer (1997). Atmospheric seasonal predictability and estimates of ensemble size. *Monthly Weather Review* 125(5), 859–874.

- Bretherton, C. S. and D. S. Battisti (2000). An interpretation of the results from atmospheric general circulation models forced by the time history of the observed sea surface temperature distribution. *Geophysical Research Letters* 27(6), 767–770.
- Briggs, J. and F. D. Peat (1989). *The turbulent mirror: An illustrated guide to chaos theory and the science of wholeness*. New York: Harper & Row.
- Brovkin, V., M. Claussen, V. Petoukhov, and A. Ganopolski (1998). On the stability of the atmosphere-vegetation system in the Sahara/Sahel region. *J. Geophys. Res.* 103(D24), 31613–31624.
- Budyko, M. (1982). *The Earth's climate*, Volume 29 of *International Geophysics Series*. New York: Academic Press.
- Burns, S., D. Fleitmann, A. Matter, J. Kramers, and A. Al-Subbary (2003). Indian Ocean climate and an absolute chronology over Dansgaard/Oeschger events 9 to 13. *Science* 301, 1365–1367.
- Campolongo, F., J. Cariboni, A. Saltelli, and W. Schoutens (2005). Enhancing the Morris Method. In *Sensitivity Analysis of Model Output. Proceedings of the 4th International Conference on Sensitivity Analysis of Model Output (SAMO 2004)*, pp. 369–379. Los Alamos National Laboratory, Los Alamos.
- Cane, M. A., S. E. Zebiak, and S. C. Dolan (1986). Experimental forecasts of El Niño. *Nature* 321, 827–832.
- CERA (2006). <http://cera-www.dkrz.de>.
- Chang, C.-P., P. A. Harr, and J. Ju (2001). Possible roles of Atlantic circulations on the weakening Indian monsoon rainfall – ENSO relationship. *Journal of Climate* 14, 2376–2380.
- Chang, C.-P., Y. Zhang, and T. Li (2000). Interannual and interdecadal variations of the East Asian summer monsoon and Tropical Pacific SSTs. Part I: Roles of the subtropical ridge. *Journal of Climate* 13(24), 4310–4325.
- Clark, C. O., J. E. Cole, and P. J. Webster (2000). Indian Ocean SST and Indian summer rainfall: Predictive relationships and their decadal variability. *Journal of Climate* 13(14), 2503–2519.
- Claussen, M. (1997). Modeling bio-geophysical feedback in the African and Indian monsoon region. *Climate Dynamics* 13(4), 247 – 257.
- Collins, M. (2002). Climate predictability on interannual to decadal time scales: The initial value problem. *Climate Dynamics* 19(8), 671–692.
- Covey, C. K., K. M. AchutaRao, U. Cubasch, P. Jones, S. Lambert, M. Mann, T. Phillips, and K. Taylor (2003). An overview of results from the coupled model intercomparison project. *Global and Planetary Change* 37(1-2), 103–133.
- Covey, C. K., K. M. AchutaRao, P. Gleckler, T. Phillips, K. Taylor, and M. Wehner (2004). Coupled ocean-atmosphere climate simulations compared with simulations using prescribed sea surface temperature: Effect of a "perfect ocean". *Global and Planetary Change* 41(1), 1–14.
- CPDN (2006). <http://www.climateprediction.net>.
- Dash, S. K., G. P. Singh, M. S. Shekhar, and A. D. Vernekar (2005). Response of the Indian summer monsoon circulation and rainfall to seasonal snow depth anomaly over Eurasia. *Climate Dynamics* 24, 1–10.
- Dickinson, R. E., A. Henderson-Sellers, P. Kennedy, and M. Wilson (1986). Biosphere-atmosphere transfer scheme (BATS) for the NCAR community climate model. Technical report, NCAR/TN-275+STR, NCAR, Boulder, Colorado.



- Dijkstra, H. A. (2005). *Nonlinear Physical Oceanography: a dynamical systems approach to the large scale ocean circulation and El Niño* (2 ed.). Springer, Dordrecht, The Netherlands.
- Dijkstra, H. A. and W. Weijer (2003). Stability of the global ocean circulation: The connection of equilibria within a hierarchy of models. *Journal of Marine Research* 61, 725–743.
- Doedel, E. J. (1981). AUTO: A program for the automatic bifurcation analysis of autonomous systems. In *Proceedings of the 10th Manitoba Conference on Numerical Mathematics and Computing*, University of Manitoba, Winnipeg, Canada, pp. 265–284.
- Duane, G. (1997). Synchronized chaos in extended systems and meteorological teleconnections. *Physical Review E* 56(6), 6475–6493.
- Fasullo, J. and P. J. Webster (2002). Hydrologic signatures relating the Asian summer monsoon and ENSO. *Journal of Climate* 15(21), 3082–3095.
- Feudel, U. and W. Jansen (1992). CANDYS/QA - a software system for the qualitative analysis of nonlinear dynamical systems. *International Journal of Bifurcation and Chaos* 2, 773–794.
- Flechsig, M., U. Böhm, T. Nocke, and C. Rachimow (2005). Techniques for quality assurance of models in a multi-run simulation environment. In K. M. Hanson and F. M. Hemez (Eds.), *Sensitivity Analysis of Model Output. Proceedings of the 4th International Conference on Sensitivity Analysis of Model Output (SAMO 2004)*, Los Alamos National Laboratory, Los Alamos, USA, pp. 297–230.
- Forest, C., P. Stone, A. Sokolov, M. Allen, and M. Webster (2002). Quantifying uncertainties in climate system properties with the use of recent climate observations. *Science* 295(5552), 113–117.
- Friederichs, P. (2000). *Interannuelle und dekadische Variabilität der atmosphärischen Zirkulation in gekoppelten und SST-getriebenen GCM-Experimenten*. Ph. D. thesis, Bonner Meteorologische Abhandlungen, Bonn, Germany.
- Friederichs, P. and A. Hense (1999). Interannual to decadal variability of the atmospheric circulation in coupled and SST-forced GCM experiments. *Clivar Exchanges* 14.
- Fujisaka, H. and T. Yamada (1983). Stability theory of synchronized motion in coupled-oscillator systems. *Progress in Theoretical Physics* 69, 32–47.
- Gates, W. L., J. Boyle, C. Covey, C. Dease, C. Doutriaux, R. Drach, M. Fiorino, P. Gleckler, J. Hnilo, S. Marlais, T. Phillips, G. Potter, B. Santer, K. Sperber, K. Taylor, and D. Williams (1992). An overview of the results of the atmospheric model intercomparison project (AMIP I). *Bulletin of the American Meteorological Society* 73, 1962–1970.
- Gauthier, D. J. and J. C. Bienfang (1996). Intermittent loss of synchronization in coupled chaotic oscillators: toward a new criterion for high-quality synchronization. *Physical Review Letters* 77(9), 1751–1754.
- Gershunov, A., N. Schneider, and T. Barnett (2001). Low-frequency modulation of the ENSO-Indian monsoon rainfall relationship: Signal or noise? *Journal of Climate* 14(11), 2486–2492.
- Gnanadesikan, A. (1999). A simple predictive model for the structure of the oceanic pycnocline. *Science* 283(5410), 2077–2079.
- Gordon, C., C. Cooper, C. Senior, H. Banks, J. Gregory, T. Johns, J. Mitchell, and R. Wood (2000). The simulation of SST, sea ice extents and ocean heat transports in a version of the Hadley Centre coupled model without flux adjustments. *Climate Dynamics* 16, 147–168.
- Goswami, B. N. (1998). Physics of ENSO-Monsoon connection. *Indian Journal of Marine Science* 27, 82–89.

- Goswami, B. N., M. S. Madhusoodanan, C. P. Neema, and D. Sengupta (2006). A physical mechanism for North Atlantic SST influence on the Indian summer monsoon. *Geophysical Research Letters* 33(2), L02706.
- Griffies, S. M. and K. Bryan (1997). A predictability study of simulated North Atlantic multi-decadal variability. *Climate Dynamics* 13(7-8), 459–487.
- Gross, T. and U. Feudel (2006). Generalized models as a universal approach to the analysis of nonlinear dynamical systems. *Physical Review E* 73, 016205.
- Grötzner, A., M. Latif, A. Timmermann, and R. Voss (1999). Interannual to decadal predictability in a coupled ocean-atmosphere general circulation model. *Journal of Climate* 12, 2607–2624.
- Guckenheimer, J. and P. Holmes (1996). *Nonlinear Oscillations, Dynamical Systems, and Bifurcations of Vector Fields* (5 ed.). New York: Springer.
- Gupta, A., D. Anderson, and J. Overpeck (2003). Abrupt changes in the Asian southwest monsoon during the Holocene and their links to the North Atlantic Ocean. *Nature* 421, 354–357.
- Hahn, D. G. and J. Shukla (1976). An apparent relationship between Eurasian snow cover and Indian monsoon rainfall. *Journal of the Atmospheric Sciences* 33(12), 2461–2462.
- Haken, H. (1981). *Erfolgsgheimnisse der Natur. Synergetik – Die Lehre vom Zusammenwirken*. DVA.
- Hansen, J., G. Russell, D. Rind, P. Stone, A. Lacis, S. Lebedeff, R. Ruedy, and L. Travis (1986). Efficient three-dimensional global models for climate studies: Models I and II. *Monthly Weather Review* 11(4), 609–662.
- Heagy, J., N. Platt, and S. Hammel (1994). Characterization of on-off intermittency. *Physical Review E* 49, 1140–1150.
- Held, H. and T. Kleinen (2004). Detection of climate system bifurcations by degenerate fingerprinting. *Geophysical Research Letters* 31, L23207.
- Houghton, J., Y. Ding, D. Griggs, M. Noguer, P. van der Linden, X. Dai, K. Maskell, and C. Johnson (Eds.) (2001). *Climate Change 2001: The Scientific Basis. Contribution of Working Group I to the Third Assessment Report of the Intergovernmental Panel on Climate Change*. Cambridge University Press.
- Ji, M., D. W. Behringer, and A. Leetmaa (1998). An improved coupled model for ENSO prediction and implications for ocean initialization. Part II: The coupled model. *Monthly Weather Review* 126(4), 1022–1034.
- Jin, F.-F. (1997). An equatorial ocean recharge paradigm for ENSO. Part I: Conceptual model. *Journal of Atmospheric Science* 54, 811–829.
- John, T., U. Behn, and R. Stannarius (2002). Fundamental scaling laws of on-off intermittency in a stochastically driven dissipative pattern-forming system. *Physical Review E* 65, 046229.
- Ju, J. and J. M. Slingo (1995). The Asian summer monsoon and ENSO. *Quarterly Journal of the Royal Meteorological Society* 121, 1133–1168.
- Jungclauss, J. H., M. Botzet, H. Haak, N. Keenlyside, J.-J. Luo, M. Latif, J. Marotzke, U. Mikolajewicz, and E. Roeckner (2006). Ocean circulation and tropical variability in the coupled model ECHAM5/MPI-OM. *Journal of Climate*. submitted.
- Kalnay, E., M. Kanamitsu, R. Kistler, W. Collins, D. Deaven, L. Gandin, M. Iredell, S. Saha, G. White, J. Woollen, Y. Zhu, M. Chelliah, W. Ebisuzaki, W. Higgins, J. Janowiak, K. C. Mo, C. Ropelewski, J. Wang, A. Leetmaa, R. Reynolds, R. Jenne, and D. Joseph (1996). The NMC/NCAR 40-year reanalysis project. *Bull. Amer. Meteor. Soc.* 77, 437–471. Data available at <http://www.cdc.noaa.gov/>.

- Kaneko, K. (1992). Overview of coupled map lattices. *Chaos* 3(2), 279–282.
- Kaplan, A., M. Cane, Y. Kushnir, A. C. Clement, M. B. Blumenthal, and B. Rajagopalan (1998). Analyses of global sea surface temperature 1856-1991. *Journal of Geophysical Research* 103, 18567–18589.
- Kirtman, B. and J. Shukla (2000). Influence of the Indian summer monsoon on ENSO. *Quarterly Journal of the Royal Meteorological Society* 126, 213–239.
- Kitoh, A., S. Yukimoto, and A. Noda (1999). ENSO-monsoon relationship in the MRI coupled GCM. *Journal of the Meteorologic Society of Japan* 77, 1221–1245.
- Klein, S. A. and D. L. Hartmann (1993). The seasonal cycle of low stratiform clouds. *Journal of Climate* 6, 1587–1606.
- Knopf, B., H. Held, and H. J. Schellnhuber (2005). Forced versus coupled dynamics in Earth System modelling and prediction. *Nonlinear Processes in Geophysics* 12, 311–320.
- Knutti, R., T. F. Stocker, F. Joos, and G.-K. Plattner (2002). Constraints on radiative forcing and future climate change from observations and climate model ensembles. *Nature* 416, 719–723.
- Kripalani, R. H. and A. Kulkarni (1997). Climatic impact of El Niño on the Indian monsoon: A new perspective. *Weather* 52, 39–46.
- Kripalani, R. H., A. Kulkarni, S. S. Sabade, and M. L. Khandekar (2003). Indian monsoon variability in a global warming scenario. *Natural Hazards*.
- Kripalani, R. H., A. Kulkarni, and S. V. Singh (1997). Association of the Indian summer monsoon with the Northern Hemisphere mid-latitude circulation. *International Journal of Climatology* 17(10), 1055 – 1067.
- Krishnamurthy, V. and B. N. Goswami (2000). Indian Monsoon-ENSO relationship on interdecadal timescale. *Journal of Climate* 13, 579–595.
- Kucharski, F., F. Molteni, and J. H. Yoo (2006). SST forcing of decadal Indian Monsoon rainfall variability. *Geophysical Research Letters* 33(3), L03709.
- Kumar, A., M. Hoerling, M. Ji, A. Leetmaa, and P. Sardeshmukh (1996). Assessing a GCM's suitability for making seasonal predictions. *Journal of Climate* 9(1), 115–129.
- Kumar, A., Q. Zhang, P. Peng, and B. Jha (2005). SST-forced atmospheric variability in an atmospheric general circulation model. *Journal of Climate* 18(19), 3953–3967.
- Kumar, K. K., B. Rajagopalan, and M. A. Cane (1999). On the weakening relationship between the Indian monsoon and ENSO. *Science* 284, 2156–2159.
- Kumar Mittal, A., S. Dwivedi, and A. Chandra Pandey (2005). Bifurcation analysis of a paradigmatic model of monsoon prediction. *Nonlinear Processes in Geophysics* 12, 707–715.
- Kurths, J., S. Boccaletti, C. Grebogi, and Y. Lai (2003). Introduction: Control and synchronization in chaotic dynamical systems. *Chaos* 13(1), 126–127.
- Kuznetsov, Y. A., V. V. Levitin, and A. Skovoroda (1997). Continuation of stationary solutions to evolution problems in CONTENT. Technical Report AM-R9611, Centrum voor Wiskunde en Informatica, Amsterdam, The Netherlands.
- Lai, Y.-C. (1996). Distinct small-distance scaling behavior of on-off intermittency in chaotic dynamical systems. *Physical Review E* 54(1), 321–327.
- Lal, M., U. Cubasch, R. Voss, and J. Waszkewitz (1995). Effect of transient increase in greenhouse gases and sulphate aerosols on monsoon climate. *Current Science* 69(9), 752–763.

- Latif, M., E. Roeckner, U. Mikolajewicz, and R. Voss (2000). Tropical stabilization of the thermohaline circulation in a greenhouse warming simulation. *Journal of Climate* 13(11), 1809–1813.
- Latif, M., K. Sperber, J. Arblaster, P. Braconnot, D. Chen, A. Colman, U. Cubasch, M. Davey, P. Delecluse, D. DeWitt, L. Fairhead, G. Flato, T. Hogan, M. Ji, M. Kimoto, A. Kitoh, T. Knutson, H. L. Treut, T. Li1, S. Manabe, O. Marti, C. Mechoso, G. Meehl, S. Power, E. Roeckner, J. Sirven, L. Terray, A. Vintzileos, R. Voss, B. Wang, W. Washington, I. Yoshikawa, J. Yu, and S. Zebiak (2001). ENSIP: The El Niño simulation intercomparison project. *Climate Dynamics* 18, 255–276.
- Lau, K. M. and S. Yang (1996). The Asian monsoon and predictability of the tropical ocean-atmosphere system. *Quarterly Journal of the Royal Meteorological Society* 122(532), 945–957.
- Levermann, A. and A. Griesel (2004). Solution of a model for the oceanic pycnocline depth: Scaling of overturning strength and meridional pressure difference. *Geophysical Research Letters* 31, L17302.
- Li, T., Y. Zhang, C.-P. Chang, and B. Wang (2001). On the relationship between Indian ocean sea surface temperature and Asian summer monsoon. *Geophysical Research Letters* 28(14), 2843–7.
- Liu, X. and Z. Yin (2002). Sensitivity of East Asian monsoon climate to the uplift of the Tibetan Plateau. *Palaeogeography, Palaeoclimatology, Palaeoecology* 183, 223–245.
- Longworth, H., J. Marotzke, and T. F. Stocker (2005). Ocean gyres and abrupt change in the thermohaline circulation: A conceptual analysis. *Journal of Climate* 18, 2403–2416.
- Lorenz, E. N. (1963). Deterministic nonperiodic flow. *Journal of the Atmospheric Sciences* 20(2), 130–141.
- Lorenz, E. N. (1984). Irregularity: A fundamental property of the atmosphere. *Tellus* 36A, 98–110.
- Lorenz, E. N. (1993). *The essence of chaos*. University of Washington Press.
- Maier-Reimer, E., U. Mikolajewicz, and K. Hasselmann (1993). Mean circulation of the Hamburg LSG OGCM and its sensitivity to the thermohaline surface forcing. *Journal of Physical Oceanography* 23, 731–757.
- May, W. (2002). Simulated changes of the Indian summer monsoon under enhanced greenhouse gas conditions in a global time-slice experiment. *Geophysical Research Letters* 29(7), 1118–1121.
- McKay, M. D., R. Beckman, and W. J. Conover (1979). A comparison of three methods of selecting values of input variables in the analysis of output from a computer code. *Technometrics* 21, 239–245.
- Meehl, G., G. Boer, C. Covey, M. Latif, and R. Stouffer (2000). The coupled model intercomparison project (CMIP). *Bulletin of the American Meteorological Society* 81, 313–318.
- Meehl, G. A. (1994). Coupled land-ocean-atmosphere processes and South Asian monsoon variability. *Science* 266, 263–267.
- Meehl, G. A. (1997). The south Asian monsoon and the tropospheric biennial oscillation. *Journal of Climate* 10, 1921–1943.
- Meehl, G. A. and J. M. Arblaster (1998). The Asian-Australian Monsoon and El Niño-Southern Oscillation in the NCAR climate system model. *Journal of Climate* 11, 1356–1385.
- Meehl, G. A. and J. M. Arblaster (2003). Mechanisms for projected future changes in south Asian monsoon precipitation. *Climate Dynamics* 21(7-8), 659–675.

- Meehl, G. A. and W. M. Washington (1993). South Asian monsoon variability in a model with doubled atmospheric carbon dioxide concentration. *Science* 260, 1101–1104.
- Mehta, V. M., M. J. Suarez, J. V. Manganello, and T. L. Delworth (2000). Oceanic influence on the North Atlantic Oscillation and associated Northern Hemisphere climate variations. *Geophysical Research Letters* 27(1), 121–124.
- MODIS (2006). <http://modis-atmos.gsfc.nasa.gov/ALBEDO/index.html>.
- Morgan, M. G. and M. Henrion (1990). *Uncertainty: A Guide to Dealing with Uncertainty in Quantitative Risk and Policy Analysis*. Cambridge University Press.
- Morris, M. D. (1991). Factorial sampling plans for preliminary computational experiments. *Technometrics* 33(2), 161–174.
- Nakićenović, N., J. Alcamo, G. Davis, B. de Vries, J. Fenhann, S. Gaffin, K. Gregory, A. Grübler, T. Y. Jung, T. Kram, E. L. L. Rovere, L. Michaelis, S. Mori, T. Morita, W. Pepper, H. Pitcher, L. Price, K. Riahi, A. Roehrl, H.-H. Rogner, A. Sankovski, M. Schlesinger, P. Shukla, S. Smith, R. Swart, S. van Rooijen, N. Victor, and Z. Dadi (2000). *IPCC Special Report on Emissions Scenarios*. Cambridge University Press.
- Nordhaus, W. D. (1994). *Managing the Global Commons. The Economics of Climate Change*. MIT Press, Cambridge.
- Ott, E. and J. Sommerer (1994). Blowout bifurcations: the occurrence of riddled basins and on-off intermittency. *Physical Letters A* 188, 39–47.
- Palmer, T. N. (1993). Extended-range atmospheric prediction and the Lorenz model. *Bulletin of the American Meteorological Society* 74(1), 49–65.
- Parthasarathy, B., A. A. Munot, and D. R. Kothawale (1995). All India monthly and seasonal rainfall series: 1871–1993. *Theoretical and Applied Climatology* 49, 217–224.
- Parthasarathy, B., K. Rupa Kumar, and A. Munot (1992). Forecast of rainy season foodgrain production based on monsoon rainfall. *Indian Journal of Agricultural Sciences* 62, 1–8.
- Paté-Cornell, M. E. (1996). Uncertainties in risk analysis: Six levels of treatment. *Reliability Engineering & System Safety* 54, 95–111.
- Patra, P. K., S. K. Behera, J. R. Herman, S. Maksyutov, H. Akimoto, and T. Yamagata (2005). The indian summer monsoon rainfall: interplay of coupled dynamics, radiation and cloud microphysics. *Atmospheric Chemistry and Physics* 5, 2181–2188.
- Pazó, D., M. A. Zaks, and J. Kurths (2003). Role of unstable periodic orbits in phase and lag synchronization between coupled chaotic oscillators. *Chaos* 13(1), 309–318.
- Pecora, L. M. and T. L. Carroll (1990). Synchronization in chaotic systems. *Physical Review Letters* 64, 821–824.
- Pecora, L. M., T. L. Carroll, G. A. Johnson, D. Mar, and J. F. Heagy (1997). Fundamentals of synchronization in chaotic systems, concepts, and applications. *Chaos* 7(4), 520–543.
- Peixoto, J. P. and A. H. Oort (1992). *Physics of Climate*. Springer Verlag New York.
- Petit, J. R., J. Jouzel, D. Raynaud, N. Barkov, J. M. Barnola, I. Basile, M. Bender, J. Chappellaz, J. Davis, G. Delaygue, M. Delmotte, V. Kotlyakov, M. Legrand, V. Lipenkov, C. Lorius, L. Pépin, C. Ritz, E. Saltzman, and M. Stievenard (1999). Climate and atmospheric history of the past 420,000 years from the Vostok ice core, Antarctica. *Nature* 399, 429–436.
- Petoukhov, V., M. Claussen, A. Berger, M. Crucifix, M. Eby, A. V. Eliseev, T. Fichet, A. Ganopolski, H. Goosse, I. Kamenkovich, I. I. Mokhov, M. Montoya, L. A. Mysak, A. Sokolov, P. Stone, Z. Wang, and A. J. Weaver (2005). EMIC intercomparison project (EMIP-CO<sub>2</sub>): comparative analysis of EMIC simulations of climate, and of equilibrium and transient responses to atmospheric CO<sub>2</sub> doubling. *Climate Dynamics* 25(4), 363–385.

- Petoukhov, V., A. Ganopolski, V. Brovkin, M. Claussen, A. Eliseev, C. Kubatzki, and S. Rahmstorf (2000). CLIMBER-2: a climate system model of intermediate complexity. Part I: model description and performance for present climate. *Climate Dynamics* 16, 1–17.
- Petoukhov, V., A. Ganopolski, and M. Claussen (2003). POTSDAM - a set of atmosphere statistical-dynamical models: theoretical background. Technical Report 81, Potsdam Institute for Climate Impact Research, Potsdam. [http://www.pik-potsdam.de/publications/pik\\_reports](http://www.pik-potsdam.de/publications/pik_reports).
- Pierce, D., T. Barnett., N. Schneider, R. Saravanan, D. Dommenges, and M. Latif (2001). The role of ocean dynamics in producing decadal climate variability in the North Pacific. *Climate Dynamics* 18(1-2), 51–70.
- Pikovsky, A. and P. Grassberger (1991). Symmetry breaking bifurcation for coupled chaotic attractors. *Journal of Physics A* 24, 4587–4597.
- Pikovsky, A., M. Rosenblum, and J. Kurths (2001). *Synchronization: A universal concept in nonlinear sciences*. Cambridge University Press.
- Pikovsky, A. and V. G. Shekhov (1991). Universal behaviour of two coupled circle maps. *Journal of Physics A* 24, 183–190.
- Pikovsky, A., M. Zaks, M. Rosenblum, G. Osipov, and J. Kurths (1997). Phase synchronization of chaotic oscillations in terms of periodic orbits. *Chaos* 7(4), 680–687.
- Plambeck, E. L., C. Hope, and J. Anderson (1997). The Page95 model: Integrating the science and economics of global warming. *Energy Economics* 19, 77–101.
- Platt, N., E. A. Spiegel, and C. Tresser (1993). On-off intermittency: A mechanism for bursting. *Physical Review Letters* 70(3), 279–282.
- Pohlmann, H., M. Botzelt, M. Latif, A. Roesch, M. Wild, and P. Tschuck (2004). Estimating the decadal predictability of a coupled AOGCM. *Journal of Climate* 17, 4463–4472.
- Prabhu, C., R. Shankar, K. Anupama, M. Taieb, R. Bonnefille, L. Vidal, and S. Prasad (2004). A 200-ka pollen and oxygen isotopic record from two sediment cores from the eastern Arabian Sea. *Palaeogeography, Palaeoclimatology, Palaeoecology* 214, 309–321.
- Prantl, L. (1942). *Führer durch die Strömungslehre*. Vieweg u. Sohn, Braunschweig.
- Quan, X., P. J. Webster, A. M. Moore, and H. R. Chang (2004). Seasonality in SST-forced atmospheric short-term climate predictability. *Journal of Climate* 17(16), 3090–3108.
- Rahmstorf, S. (1996). On the freshwater forcing and transport of the Atlantic thermohaline circulation. *Climate Dynamics* 12, 799–811.
- Rahmstorf, S., M. Crucifix, A. Ganopolski, H. Goosse, I. V. Kamenkovich, R. Knutti, G. Lohmann, R. Marsh, L. A. Mysak, Z. Wang, , and A. J. Weaver (2005). Thermohaline circulation hysteresis: a model intercomparison. *Geophysical Research Letters* 32, L23605.
- Rial, J. A., R. A. Pielke, M. Beniston, M. Claussen, J. Canadell, P. Cox, H. Held, N. de Noblet-Ducoudré, R. Prinn, J. F. Reynolds, and J. D. Salas (2004). Nonlinearities, feedbacks and critical thresholds within the Earth's climate system. *Climate Dynamics* 65(1-2), 11–38.
- Robock, A., M. Mu, K. Vinnikov, and D. Robinson (2003). Land surface conditions over Eurasia and Indian summer monsoon rainfall. *Journal of Geophysical Research (Atmospheres)* 108(D4), 4131.
- Rodwell, M. J., D. P. Rowell, and C. K. Folland (1999). Oceanic forcing of the wintertime North Atlantic Oscillation and European climate. *Nature* 398, 320–323.
- Roebber, P. (1995). Climate variability in a low-order coupled atmosphere-ocean model. *Tellus* 47A, 473–494.

- Roeckner, E., G. Baeuml, L. Bonaventura, R. Brokopf, M. Esch, M. Giorgetta, S. Hagemann, I. Kirchner, L. Kornblueh, E. Manzini, A. Rhodin, U. Schlese, U. Schulzweida, and A. Tompkins (2003). The atmospheric general circulation model ECHAM5: Part I: Model description. MPI Report 349, Max-Planck-Institut für Meteorologie, Hamburg, Germany.
- Roeckner, E., K. Arpe, L. Bengtsson, S. Brinkop, L. Dümenil, M. Esch, E. Kirk, F. Lunkeit, M. Ponater, B. Rockel, R. Sausen, U. Schlese, S. Schubert, and M. Windelband (1992). Simulation of the present-day climate with the ECHAM model: Impact of model physics and resolution. MPI Report 93, Max-Planck-Institut für Meteorologie, Hamburg, Germany.
- Roeckner, E., K. Arpe, L. Bengtsson, M. Christoph, M. Claussen, L. Dümenil, M. Esch, M. Giorgetta, U. Schlese, and U. Schulzweida (1996). The atmospheric general circulation model ECHAM-4: Model description and simulation of present-day climate. MPI Report 218, Max-Planck-Institut für Meteorologie, Hamburg, Germany.
- Rotmans, J. and H. Dowlatabadi (1998). Integrated assessment modelling. In S. Rayner and E. Malone (Eds.), *Human Choice and Climate Change*, Volume 3, pp. 291–378. Battelle Press, Columbus, OH, USA.
- Rotmans, J. and M. B. A. van Asselt (2001). Uncertainty in integrated assessment modelling: A labyrinthic path. *Integrated Assessment* 2(2), 43–55.
- Rowell, D. P. (1998). Assessing potential seasonal predictability with an ensemble of multidecadal GCM simulations. *Journal of Climate* 11(2), 109–120.
- Rowell, D. P., C. K. Folland, K. Maskell, and M. N. Ward (1995). Variability of summer rainfall over tropical North Africa (1906-92): Observations and modelling. *Quarterly Journal of the Royal Meteorological Society* 121, 669–704.
- Sachs, L. (1992). *Angewandte Statistik*. Springer Verlag.
- Saltelli, A., S. Tarantola, F. Campolongo, and M. Ratto (2004). *Sensitivity Analysis in Practice. A Guide to Assessing Scientific Models*. John Wiley & Sons.
- Sarkar, S., R. P. Singh, and M. Kafatos (2004). Further evidences for the weakening relationship of Indian rainfall and ENSO over India. *Geophysical Research Letters* 31(13), L13209.
- Sarnthein, M., J. Kennett, J. Allen, J. Beer, P. Grootes, C. Laj, J. McManus, R. Ramesh, and SCOR-IMAGES W.G. 117 (2002). Decadal-to-millennial-scale climate variability – chronology and mechanisms: Summary and recommendations. *Quaternary Science Reviews* 21, 1121–1128.
- Schellnhuber, H. J. and V. Wenzel (Eds.) (1998). *Earth System Analysis: Integrating Science for Sustainability*. Springer, Heidelberg.
- Schellnhuber, H. J. and G. Yohe (1997). Comprehending the economic and social dimensions of climate change by Integrated Assessment. In *Proceedings of the Conference on the World Climate Research Programme: Achievements, Benefits and Challenges*, Geneva, WMO, 179.
- Schlosser, C. and B. P. Kirtman (2005). Predictable skill and its association to sea-surface temperature variations in an ensemble climate simulation. *Journal of Geophysical Research* D19, D19107. doi:10.1029/2005JD005835.
- Schneider von Deimling, T., H. Held, A. Ganopolski, and S. Rahmstorf (2006). Climate sensitivity estimated from ensemble simulations of glacial climate. *Climate Dynamics* 27. accepted.
- Shaman, J. and E. Tziperman (2005). The effect of ENSO on Tibetan Plateau snow depth: a stationary wave teleconnection mechanism and implications for the South Asian monsoons. *Journal of Climate* 18, 2067–2079.
- Shilnikov, A., G. Nicolis, and C. Nicolis (1995). Bifurcation and predictability analysis of a low-order atmospheric circulation model. *Bifurcations & Chaos* 5(6), 1701–1711.

- Shukla, J. and D. A. Paolino (1983). The Southern Oscillation and long range forecasting of the summer monsoon over India. *Monthly Weather Review* 111, 1830–1837.
- SimEnv (2006). <http://www.pik-potsdam.de/software/simenv>.
- Smith, L. A., C. Ziehmann, and K. Fraedrich (1999). Uncertainty dynamics and predictability in chaotic systems. *Quarterly Journal of the Royal Meteorological Society* 155(560), 2855–2886.
- Stainforth, D. A., T. Aina, C. Christensen, M. Collins, N. Faull, D. J. Frame, J. A. Kettleborough, S. Knight, A. Martin, J. M. Murphy, C. Piani, D. Sexton, L. A. Smith, R. A. Spicer, A. J. Thorpe, and M. R. Allen (2005). Uncertainty in predictions of the climate response to rising levels of greenhouse gases. *Nature* 433, 403–406.
- Stommel, H. (1961). Thermohaline convection with two stable regimes of flow. *Tellus* 13, 224–241.
- Stott, P., S. Tett, G. Jones, M. Allen, J. Mitchell, and G. Jenkins (2000). External control of twentieth century temperature variations by natural and anthropogenic forcings. *Science* 15, 2133–2137.
- Terray, P. (1995). Space-time structure of monsoon interannual variability. *Journal of Climate* 8, 2595–2619.
- Timmermann, A., S.-I. An, U. Krebs, and H. Goosse (2005). ENSO suppression due to weakening of the North Atlantic thermohaline circulation. *Journal of Climate* 18, 3122–3139.
- Titz, S., T. Kuhlbrodt, S. Rahmstorf, and U. Feudel (2002). On freshwater-dependent bifurcations in box models of the interhemispheric thermohaline circulation. *Tellus A* 54(1), 89–98.
- Tol, R. S. J. (1999). Safe policies in an uncertain climate: an application of FUND. *Global Environmental Change* 9, 221–232.
- Torrence, C. and P. J. Webster (1999). Interdecadal changes in the ENSO-monsoon system. *Journal of Climate* 12, 2679–2690.
- Tóth, F. L., T. Bruckner, H.-M. Füßel, M. Leimbach, and G. Petschel-Held (2003). Integrated assessment of long-term climate policies: Part 2 – model results and uncertainty analysis. *Climatic Change* 56(1-2), 57–72.
- Tziperman, E., M. A. Cane, S. Zebiak, Y. Xue, and B. Blumenthal (1998). Locking of El Niño’s peak time to the end of the calendar year in the delayed oscillator picture of ENSO. *Journal of Climate* 11, 2191–2199.
- Tziperman, E. and H. Gildor (2003). On the mid-Pleistocene transition to 100-kyr glacial cycles and the asymmetry between glaciation and deglaciation times. *Paleoceanography* 18(1), 1–1.
- van Veen, L., T. Opsteegh, and F. Verhulst (2001). Active and passive ocean regimes in a low-order climate model. *Tellus* 53A, 616–628.
- Visser, H., R. Folkert, J. Hoekstra, and J. de Wolff (2000). Identifying key sources of uncertainty in climate change projections. *Climatic Change* 45(3-4), 421–457.
- von Storch, H. and F. W. Zwiers (1999). *Statistical Analysis in Climate Research*. Cambridge University Press.
- Waldrop, M. M. (1992). *Complexity, the emerging science at the edge of chaos*. Touchstone, New York.
- Walker, G. T. (1923). Correlation in seasonal variation of weather. VIII: A preliminary study of world weather. *Memoirs, India Meteorological Department* 24, 75–131.
- Wang, B. and Z. Fang (1996). Chaotic oscillation of tropical climate: A dynamic system theory for ENSO. *Journal of the Atmospheric Sciences* 53, 2786–2802.



- Wang, P., S. Clemens, L. Beaufort, P. Braconnot, G. Ganssen, Z. Jian, P. Kershaw, and M. Sarnthein (2005). Evolution and variability of the Asian monsoon system: state of the art and outstanding issues. *Quaternary Science Reviews* 24, 595–629.
- Washington, W. M., J. W. Weatherly, G. A. Meehl, A. J. S. Jr., T. W. Bettge, A. P. Craig, W. G. S. Jr., J. Arblaster, V. B. Wayland, R. James, and Y. Zhang (2000). Parallel climate model (PCM) control and transient simulations. *2000* 16(10-11), 755–774.
- Webster, P. J., V. O. Magaña, T. N. Palmer, J. Shukla, R. A. Tomas, M. Yanai, and T. Yasunari (1998). Monsoons: Processes, predictability, and the prospects for prediction. *Journal of Geophysical Research* 103, 14,451–14,510.
- Webster, P. J. and T. N. Palmer (1997). The past and future of El Niño. *Nature* 390, 562–564.
- Webster, P. J. and S. Yang (1992). Monsoon and ENSO: Selectively interactive systems. *Quarterly Journal of the Royal Meteorological Society* 118, 877–926.
- Wei, M. (2005). A coupled model study on the intensification of the Asian summer monsoon in IPCC SRES scenarios. *Advances in Atmospheric Sciences* 22(6), 798–806.
- Williams, K. D., C. A. Senior, and J. F. B. Mitchell (2001). Transient climate change in the Hadley Centre models: The role of physical processes. *Journal of Climate* 14, 2659–2674.
- Wittenberg, A. T. and J. L. Anderson (1998). Dynamical implications of prescribing part of a coupled system: Results from a low order model. *Nonlinear Processes in Geophysics* 5, 167–179.
- Wu, G. and Y. Zhang (1998). Tibetan Plateau forcing and the timing of the monsoon onset over South Asia and the South China Sea. *Monthly Weather Review* 126(4), 913–927.
- Wu, R. and B. P. Kirtman (2003). On the impacts of the Indian summer monsoon on ENSO in a coupled GCM. *Quarterly Journal of the Royal Meteorological Society* 129(595), 3439–3468.
- Wu, R. and B. P. Kirtman (2004). Impacts of the Indian Ocean on the Indian summer monsoon-ENSO relationship. *Journal of Climate* 17(15), 3037–3054.
- Yanai, M., C. Li, and Z. Song (1992). Seasonal heating of the Tibetan Plateau and its effects on the evolution of the Asian summer monsoon. *Journal of the Meteorological Society of Japan* 70, 319–351.
- Ye, D.-Z. and G.-X. Wu (1998). The role of the heat source of the Tibetan Plateau in the general circulation. *Meteorology and Atmospheric Physics* 67(1-4), 181 – 198.
- Yuan, D., H. Cheng, R. L. Edwards, C. A. Dykoski, M. J. Kelly, M. Zhang, J. Qing, Y. Lin, Y. Wang, J. Wu, J. A. Dorale, Z. An, and Y. Cai (2004). Timing, duration, and transitions of the last interglacial Asian Monsoon. *Science* 304(5670), 575–578.
- Zheng, Z., G. Hu, and B. Hu (1998). Phase slips and phase synchronization of coupled oscillators. *Physical Review Letters* 81(24), 5318–5321.
- Zickfeld, K. (2004). *Modelling large-scale singular climate events for Integrated Assessment*. Ph. D. thesis, Universität Potsdam, Germany. <http://deposit.ddb.de/cgi-bin/dokserv?idn=971983453>.
- Zickfeld, K., B. Knopf, V. Petoukhov, and H.-J. Schellnhuber (2005). Is the Indian summer monsoon stable against global change? *Geophysical Research Letters* 32, L15707. doi:10.1029/2005GL022771.
- Zwiers, F. W. (1987). A potential predictability study conducted with an atmospheric general circulation model. *Monthly Weather Review* 115, 2957–2974.
- Zwiers, F. W. (1996). Interannual variability and predictability in an ensemble of AMIP climate simulations conducted with the CCC GCM2. *Climate Dynamics* 12, 825–847.

- Zwiers, F. W. and V. V. Kharin (1998). Changes in the extremes of the climate simulated by CCC GCM2 under CO<sub>2</sub> doubling. *Journal of Climate* 11(9), 2200–2222.

# Danksagung

An dieser Stelle möchte ich allen danken, die direkt und indirekt am Gelingen dieser Arbeit ihren Anteil hatten:

- Hans-Joachim Schellnhuber möchte ich dafür danken, dass er es mir ermöglicht hat, am PIK meine Dissertation zu schreiben. Seine Anregungen waren immer sehr hilfreich.
- Mein ganz großer Dank geht an Hermann Held, der mir oft mit Diskussionen den richtigen Anstoß gegeben hat. Von ihm habe ich viele wertvolle Anregungen und Ideen erhalten. Darüber hinaus möchte ich ihm ganz herzlich danken, dass er mir durch sein Verständnis ermöglicht hat, Familie und Beruf in Einklang zu bringen.
- Kirsten Zickfeld danke ich ganz herzlich für die nette Zimmernachbarschaft und ihre andauernde Bereitschaft, sich mit mir über das Monsun-Modell auszutauschen. Ihre Anregungen und Ideen haben mich entscheidend weiter gebracht.
- Vladimir Petoukhov danke ich für die Beantwortung von vielen, vielen Fragen im Zusammenhang mit dem Monsun Modell.
- Michael Flechsig danke ich für die unkomplizierte und nette Zusammenarbeit bei der Durchführung der Multi-Run Analyse.
- Klaus Eisenack, Malaak Kallache, Henning Rust, Elmar Kriegler, Thomas Schneider, Till Kuhlbrodt, Matthias Lüdeke, Jürgen Kropp und den vielen anderen ungenannten KollegInnen möchte ich ganz herzlich für die überaus freundliche, kollegiale und inspirierende Arbeitatmosphäre am PIK danken.
- Anders Levermann, Jürgen Scheffran, Manfred Stock und vor allem Thomas Kleinen danke ich für die vielen hilfreichen Anmerkungen zu Entwürfen meiner Arbeit.
- Petra Friederichs, Michael Botzet und Adam Phillips danke ich für die Bereitstellung von Daten der GCM Ensemble Simulationen.
- Der Rosa Luxemburg Stiftung danke ganz herzlich für ihr Stipendium, das es mir ermöglichte, für zwei Jahre meiner Arbeit an der Dissertation unabhängig nachzugehen.
- Meinen Kindern Julian und Benjamin danke ich ganz herzlich dafür, dass sie *kein* Verständnis für meine Arbeit hatten und mich immer wieder auf den Spielplatz gezerrt haben. Sie haben mir so gezeigt, dass es auch noch andere wichtige Dinge im Leben gibt.
- Meiner ganzen Familie, Schwiegerfamilie und Freunden danke ich für ihr Interesse an meiner Arbeit, ihre Unterstützung bei der Kinderbetreuung und ihr Verständnis für meine manchmal knappe Zeit.
- Mein ganz besonderer Dank geht an meinen Lebensgefährten Thomas Fiedler, der mir zu jeder Zeit eine ganz große Stütze und ein unverzichtbarer Ratgeber war. Vielen Dank!